PZT Thin-Film Micro Probe Device with Dual Top Electrodes

Chuan Luo

A dissertation
submitted in partial fulfillment of the
requirements for the degree of

Doctor of Philosophy

University of Washington
2013

Reading Committee:
I.Y. Shen
Guozhong Cao
Jiangyu Li

Program Authorized to Offer Degree:
Mechanical Engineering

University of Washington

Abstract

PZT Thin Film Micro Probe Device with Dual Top Electrodes

Chuan Luo

Co-Chairs of the Supervisory Committee:

Professor I.Y. Shen

Department of Mechanical Engineering

Professor Guozhong Cao

Department of Material Science and Engineering

Lead zirconate titanate (PZT) thin-film actuators have been studied intensively for years because of their potential applications in many fields. In this dissertation, a PZT thin-film micro probe device is designed, fabricated, studied, and proven to be acceptable as an intracochlear acoustic actuator. The micro probe device takes the form of a cantilever with a PZT thin-film diaphragm at the tip of the probe. The tip portion of the probe will be implanted in cochlea later in animal tests to prove its feasibility in hearing rehabilitation. The contribution of the dissertation is three-fold.

First, a dual top electrodes design, consisting of a center electrode and an outer electrode, is developed to improve actuation displacement of the PZT thin-film diaphragm. The improvement by the dual top electrodes design is studied via a finite element model. When the dimensions of the dual electrodes are optimized, the displacement of the PZT thin-film diaphragm increases about 30%. A PZT thin-film diaphragm with dual top electrodes is fabricated to prove the concept, and experimental results confirm the predictions from the finite element analyses. Moreover, the dual electrode design can accommodate presence of significant residual stresses in the PZT thin-film diaphragm by changing the phase difference between the two electrodes.

Second, a PZT thin-film micro probe device is fabricated and tested. The fabrication process consists of PZT thin-film deposition and deep reactive ion etching (DRIE). The uniqueness of the fabrication process is an automatic dicing mechanism that allows a large number of probes to be released easily from the wafer. Moreover, the fabrication is very efficient, because the DRIE process will form the PZT thin-film diaphragm and the special dicing mechanism simultaneously. After the probes are fabricated, they are tested with various possible implantation depths (i.e., boundary conditions). Experimental results show that future implantation depths should be less than 3 mm in order to guarantee the first resonant frequency above 60 kHz.

Finally, a package for the PZT thin-film micro probe device is developed to ensure its proper function in an aqueous environment, such as inside of cochlea. The package is an insulation layer of parylene coating on the probe. A finite element analysis indicates that a coating thickness of less than 1 μm will reduce the PZT diaphragm displacement by less than 10%. A special fixture is designed to hold a large number of probes for parylene deposition of a thickness of 250 nm. A packaged probe is then submerged in deionized water and functions properly for at least 54 hours. Displacement and impedance of the probe are measured via a laser Doppler vibrometer and an impedance analyzer, respectively. Experimental results show that displacement of the PZT diaphragm increases about 30% in two hours, after the probe is submerged in the deionized water. The impedance measurement shows consistent trends. A hypothesis to explain this unusual phenomenon is diffusion of water molecules into the PZT thin film. High-resolution SEM images of the probe indicate presence of numerous nano-pores in the surface of the PZT thin film, indirectly confirming the hypothesis.

Keywords: PZT, Thin-Film, Dual Electrodes, Parylene Coating, Aqueous Environment, Cochlear Implant

Table of Contents

Chapter 1 Introduction 1

1.1 Sensori-neural hearing loss and rehabilitation 2

1.2 Proposed application of hybrid cochlea implant hearing aid 7

1.3 Challenges and research objective... 8

Chapter 2 Fabrication of PZT thin-film actuators..12

2.1 Piezoelectric Materials 13

2.2 Fabrication of PZT thin films 17

2.3 MEMS device based on PZT thin-film 19

2.4 Micro-processing fabrication... 21

2.5 Backend fabrication.. 22

2.6 Mask preparation.. 24

2.6.1 Alignment mark design.. 24

2.6.2 Positions of the alignment marks 26

2.6.3 Mask fabrication 28

Chapter 3 Device testing 30

3.1Measurement of basic parameters 30

3.1.1 Capacitance measurement.. 30

3.1.2 Vibration measurement 31

3.1.3 Charge measurement.. 32

3.2 Performance Test.. 35

3.2.1 Actuator performance test... 35

3.2.2 Development of the experiment setup for sensor application............... 37

Chapter 4 FEA model 45

4.1 FEA model.. 45

4.2 Piezoelectric coefficient 48

Chapter 5 Dual top-electrode design 50

5.1 Introduction 50

5.2 Finite element analysis 54

5.2.1 Model development 54

5.2.2 Simulation results 55

5.2.3 Optimization study 57

5.3 Experiment verification 59

5.3.1 Specimen preparation 59

5.3.2 Experimental Setup and Results 60

5.3.3 Applications to Misaligned Microactuators 62

5.3.4 Effects of Warping 65

5.4 Summary 69

Chapter 6 Design and fabrication of probe device 70

6.1 Introduction 70

6.2 Dicing method and layout design 71

6.2.1 Dicing method 71

6.2.2 Layout design 73

6.3 Mask design 75

6.3.1 Top-side mask design 75

6.3.2 Back-side mask design 76

Chapter 7 Boundary conditions for probes 80

7.1 Simply supported boundary condition 81

7.2 Experiment under clamped-free boundary conditions 83

7.3 Calculation of the clamped-free boundary condition 85

7.4 Summary 84

Chapter 8 Parylene coated Probe working in fluid environment 86

8.1 Coating process of parylene 86

8.1.1 Parylene introduction 86

8.1.2 Effect of parylene coating thickness on displacement 89

8.1.3 Insulation effect of Parylene coating 92

8.2 Probe working in water over time 94

8.2.1 Displacement measurement in water 94

8.2.2 FRF test in water over time 95

8.2.3 Impedance test result 97

8.2.4 Discussion 98

8.3 Summary 102

Chapter 9 Conclusion and future works 103

Appendix A Fabrication Recipe of probe device 108

Bibliography 122

List of Figures

Fig. 1 A diagram of structures of human ear [1] 3

Fig. 2 A scanning electron migrograph of (a) the normal of hair cells and (b) the disruption and loss of hair cells [2] 3

Fig. 3 Cross section view of the spiral structure of the cochlea [3] 4

Fig. 4 An audiogram of the hearing rehabilitation strategy for various extents of hearing loss [4] 6

Fig. 5 Schematic drawing of the proposed HCI 8

Fig. 6 PZT thin-film probe with dual electrodes 10

Fig. 7 Perovskite structure of the PZT material [19] 15

Fig. 8 Phase diagram of PZT materials [20] 16

Fig. 9 The effect of the composition on the dielectric constant and the electromechanical coupling factor, k_p, in PZT ceramics [18] 17

Fig. 10 Schematic drawing of the PZT thin-film membrane actuator (not to scale) replot adding insulation later 19

Fig. 11 Fabrication processes of PZT thin film actuators. 22

Fig. 12. A diagram of the designed alignment mark (in mm) 25

Fig. 13. Schematic structures of the ABM aligner 27

Fig. 14 Schematics for a single-end charge amplifier 33

Fig. 15 Comparison of 60 Hz noise under different parameters 34

Fig. 16. Experiment setup for measurement of actuator performance 36

Fig. 17. Actuator die tested under different boundary conditions 37

Fig. 18. Experiment setup for sensor application 38

Fig. 19. Initial sensor measurement results 39

Fig. 20. Comparison of Grounding Patterns 39

Fig. 21. Comparison of noise under different grounding patterns 40

Fig. 22. Displacement measurement over the PZT thin-film surface 41
Fig. 23. Comparison of charge measurements (Ch1) by single end charge amplifier with (left) / without (right) sensor.. 42
Fig. 24. Comparison of charge measurements (Ch1) by differential charge amplifier output with (left) / without (right) sensor 43
Fig. 25. The experiment setup of the impulse response measurement 44
Fig. 26. Impulse response measurement result... 44
Fig. 27 A diagram of the finite element model and its components 45
Fig. 28 SEM photo of the silicon residue 46
Fig. 29 Comparison of normal strain in the radial direction at the top surface of the passive silicon 53
Fig. 30 Comparison of the displacement of the single and dual top-electrode design 56
Fig. 31 Comparison of the normal strain along the thickness of the diaphragm 57
Fig. 32 Actuator displacement with respect to the seize of center electrode........... 58
Fig. 33 Actuator displacement with respect to the size of the outer electrode 59
Fig. 34 Microscope picture of the actuator 60
Fig. 35 Schematics of the experiment setup 61
Fig. 36 Displacements under excitation with different phase differences 62
Fig. 37 Microscope picture of the misaligned actuator.. 63
Fig. 38 Displacements under excitation with different phase difference (misaligned actuator) 64
Fig. 39 3D Profile picture of the warped actuator 65
Fig. 40 Actuator excited by both electrodes (in phase) 66
Fig. 41 Actuator excited by both electrodes (out of phase) 66

Fig. 42 Displacements under excitation with different phase difference (warped actuator) 67
Fig. 44 A schematic of square array layout design 73
Fig. 45 A schematic of radial array layout design 74
Fig. 46 Top-side mask design 76
Fig. 47 Backside DRIE mask 77
Fig. 48 Backside DRIE mask zoom in (μm) 78
Fig. 49 Separating effect of the etching lines of 10 μm in width 79
Fig. 50 Separating effect of the etching lines of 200 μm in width 79
Fig. 51 FEA result of the probe strain 81
Fig. 52 Typical frequency response under the clamped boundary condition 81
Fig. 53 Simple supported boundary condition with blue tape 82
Fig. 54 Measurement results of the simple supported boundary condition 83
Fig. 55 Clamped-free boundary conditions of different fixed lengths with epoxy... 84
Fig. 56 Experiment results of the clamped-free boundary conditions 85
Fig. 57 Schematics of geometry limits 86
Fig. 58 Parylene coating process [50] 89
Fig. 59 Repeating units of three types of parylene 90
Fig. 60 Displacement ratio in respect to the coating thickness 91
Fig. 61 Parylene coating on different surfaces 92
Fig. 62 Parylene coating thickness measurement 93
Fig. 63 The impedance variation in DI water over time for the bare probe 95
Fig. 64 The impedance variation in DI water over time for the parylene coated probe 96
Fig. 65 Displacement (3 kHz) variation in DI water over time 98
Fig. 66 Resonance frequency in water over time 99

Fig. 67 SEM picture of the porous structure of the PZT surface 101

Fig. 68 SEM picture of the porous structure of the top electrode surface 102

Fig. 69 Impedance after the probe is out of the water 103

List of Tables

Table 1 Comparison of different piezoelectric materials.. 15

Table 2 Calculation and experiment results of the resonance frequencies 87

Table 3 Properties of parylene materials 90

Table 4 FRF comparison before and after parylene coating.................................... 94

Table 5 Displacement at 3 kHz in water over time (1st time) 97

Chapter 1 Introduction

1.1 Sensori-neural hearing loss and rehabilitation

Hearing loss is the total or partial inability to hear sound in one or both ears. It falls into two major categories, conductive hearing loss and sensori-neural hearing loss. In general, the human ear consists of three parts: the outer ear, the middle ear, and the inner ear (Fig. 1). The sound waves collected by the outer ear go through the external canal and hit the tympanic membrane (eardrum), which cause the tympanic membrane to vibrate. The vibration of the tympanic membrane is transmitted to the oval window of cochlea by three linked bones (malleus, incus, and stapes), which are connected to the eardrum in the middle ear. In the inner ear, the cochlea has thousands of hair cells (stereocilia) inside the spiral-shaped (two and half turns) cavity filled with fluid. The pressure waves in the cochlea canals (scala) caused by the movement of the stapes will stimulate the mechanoelectric exchange in hair cells, which generates electrical excitation in the auditory nerve. Conductive hearing loss usually occurs in the outer or middle ear when the transmission of sound vibrations cannot reach the inner ear due to obstacles in the ear canal, holes in the tympanic membrane, or fluid behind the eardrum. Sensori-neural hearing loss occurs in the inner ear when the sound vibrations are unable to be converted into electrical signals. The major reason for sensori-neural hearing loss is the dysfunction or loss of hearing hair cells in the cochlea, which is common in both aging seniors and people who work in loud environments for prolonged periods of time. Fig. 2 shows the normal orderly arranged hair cells on an apical region of the cochlea (a), and the disruption and loss of hair cells in the basal region of the cochlea after exposure to 90 dB noises for 8 hours (b).

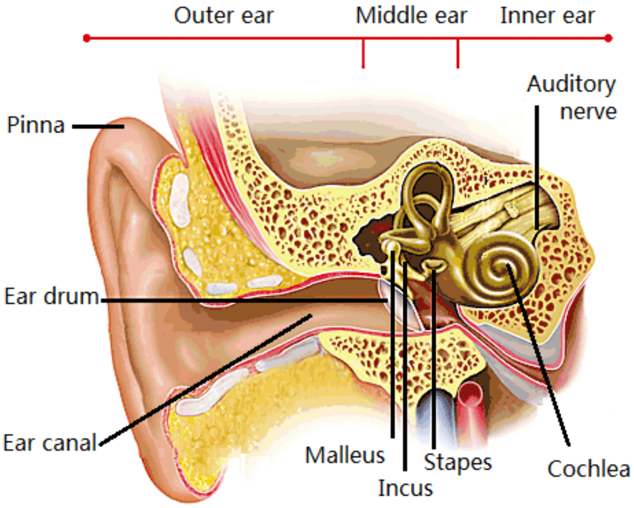

Fig. 1 A diagram of structures of human ear [**Error! Reference source not found.**]

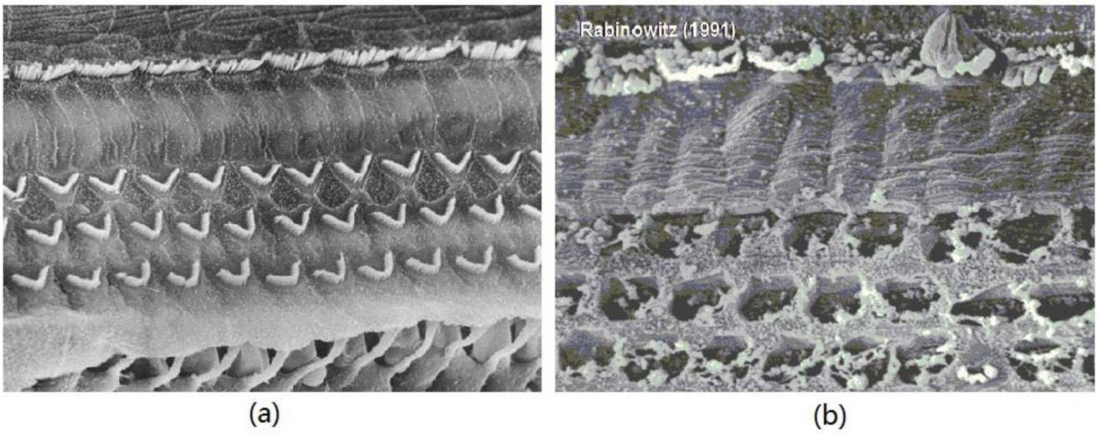

(a) (b)

Fig. 2 A scanning electron migrograph of (a) the normal of hair cells and (b) the disruption and loss of hair cells [**Error! Reference source not found.**]

Although Sensori-neural hearing loss is permanent because hair cells do not regenerate, it often gradually develops from the high frequency range to the entire audible range. Due to the special structures of cochlea, sound with different pitches will cause resonance at different regions of cochlea (Fig. 3). The membrane in the cochlea and the fluid around it can be thought of as a “mass-spring” system. The basal region near the oval window, due to the thicker membrane and smaller fluid mass, is associated with the hearing of high frequency sound crucial for speech recognition, such as the t- and s-sounds. The apical region of the cochlea coil has a thinner membrane and larger fluid mass; hence, it is associated with hearing in the low frequency range. Because sound waves reach the basal region first, damage to the hair cells often start from the high frequency region and may progress to the low frequency region with time.

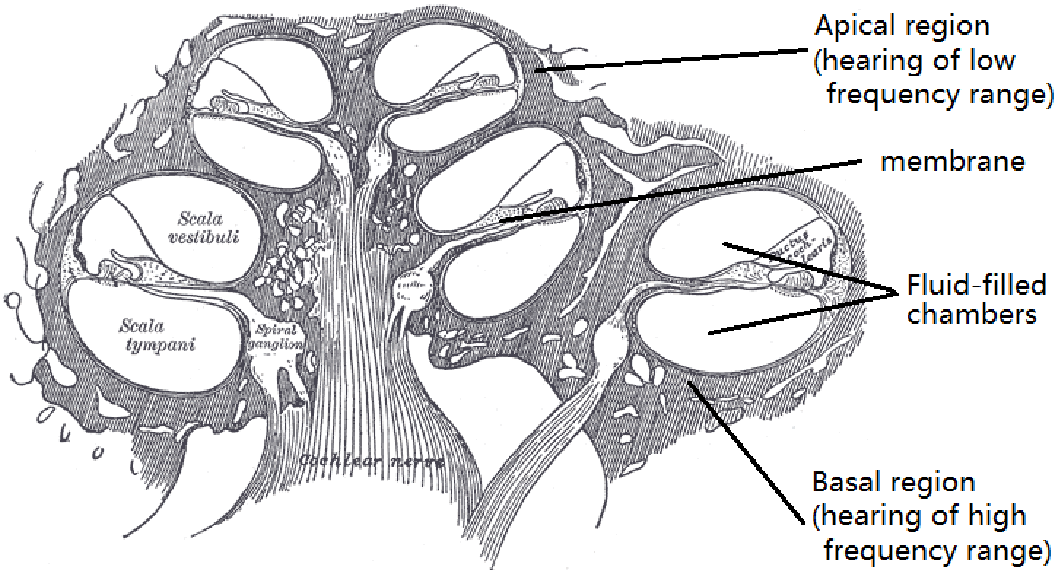

Fig. 3 Cross section view of the spiral structure of the cochlea [**Error! Reference source not found.**]

The strategy of hearing rehabilitation is shown in Fig. 4, where the horizontal axis is the frequency and the vertical axis is the hearing threshold level, in dB. For people who only have mild hearing loss in the high frequency range, traditional hearing aids can help them by amplifying the sound level. For people with severe to profound hearing loss in the entire frequency range, cochlea implants can rehabilitate their hearing by stimulating the nerve directly by electric signals transmitted from an outside microphone. However, a large group of people fall into the group of partial hearing loss, who have severe hearing loss in the high frequency range, while still retain some degree of hearing in the low frequency range. Although the size of this group continues to increase, unfortunately, neither traditional nor cochlea implants are well suited for them, because traditional hearing aids only have marginal rehabilitation effects in the high frequency range, while surgery for the cochlea implant runs the risk of damaging preserved hearing in the low frequency range.

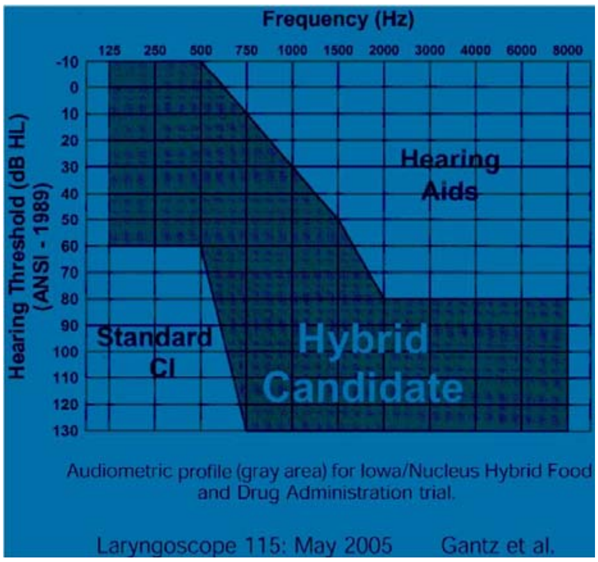

Fig. 4 An audiogram of the hearing rehabilitation strategy for various extents of hearing loss **Error! Reference source not found.**

Recently, it was found that the trend of combining electrical and acoustic stimulation (CEAS) is the most effective rehabilitation solution for people with partial hearing loss. The general idea is to stimulate the high frequency region of cochlea electrically with a shortened electrode, which can reduce the risk of hurting the low frequency region. Simultaneously, stimulation is acoustically delivered to the apical low frequency region by a traditional hearing aid. Clinical trials show that CEAS can provide people of partial hearing loss with a better appreciation of aesthetic qualities of sound and speech recognition in noisy backgrounds, especially when compared to hearing aids or cochlear implants alone [**Error! Reference source not found.-Error! Reference source not found.**].

1.2 Proposed application of hybrid cochlea implant hearing aid

Current CEAS relies on separate devices, such as: a cochlea implant and a hearing aid. This strategy causes coordination problems between devices, such as feedback effects or requiring the patient to make inconvenient continual device adjustments. Furthermore, the outside hearing aid receiver does not overcome the side effects of blocking the ear canal which may cause compromises in sound quality, discomfort, and infections.

According to clinical needs, a hybrid cochlear implant (HCI) hearing aid is proposed to integrate the acoustic and electrical components into a single device. As shown in Fig. 5, the HCI consists of a shortened electrode array and a PZT thin film acoustic actuator. The electrode array will restore hearing in the high-frequency range, much like a traditional cochlea implant. The novel intracochlea acoustic actuator near the basal region will generate pressure waves, which propagate to the apical region through the perilymph fluid to restore hearing in the low frequency range. A speech signal processor would control the coordination between the acoustic and electric components.

If proven to be feasible, the HCI approach will have a number of advantages over existing technologies. It will have the capability to fit specific needs of each patient over the entire frequency range. In addition, it will avoid the side effects of traditional hearing aids. As a single device, it will also provide convenience to patients, as they will not be required to spend effort toward device maintenance or continual adjustments. Moreover, the HCI may alter the developing direction of hearing rehabilitation by bypassing the outer and middle ear with a direct drive device.

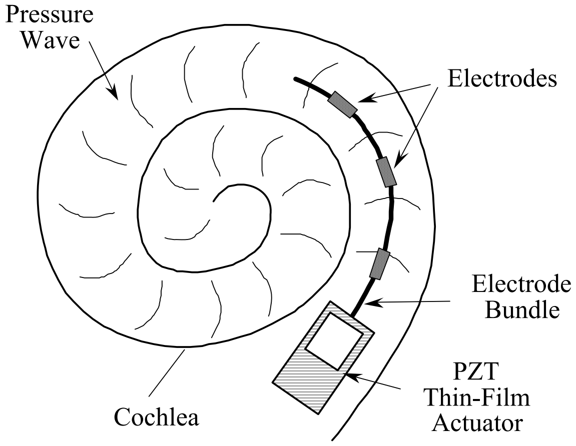

Fig. 5 Schematic drawing of the proposed HCI

1.3 Challenges and research objective

Although PZT thin-film actuators have been fabricated and studied for years on wafers, a major obstacle towards the application in hearing rehabilitation has been the availability of an acceptable intracochlear acoustic actuator for animal test, which can demonstrate the feasibility for the idea of HCI hearing aids. In particular, the research objective of this dissertation is to address three major challenges: performance, size, and the aqueous environment in the cochlea.

Challenge 1: Performance. Although the fabrication recipe is relatively stable, the performance of actuators is not always consistent. Manufacturing defects could significantly reduce the designed actuator displacement. For example, residual stresses, warping, non-uniform etching of the silicon diaphragm, and misalignment between the top electrode and the silicon diaphragm could all negatively influence the performance of the device. Moreover, these defects are neither predictable nor avoidable due to the limitation of the capabilities of equipments and the understanding of causes of these defects.

Challenge 2: Size. The cochlea is about the size of a pea. The actuator needs to have a maximum size of about 1 mm to be able to combine with a shortened electrode array to work in the basal region of cochlea together. The depth of the implantation must also be small to minimize the risk of damaging residual low-frequency hearing.

Challenge 3: Aqueous environment. The aqueous environment of the cochlea will challenge the intracochlea acoustic actuator in two ways. The perilymph fluid inside cochlea might short the electrodes of the actuator; or inversely, the electrolyte balance in the fluid might be affected by the electrical signals from the electrodes. Therefore, an insulation layer is needed to prevent the interaction between the electrodes and the fluid in the cochlea. Second, the actuator must be stiff enough to overcome fluid loading inside cochlea.

The research objective of this dissertation is to properly address the challenges outlined above in the following ways:

The first objective of this dissertation is to further improve the performance of the PZT actuator without changing existing fabrication recipes. Despite the various possible defects, current recipes have been proven to produce the best yield. A dual top electrodes design is proposed to enhance the displacement by making full use of the real estate of the PZT thin film.

The second objective of this dissertation is to fabricate the intracochlear probe, as shown in Fig. 6. The width of the probe tip must be about 1 mm to fit inside the scala tympani of the cochlea. Furthermore, the effect of the boundary condition on the performance of the probe also needs to be studied to find the appropriate setup for the following experiments and animal tests.

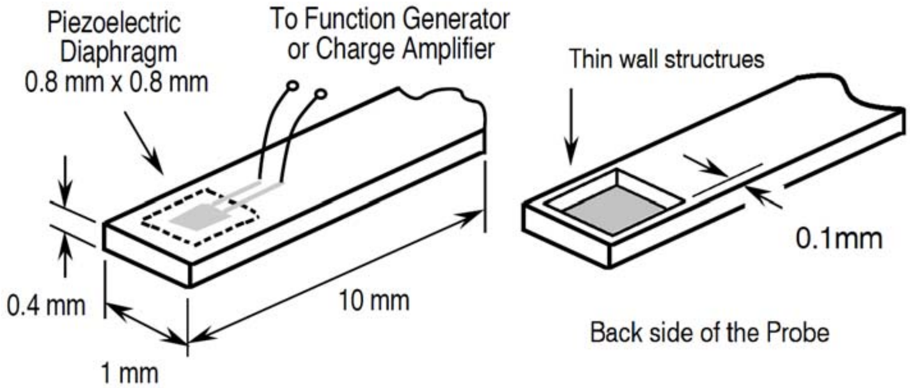

Fig. 6 PZT thin-film probe with dual electrodes

The third objective of this dissertation is to prove the insulation effect of the parylene coating. First, the proper coating thickness must be found to avoid sacrificing too much displacement. Second, the insulation effect of the parylene coating needs to be proved via both the displacement measurement and the impedance examination in the deionized water environment. As to concerns regarding the acoustic impedance, the PZT actuator can achieve 250 Gohm MKS at 1 kHz[**Error! Reference source not found.**], which exceeds the required 100 Gohm MKS [**Error! Reference source not found.-Error! Reference source not found.**].

An outline for this dissertation is provided as follows. First, the existing fabrication process, testing equipments and setups, and finite element analysis model of the PZT thin-film actuator is reviewed in Chapters 2-4. In Chapter 5, a new dual top electrodes design is introduced to improve the displacement by 30%. The effects of the dual top electrodes are studied by FEA and verified by the experimental results. The fabrication process and boundary conditions for the probe device is introduced in Chapters 6 and 7. The study of the effects of the parylene coating is introduced in Chapter 8, including how the coating thickness affects the displacement and the insulation effect when in a deionized water environment. It was found that the displacement will increase after the actuator is soaked in deionized water. The reason for this is also discussed in Chapter 8. Finally, Chapter 9 summaries the conclusions of this dissertation and future work.

Chapter 2 Fabrication of PZT thin-film actuators

Although fabrication recipes developed over the past ten years are relatively stable, in order to successfully fabricate devices with high yield and make minor modifications due to specific needs, it is necessary to understand the mechanisms behind PZT materials, the available options for the fabrication of PZT thin films, and their applications to the field of MEMS. These critical concepts are reviewed in more detail in Sections 2.1 to 2.3.

The specific fabrication process for our PZT thin-film device is reviewed in Sections 2.4 and 2.5, which are comprised of two parts: the micro-processing fabrication and the backend fabrication. The micro-processing fabrication is conducted in the class 10,000 cleanroom of University of Washington Microfabrication Facility (MFF). The deposition on the front side of the wafer includes an insulation layer, a bottom electrode, a PZT thin-film, and a top electrode. The thin-film structure is released by the substrate etching from the backside. The backend fabrication includes cutting the wafer into dices, making the electrical connections, and fixing the device with different boundary conditions.

In Section 2.6, mask preparation for lithography, especially the design of the alignment mark, is thoroughly introduced as the essential part of micro-processing fabrication, which is because the alignment between the backside cavities and the corresponding top electrodes can have significant effects on the performance of our device.

2.1 Piezoelectric Materials

A piezoelectric material is a material that generates electric charge on the surface in response to an applied stress, and conversely, develops a strain in response to an applied electric field. These are called positive and negative piezoelectric effects, respectively. The piezoelectric effect was first discovered in 1880 by French physicists Jacques and Pierre Curie.

To demonstrate the piezoelectric effect, the crystalline structure of the material needs to have an asymmetric center. The symmetric structures of crystals can be described by 32 possible point groups [**Error! Reference source not found.**]. 11 of the point groups are centrosymmetric. Out of the 21 non-centrosymmetric point groups, 20 of them are piezoelectric crystals. When mechanical stress is applied to the material, the deformation will cause the positive charge center to depart from the negative charge center. As a result, an electric dipole is generated.

Most piezoelectric materials used in MEMS are ferroelectric materials, which are only a subset of piezoelectric materials. Among the 20 piezoelectric point groups, 10 are called ferroelectric materials. Ferroelectric materials satisfy the following two prerequisites. First, the material has a spontaneous polarization. Second, the polarization can be oriented by applying an electric field and will remain oriented to some degree when the electric field is removed. These properties allow the ferroelectric material to be poled, in order to generate a larger net piezoelectric effect.

Piezoelectric materials can be classified into four types, including: poled polycrystalline ceramics (e.g., PZT and BST), single-crystal or highly oriented polycrystalline ceramics (e.g., zinc oxide and quartz), organic crystals (e.g., ammonium dihydrogen phosphate), and polymers (e.g., polyvinylidiene fluoride).

Different piezoelectric materials will generate different amounts of charge under the same mechanical stress. The ratio between generated electric charge density and applied mechanical stress is defined as the positive piezoelectric constant, in order to evaluate the linear intensity of the electromechanical interaction. Similarly, the negative piezoelectric constant is defined as the ratio between the generated mechanical strain and the applied electrical field. Because the mechanical strain has 6 degrees of freedom and the electrical field has 3 degrees freedom, the positive and negative piezoelectric constant is actually a 3 by 6 matrix and a 6 by 3 matrix, respectively. Detailed information regarding the piezoelectric constant is reviewed in Chapter 4. The piezoelectric constant of some piezoelectric materials are listed in Table 1. Different materials are favorable for different applications due to the specific requirements of the dielectric properties, elastic properties, and fatigue properties. However, a large piezoelectric constant is always desired, regardless of the application for the sensor or actuator.

Table 1 Comparison of different piezoelectric materials

Material	Formula	Form	Piezoelectric constant (pm/V or pC/N)
ADP / KDP	NH4H2PO4 / KH2PO4	Single crystal	48 / 21
Barium titanate	BaTiO3	Polycrystalline ceramic	200 ~ 500
PZT	PbZr0.6Ti0.4O3	Polycrystalline ceramic	100 ~ 500
PVDF	(CH2CF2)n	Oriented film	28
Quartz	SiO2	Single crystal	2.3
Zinc oxide	ZnO	Single crystal	1.2

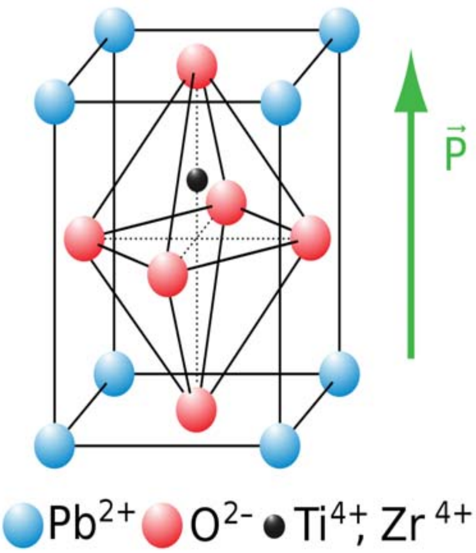

Fig. 7 Perovskite structure of the PZT material [**Error! Reference source not found.**]

PZT, as one of the most popular piezoelectric materials, is a binary solid solution of $PbZrO_3$ and $PbTiO_3$. These two crystals have perovskite structure with the chemical formula ABO_3. One cubic unit cell of PZT is shown in Fig. 7. Eight A(Pb^{2+}) ions sit at the cubic corners, with one B(Ti^{4+} or Zr^{4+}) ion located in the cubic body and six O^{2-} ions sit at center positions of six faces. Due to the relative size of the ions, Ti^{4+} or Zr^{4+} is stable at an off-center position. The resulting electric dipole will decide the spontaneous polarization orientation of the unit cell.

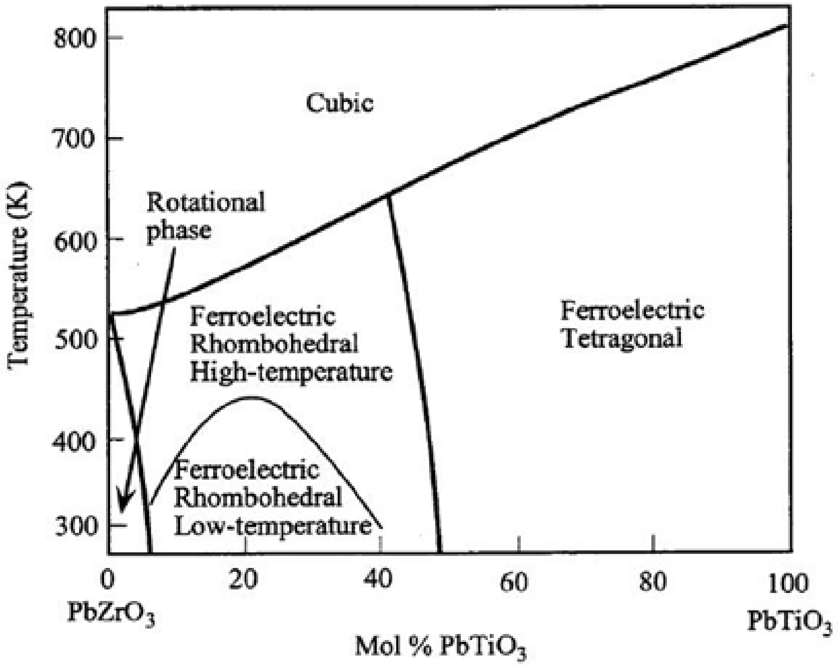

Fig. 8 Phase diagram of PZT materials [**Error! Reference source not found.**]

The piezoelectric property of PZT can be significantly affected by temperature and material composition. The phase diagram of PZT is shown in Fig. 8. At high temperatures, PZT has a centrosymmetric cubic perovskite structure with no piezoelectric properties. When the temperature is lower than the Curie point, the structure undergoes a phase transition to form the tetragonal or rhombohedral phase. The morphotropic phase boundary (MPB) separating the tetragonal and rhombohedral phases has a room temperature composition with a Zr/Ti ratio of about 52/48. PZT ceramics with the MPB composition have the best piezoelectric properties, as is shown in Fig. 9. The poling of the PZT ceramic is also easy at this composition because the spontaneous polarization within each grain can be switched to one of the 14 possible orientations (eight [111] directions for the rhombohedral phase and six [100] directions for the tetragonal phase).

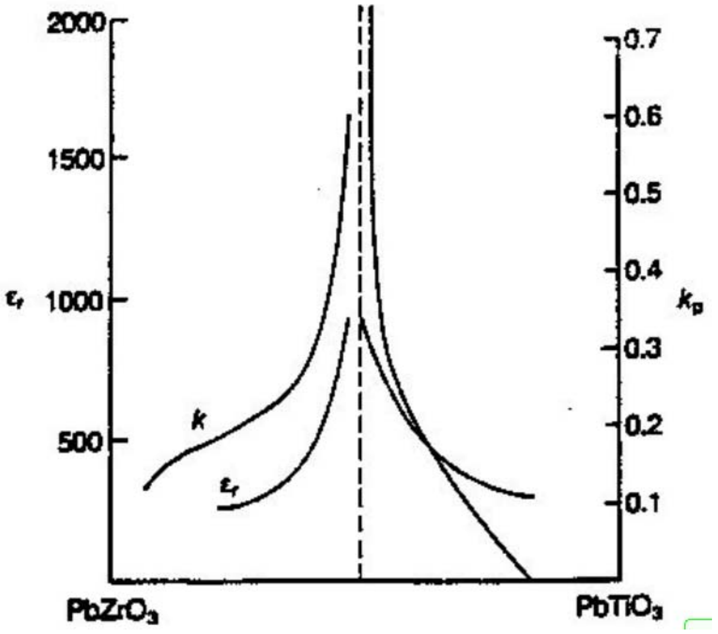

Fig. 9 The effect of the composition on the dielectric constant and the electromechanical coupling factor, k_p, in PZT ceramics [**Error! Reference source not found.**].

2.2 Fabrication of PZT thin films

Since PZT thin films offer tremendous potential for MEMS device applications, a number of deposition techniques are used to produce PZT thin films, including sputtering, metal organic chemical vapor deposition (MOCVD), pulsed laser deposition (PLD), and sol-gel methods.

Sputtering is widely used in early work because of high thin film quality and relative easy process. However, the control of composition is difficult and the deposition rate is slow [**Error! Reference source not found.**].

MOCVD is the most promising technology to deposit PZT thin films for many reasons, such as large deposition area with excellent conformal step coverage over a patterned substrate, a high deposition rate, good film uniformity, compatibility with current Si processes, and the possibility of relatively low temperature deposition. On the other hand, successful MOCVD processes require extremely complicated control over numerous processing parameters. The adjustment of physical and chemical environments highly relies on empirical methods [**Error! Reference source not found.**].

Compared to other techniques, PLD offers a prominent advantage of an independent controllability of the different process parameters [**Error! Reference source not found.**, **Error! Reference source not found.**] because there is no energy source in the deposition chamber and the short-wavelength pulsed laser is focused onto the target material from outside of the chamber [**Error! Reference source not found.**]. Moreover, the advantages of PLD include the capability of depositing PZT thin films at low substrate temperatures and high deposition rates [**Error! Reference source not found.**]. Nevertheless, the post-deposition temperature for annealing is significantly higher than that of the chemical solution deposition method [**Error! Reference source not found.**, **Error! Reference source not found.**].

The sol-gel method is a branch of chemical solution deposition. The precise control of the chemical composition, relatively low initial investment, large deposition area, and compatibility with local cleanroom facilities are the reasons of choosing this method for PZT thin film fabrication. The disadvantages of this method include low deposition rate, poor thickness uniformity, and high temperature post-deposition sintering.

2.3 MEMS device based on PZT thin-film

In the past few decades, Micro-Electro-Mechanical Systems (MEMS) based on lead zirconate titanate oxide (PZT) thin films have been intensively studied because of their large actuation strength, broad frequency bandwidth, and fast response. In this chapter, the general information related to this research is introduced, including the following aspects: piezoelectric materials, fabrication of the PZT thin-film, and typical PZT thin-film MEMS devices.

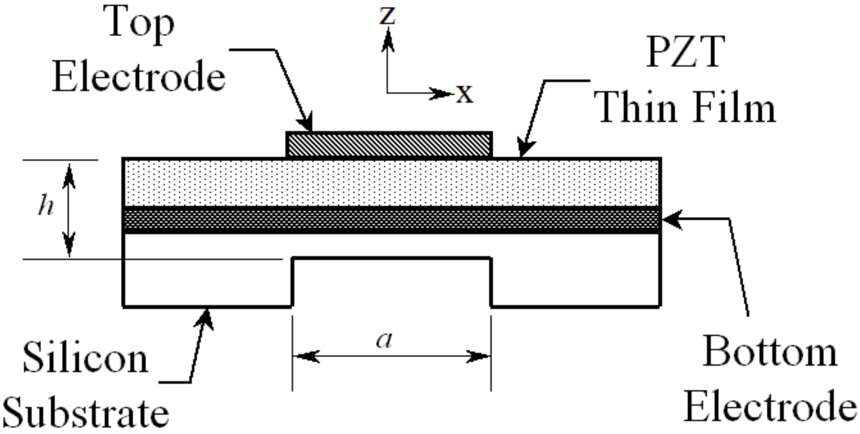

Fig. 10 Schematic drawing of the PZT thin-film membrane actuator (not to scale) replot adding insulation later

Lead-zirconate-titanate (PZT) thin-film microactuators often take the form of a membrane structure. Such membrane actuators typically consist of four parts: a diaphragm, a bulk silicon substrate, a PZT thin film layer, and a pair of electrodes, as is seen in Fig. 10 (note that the parts in Fig. 10 are not drawn in proportion). The diaphragm is a moving component of the actuator anchored to the silicon substrate. As a result of its small thickness, the silicon diaphragm has low structural stiffness when compared to the substrate. On top of the silicon diaphragm is a layer of PZT thin film with a pair of bottom and top electrodes. When a driving voltage is applied to the electrodes, the PZT thin film extends or contracts in the plane of the diaphragm, thus creating a bending moment to flex the diaphragm out of its plane. Such PZT thin-film membrane actuators have appeared in many applications, including micro fluidic devices (e.g., pumps and valves [**Error! Reference source not found.**], nozzles [**Error! Reference source not**

found.]), micro scanners [**Error! Reference source not found.**], micro-deformable mirrors [**Error! Reference source not found.**, **Error! Reference source not found.**], micro high fidelity speakers [**Error! Reference source not found.**, **Error! Reference source not found.**], micro protein desorption devices [**Error! Reference source not found.**], hybrid cochlear implant actuators [**Error! Reference source not found.**], and fuel cell membranes [**Error! Reference source not found.**]. In addition, similar structures are also widely used in various transducers, such as micro energy generators [**Error! Reference source not found.**, **Error! Reference source not found.**], micro mass sensing devices [**Error! Reference source not found.**, **Error! Reference source not found.**], ultrasonic transducers [**Error! Reference source not found.**], acoustic transducers [**Error! Reference source not found.**], and micro pressure sensors [**Error! Reference source not found.**].

2.4 Micro-processing fabrication

The fabrication process uses an improved sol-gel process that employs rapid thermal annealing and a dilute sealant coating, as is illustrated in Fig. 11. The silicon substrate is first oxidized in a furnace at 1045 °C for 2 hours to grow a 500 nm thick layer of SiO_2. Then, a 200 nm thick layer of silicon nitride is deposited by plasma enhanced chemical vapor deposition (Fig. 11 (a)). The bottom electrode consists of Pt/Ti layers, with thicknesses of 100 nm and 50 nm, respectively (Fig. 11 (b)). The PZT film is spin-coated three times. For the first two coatings, the sintering temperature is 650 °C for 15 minutes. For the third coating, the sol is diluted by 50% with acetic acid, and the sintering temperature is 450 °C for 10 minutes (Fig. 11 (c)). To fabricate the top electrodes, the conducting layers consisting of Au/Cr are deposited through evaporation (Fig. 11 (d)). The dual top electrodes are patterned and formed through lift-off (Fig. 11 (e)). Finally, the backside of the silicon is etched via a deep reactive ion etching (DRIE) to form the diaphragm suspension (Fig. 11 (f)).

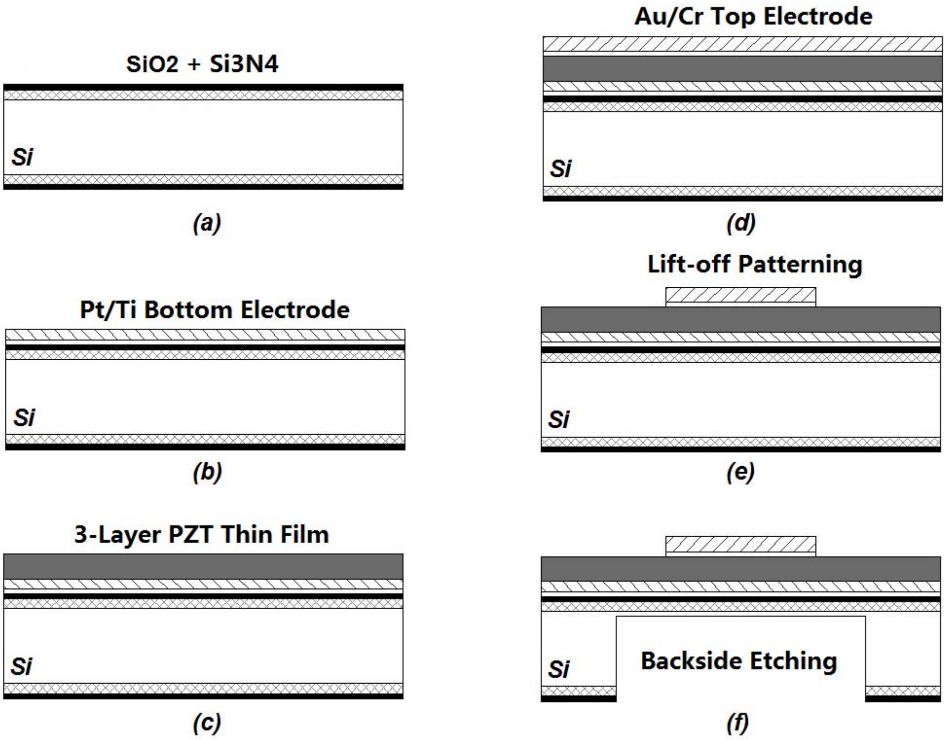

Fig. 11 Fabrication processes of PZT thin film actuators.

2.5 Backend fabrication

In order to have good yield and device performance, backend fabrication is as important as micro-processing fabrication. Based on experience, a lot of devices are damaged during backend fabrication.

A dicing saw is one of the most promising tools for cutting the wafer into dices with a high speed rotating thermocarbon blade. Because the saw in MFF is half automatic, the cutting process is more precisely controlled than manually cutting with a diamond pen. The cutting route can be aligned with a microscope, and the cutting depth has good consistency. However, there are also limitations with the dicing saw. Because the length of the cutting route is fixed to a distance longer than 3 inches, it is impossible to cut half of a wafer. Moreover, because the dicing process needs coolant and will generate a lot of silicon powder, there is considerable risk of contaminating the devices. The cutting width is another limitation that should be considered. The thinnest saw plate available is 0.2 mm. Because the saw will ruin the cross section of the sample, preparing cross section for the SEM observation must be done by hand.

For making electric connections, soldering is the first choice because of the reliable connection quality, although the top electrode will not be able to sustain a lot of contact and abrasion from the soldering pen. If the soldering wire with soldering aid is used, the soldering aid needs to be evaporated by the soldering pen for a while before it is placed close to the device. This can prevent the thin film from being contaminated by condensation of the soldering aid, which will cause extreme trouble in the following measurement of displacement by the laser interferometer. Sometimes, silver paste is another option for making electric connections, especially when the exposed electrode area is too small for soldering, for example, when making a connection for the bottom electrode from the cross section of the device. However, epoxy is needed afterward to stabilize the connection made by silver paste.

As for the boundary condition, epoxy is often used to glue the device or fix the electric connection due to its relatively high stiffness and good insulating properties. Clay and non-residual tape are some other options when temporary fixing is needed.

2.6 Mask preparation

In the micro-processing fabrication of our device, one mask is used to pattern the top electrodes, and the other is used to pattern the cavities on the backside. The shape and distribution of the top electrodes and the corresponding backside cavities depends on different applications; a design for the dual top electrodes probe device is introduced in Chapter 6 as a specific example. In addition to this, the design of an alignment mark is the third most important part of the mask preparation. The shape and position of alignment marks for both masks are thoroughly introduced in this section. Finally, the fabrication of the mask is also included.

2.6.1 Alignment mark design

The alignment mark always works in pairs. In our fabrication process, the first negative mark is deposited on the wafers through a lift-off process together with the top electrodes. The second positive mark is on the backside etching mask. Under an infrared microscope, the negative mark is bright within a dark background; In contrast, the positive mark is dark within a bright background. When the two masks are well aligned with each other, the sight of the microscope will be almost all dark, except for an even bright edge of the alignment mark (see the view part in Fig. 13) because the negative mark is purposely designed a bit larger. The gap between the negative and positive marks is 2.5 μm.

The shape of the alignment mark is shown in Fig. 12. The size of the center cross is 4.2 mm×14 mm. There are two 2 mm crosses beside the center cross. The function of these three larger crosses is to locate the mark and to make a rough alignment under the microscopes. The length and width difference of these three vertical lines can doubly assure the rough alignment by ensuring that the line in the positive mark is not aligned with the adjacent line in the negative mark when the view in the microscope only covers part of the alignment marks.

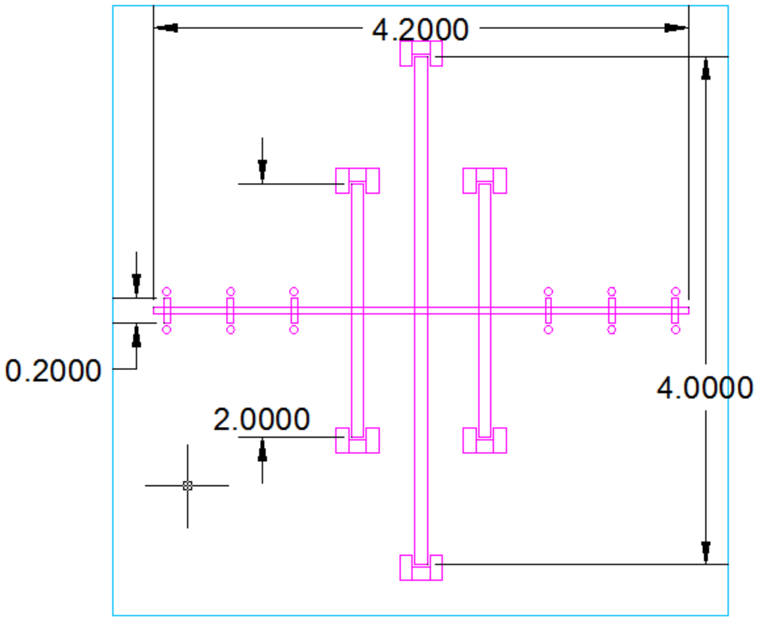

Fig. 12. A diagram of the designed alignment mark (in mm)

After the rough alignment, the fine alignment relies on the six smaller crosses on the two ends of the horizontal line, with a length of 0.2 mm. Three of these smaller features on each side will guarantee that we can find some valid marks even with some unexpected fabrication defects.

2.6.2 Positions of the alignment marks

To make a good alignment, at least two alignment marks are necessary. One confines the freedom of the translation, while the other confines the freedom of rotation. There are several restrictions that need to be considered when deciding the positions of the alignment marks.

The first restriction is the sight region of the infrared microscope. The structure of the infrared microscope is shown in Fig. 13. The infrared source is located underneath the mask and wafer. Two parallel infrared light beams generated by the convexes are observed by the microscope from the top view after going through the wafer and the mask.

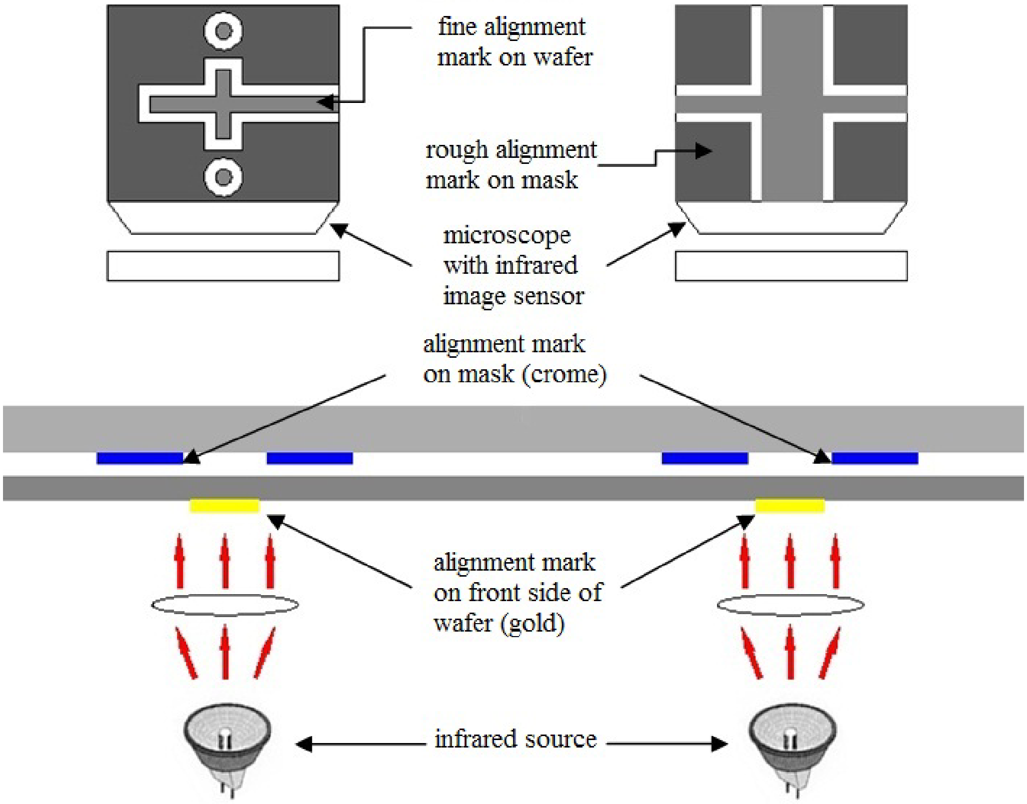

Fig. 13. Schematic structures of the ABM aligner

The second restriction relates to the pattern of the bottom electrode. Because the infrared light cannot pass through the bottom electrode, the region of the alignment mark needs to be protected from the deposition of the bottom electrode. This could be done by another lithography process. However, considering that the shape and position is not precisely required and the cost of time, the alignment mark region is protected by high temperature tape instead of photoresist. Regarding positions, the alignment marks can be anywhere within the region of the infrared sight.

The third restriction is the pattern of PZT thin film. The PZT layers need to be patterned for two reasons. First, it contains metallic elements. The alignment mark regions need to be transparent to infrared for alignment; second, part of the bottom electrode needs to be exposed to make the backend connection easier. During the research of this dissertation, the PZT layer is patterned by plastic tape. This is because photoresist cannot be cleaned without removing the PZT sol-gel in desired deposition region, therefore, will contaminate the high temperature sintering tube; In contrast, plastic tape can be easily removed while remain the PZT sol-gel in the desired deposition region for the high temperature sintering process. Since the tape will affect the thickness of the spin-coated PZT sol-gel in a region around its edge, the alignment marks (protection tape) can only be at the edge of wafers for an even thickness in designed regions of diaphragm.

2.6.3 Mask fabrication

The fabrication of chrome masks, including all four steps, is a standard lithography process. The first step is to expose the designed feature on the photoresist layer. The next two steps are to develop the photoresist with an appropriate developer and etch the chrome layer under the developed photoresist with a chrome etchant. The final step is to clean the undeveloped photoresist.

After the features on the mask are designed, two decisions need to be made before exposing the photoresist. First, if the mask is for operations on the front side of the wafers, the features need to be mirrored because the chrome side of the mask faces up during the exposure of the mask fabrication, while it faces down during the exposure for the lithography process of the wafer. The second decision is to determine if the exposure for mask fabrication needs to be inverted. For the mask of the top electrode fabrication, because negative photoresist is used for lift-off processes, the mask needs to be inverted. For the mask of the backside etching, the features do not need to be inverted.

Chapter 3 Device testing

After fabrication, device performance is tested through a series of experiments. The equipment and setup for each experiment is introduced in this chapter.

3.1Measurement of basic parameters

3.1.1 Capacitance measurement

Immediately after device fabrication, a rough test is conducted with the use of a multimeter. Because the defects of the PZT thin-film cannot be completely eliminated, the top and bottom electrodes of some devices will be shorted. The purpose of the rough test is to verify which devices are workable.

For the workable devices, the capacitance between the top and bottom electrodes is an important parameter to measure. When the device is tested as a sensor, the input capacticance of the charge amplifier should be selected according to the result of the measurement. When PZT material properties (e.g., the dielectric constant or the piezoelectric constant) need to be verified, the capacitance is also a necessary parameter.

The equipment we used to measure the capacitance is an Agilent 4294A precision impedance analyzer with text fixture 16047E. Although the equipment is very sophisticated and can perform all kinds of impedance measurements, we are only interested in the equivalent parallel capacitance and the quality factor in the swept frequency range from 100 Hz to 200 kHz. The equivalent series resistance can be calculated from these two parameters. The analyzer is able to be programmed to conduct automatic measurements. A program for automaticly measuring the capacitance is listed in Appendix B, which is used to monitor the change of capacitance over a long period of time, in accordance with the desired intervals.

3.1.2 Vibration measurement

The displacement of the PZT thin-film diaphragm is the second most important parameter that needs to be measured, whether the device works as an actuator or a sensor. The performance of an actuator, the sensitivity of a sensor, and the piezoelectric constant of the PZT thin-film are all directly related to the displacement. The displacement is indirectly measured by a Polytec laser Doppler vibrometer (LDV). The output signal is proportional to the velocity of the shining point. In all of our applications, the velocity will be sinusoidal.

Assume the velocity is:

$$\mathrm{v} = \mathrm{e}^{\mathrm{i}\omega\mathrm{t}}$$

The displacement is the integral of the velocity:

$$\mathrm{D} = \int \mathrm{e}^{\mathrm{i}\omega\mathrm{t}}\mathrm{dt} = \frac{\mathrm{e}^{\mathrm{i}\omega\mathrm{t}}}{\mathrm{i}\omega} = \frac{\mathrm{v}}{\mathrm{i}\omega}$$

Therefore, in order to measure the displacement, the corresponding frequency needs to be record as well.

According to the working principles of the vibrometer, good reflection is necessary for accurate measurements. Since the surface of the top electrode is normally a nice mirror, the focus distance and the direction of the laser beam become the two factors that determine the reflection quality, which is indicated by 10 green LED lights on the front panel of the optical fiber head. When 4 or more lights are off, the SNR and accuracy of the measurement output will be sacrificed.

The maximum output voltage of the equipment is 20 V, peak to peak. The measurement range depends on the selection of sensitivity (5, 25, or 125 mm/s/V). The built in low pass filter helps to get a clear output signal. When the resonant peak is observed, the cut-off frequency is set to 250 kHz; when the amplitude in the audible frequency range is interested, the cut-off frequency is set to 20 kHz.

3.1.3 Charge measurement

As the third most essential parameter for PZT thin-film diaphragm, the charge generated on the bottom and top electrodes are measured by a single-end charge amplifier CCA1000. The parameters need to be set before the measurement includes input capacitance, input resistance, and output gain.

To set these parameters correctly, the circuit of the charge amplifier, especially for the input gain part, needs to be understood. The schematic graph for the charge amplifier is shown in Fig. 14.

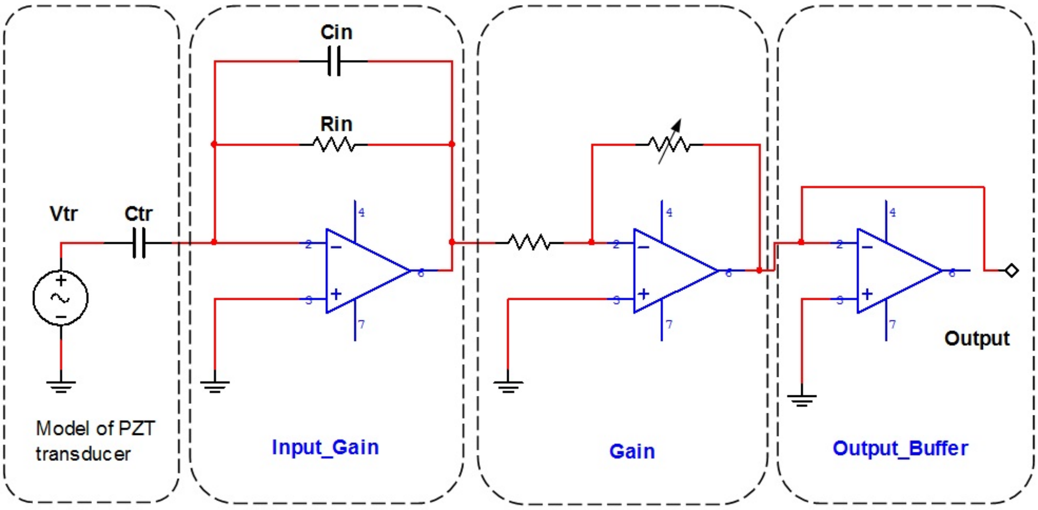

Fig. 14 Schematics for a single-end charge amplifier

The transfer function of the input gain part is:

$$A_{\mathrm{input}} = -\frac{Z_{R_{\mathrm{in}}//C_{\mathrm{in}}}}{Z_{C_{\mathrm{tr}}}} = -\frac{R_{\mathrm{in}}C_{\mathrm{tr}}}{\frac{1}{j\omega} + R_{\mathrm{in}}C_{\mathrm{in}}}$$

In the high frequency range, the term of "$C_{\mathrm{in}}R_{\mathrm{in}}$" dominates the value of the denominator; the input gain becomes the ratio between the capacitance of the transducer and the input capacitance. In the low frequency range, the term of "$\frac{1}{j\omega}$" dominates the value of the denominator; as the frequency decreases, the input gain decreases with a rate of -20dB. The cut-off frequency of the high-pass filter is $f_c = \frac{1}{2\pi R_{\mathrm{in}}C_{\mathrm{in}}}$.

Therefore, the charge is $Q_{\mathrm{tr}} = C_{\mathrm{tr}} \times V_{\mathrm{tr}} = C_{\mathrm{tr}}\frac{V_{\mathrm{out}}}{A_{\mathrm{input}} \times A_{\mathrm{gain}}}$.

The strategy for the parameter selection includes three steps. First, select the closest capacitance value to the capacitance of the PZT thin-film device. In this way, the output power from the device is maximized.

Second, select an appropriate input resistance to set the cut-off frequency higher than 60 Hz, because the single end amplifier is vulnerable to the common mode noise from the power line. A comparison among the different effects of different setups is shown in Fig. 15. A sample is tested without any stimulations; the output signal from the charge amplifier is shown in channel 3. The input capacitance was set to 22 pF. On the left side, the input resistance is 1 Gohm with a cut-off frequency of about 7.24 Hz; the noise of 60 Hz is obvious. On the right side, the input resistance was adjusted to 10 Mohm with a cut-off frequency of about 724 Hz. The noise of 60 Hz is filtered out effectively.

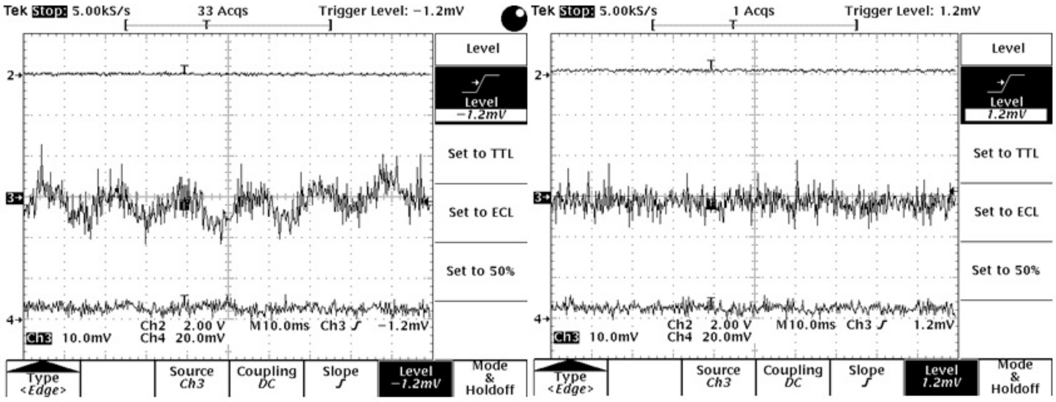

Fig. 15 Comparison of 60 Hz noise under different parameters

The last step is to select an appropriate output gain to make the amplitude of the output signal fall in the measurement range of the next equipment. Since the output signal from the PZT thin-film sensor is usually very small, 32 dB and 20 dB are the most common values used in related experiments.

3.2 Performance Test

After the preparation of the measurements of basic parameters, we are able to use a dynamic signal analyzer (SR785) to measure the device performance as a function of frequency.

The analyzer can output a standard sinusoidal wave as the reference frequency signal, and simultaneously, it will record signals from two channels. The amplitude ratio and phase difference at different frequencies between the two channels will be calculated automatically to generate the frequency response function (FRF) of the tested dynamic system from 100 Hz to 100 kHz. There are two types of setup to measure our device as an actuator or a sensor, respectively.

3.2.1 Actuator performance test

The setup to test the device as an actuator is shown in Fig. 16. The output reference signal first goes into a power amplifier. The amplified signal is applied to the top and bottom electrode to drive the PZT thin-film. It is also connected to channel A of the analyzer as the input signal of the system. The velocity measurement result from the LDV is connected to channel B as the output signal of the system.

Similar to the measurement of the displacement, the direct measurement result is the velocity of the diaphragm under the unit driving voltage at a certain frequency. We need to integrate to get the result of the displacement under the unit driving voltage. This parameter representing the performance directly is defined as the actuation constant of the device.

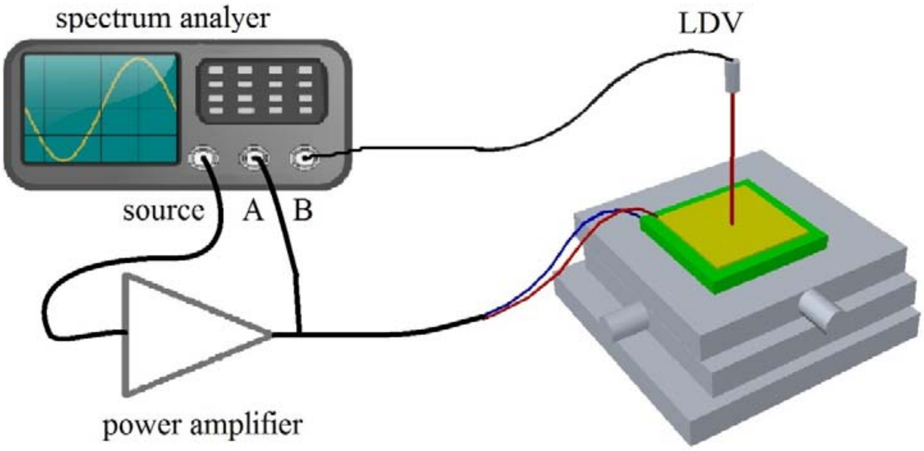

Fig. 16. Experiment setup for measurement of actuator performance

Other than the setup for the testing equipment, the boundary condition of the tested sample is also important for consistent measurement results. An actuator die cut from the wafer was tested five times with different boundary conditions. The schematic diagram and the measurement results are shown in Fig. 17. The actuator was first tested when simply placed on an aluminum block. The resonant frequency is higher than 100 kHz. The other four results are tested after each side of the die was glued to the substrate with epoxy. The resonant frequency drops to about 99 kHz with little difference among each other. Therefore, comparable measurement results should be taken under the same boundary conditions.

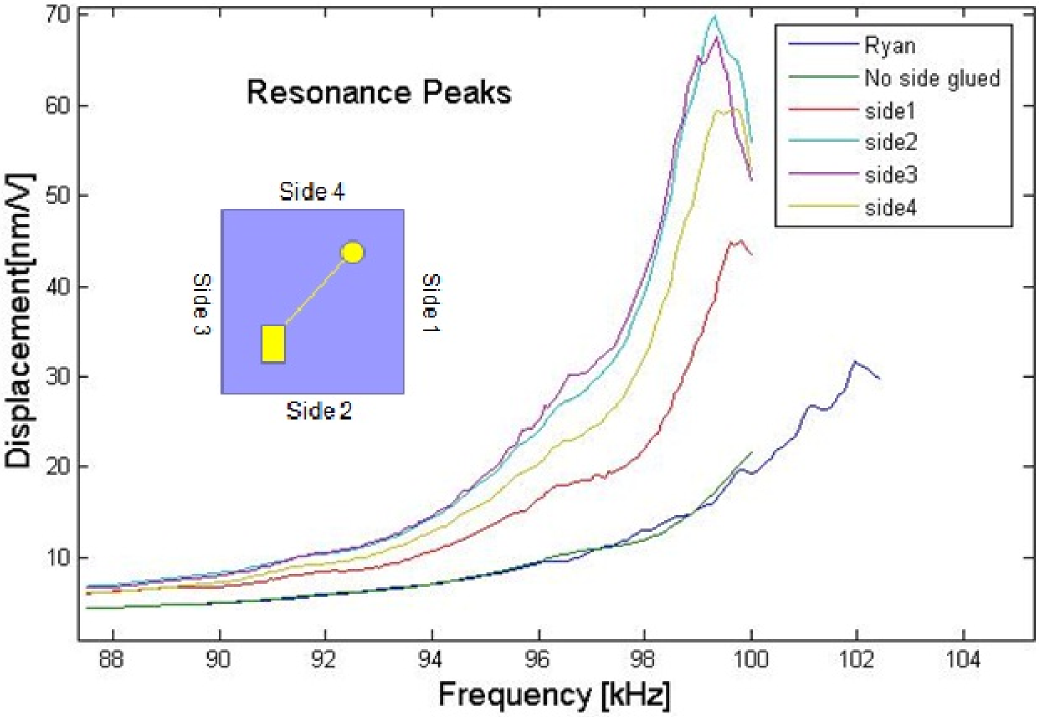

Fig. 17. Actuator die tested under different boundary conditions

3.2.2 Development of the experiment setup for sensor application

The setup to test the device as a sensor is shown in Fig. 18. The stimulation is from a speaker driven by the amplified frequency reference signal. The output charge is measured by the charge amplifier. The input signal of the system can either be the speaker's driving signal or the displacement measured by the LDV.

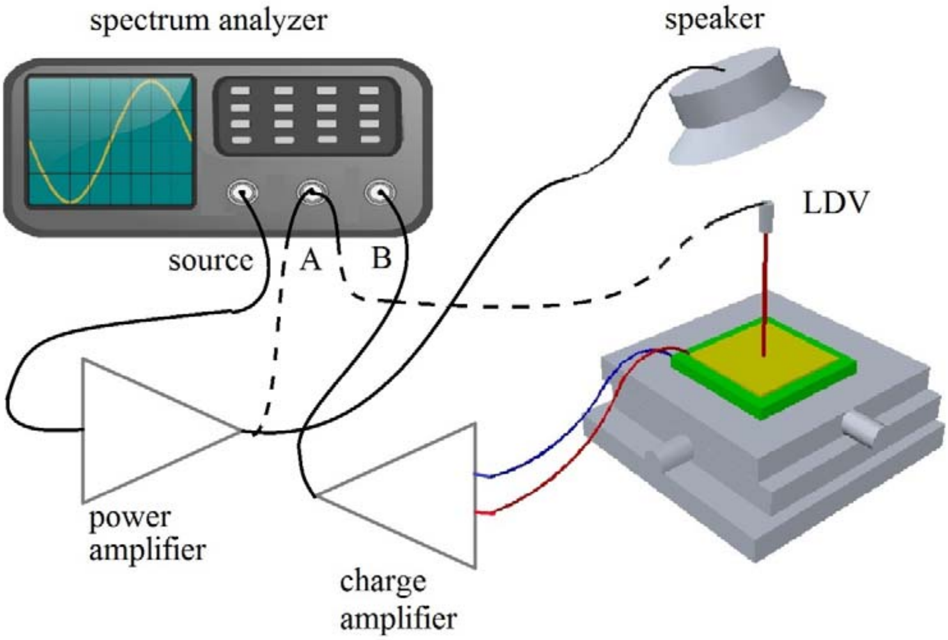

Fig. 18. Experiment setup for sensor application

The measured result is shown in Fig. 19. The signal in channel 2 is the output signal from the power amplifier, which drove the speaker. Channel 3 and channel 4 are the measurement results from the charge amplifier and the LDV. Although the average result (right) shows that the device is workable as a sensor, the direct measurement results (left) are very noisy because both the charge and velocity generated by the sound pressure are extremely small.

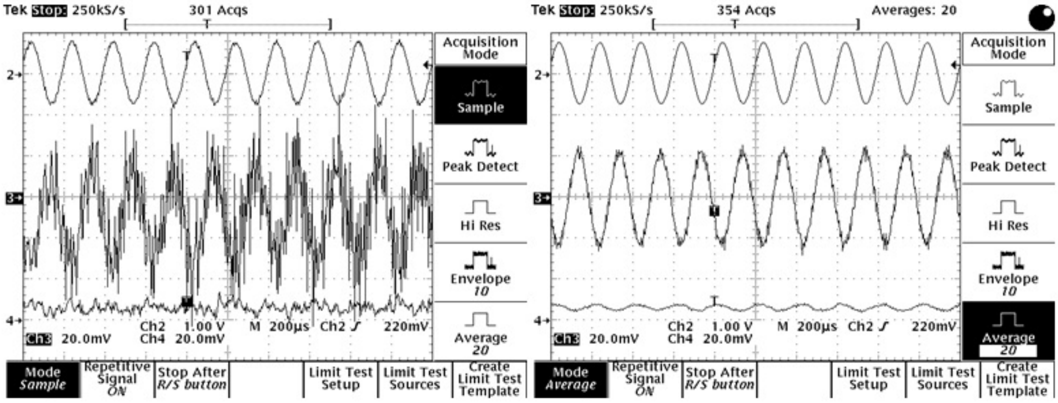

Fig. 19. Initial sensor measurement results

To reduce noise in the signals, the DC power supply of the charge amplifier was changed from a switching power supply to a lead-acid battery; all unshielded cables were shielded with foil paper and grounded. However, the reduction of noise is limited, as is shown in Fig. 21 (left).

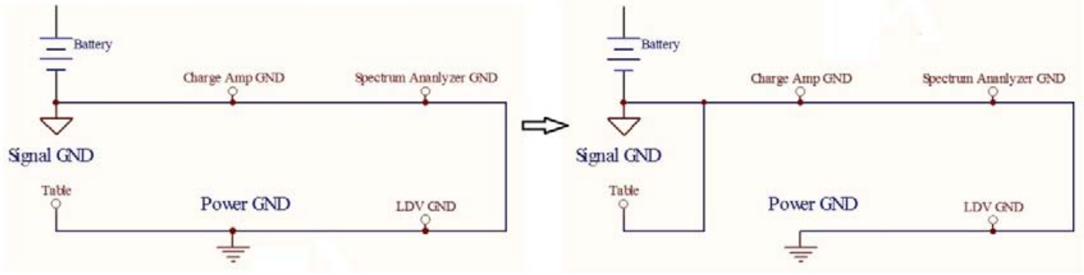

Fig. 20. Comparison of Grounding Patterns

Then, the grounding of the whole experiment setup was invested. The original pattern is shown in Fig. 20 (left). As the substrate for all equipments, the suspension table is grounded with the power supply, and it is far away from the signal ground. Because the ground of power is a common source of all kinds of noise, the table is connected to the ground of battery directly, as is shown in Fig. 20 (right). The significant reduction of noise is shown in Fig. 21 (right).

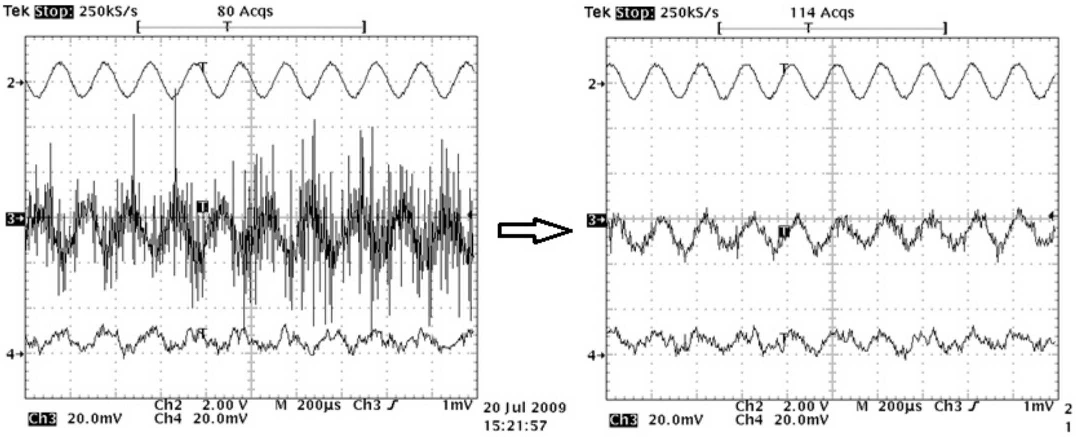

Fig. 21. Comparison of noise under different grounding patterns

To confirm that the measured signal is generated from the vibration of the PZT thin-film, two other experiments were conducted. The first experiment is the displacement measurement across the whole range of the thin-film while the speaker remains working. The result shown in Fig. 22 demonstrates that the thin-film is stimulated by the sound pressure at 4 kHz. The horizontal axis is the reading from the micrometer on the platform, in millimeters. The vertical axis is the displacement of the device surface, in nm.

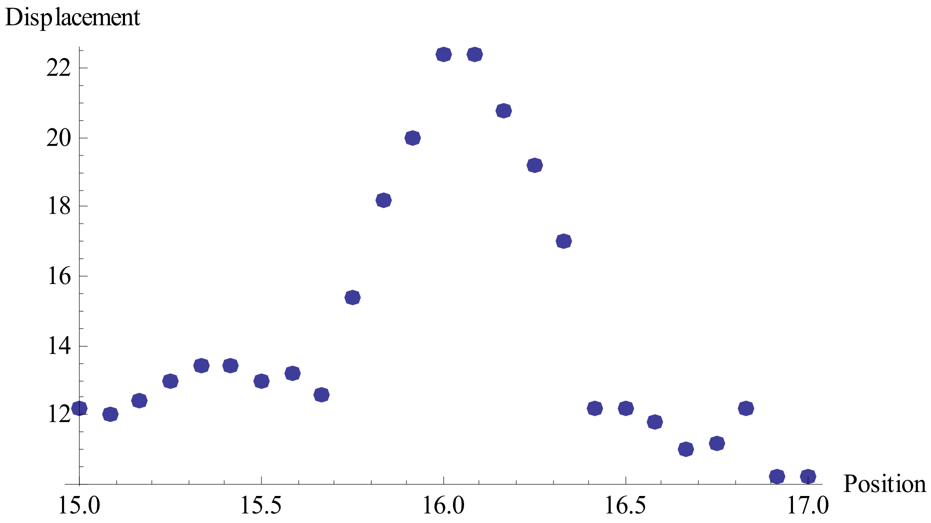

Fig. 22. Displacement measurement over the PZT thin-film surface

The second experiment is a comparison of the output from the charge amplifier with (left) and without (right) the sensor connected when the speaker remains operational. The result is shown in Fig. 23. Although the amplitude without the sensor connected decreased to about half, the output is obviously not from the piezoelectric effect of the thin-film. Since the frequency is consistent with the speaker, it is believed that the signal is picked up by the connection cable between the device and the charge amplifier as a common mode noise.

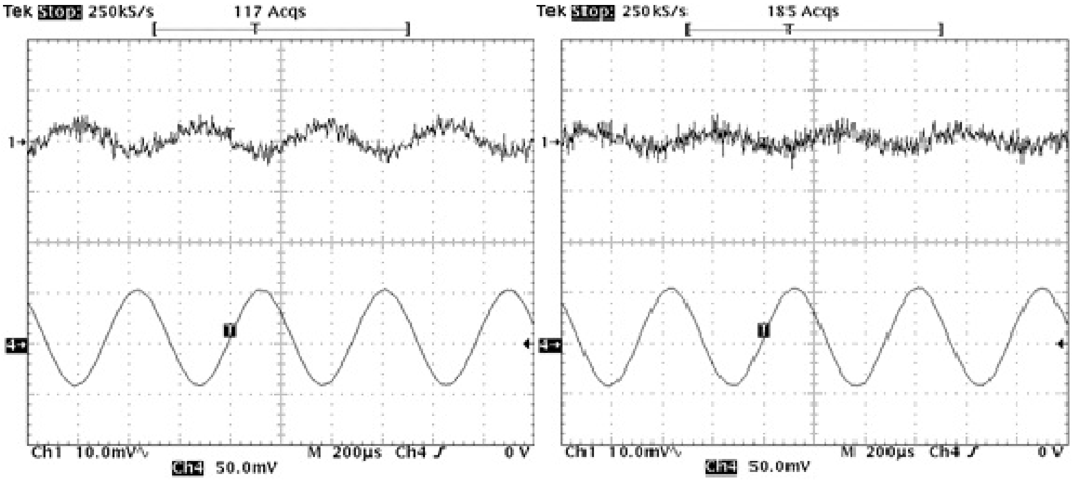

Fig. 23. Comparison of charge measurements (Ch1) by single end charge amplifier with (left) / without (right) sensor

In order to measure the charge generated purely by the PZT thin film, a differential charge amplifier with a 50 dB common mode rejection ratio is used instead of the single end charge amplifier. The result of the same comparison for the differential charge amplifier is shown in Fig. 24. There is no sinusoidal output signal when the sensor is disconnected.

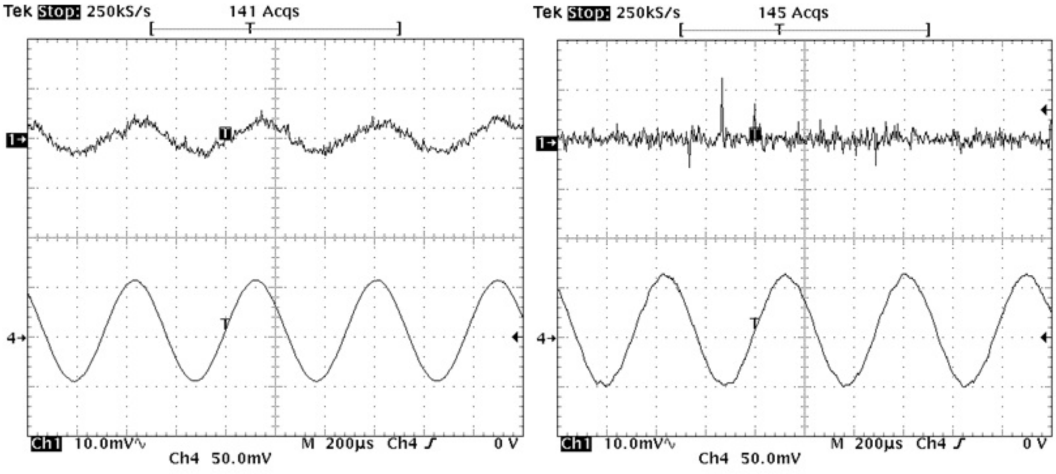

Fig. 24. Comparison of charge measurements (Ch1) by differential charge amplifier output with (left) / without (right) sensor

While different from the released PZT thin-film devices, the thin-film with silicon substrate can also work as a sensor, but its impulse response is of more interest than its frequency response. The setup of the experiment is shown in Fig. 25. The impulse stimulation is applied by a small hammer, and the force can be measured through a sensor inside the hammer. The generated charge can be measured by the single end charge amplifier.

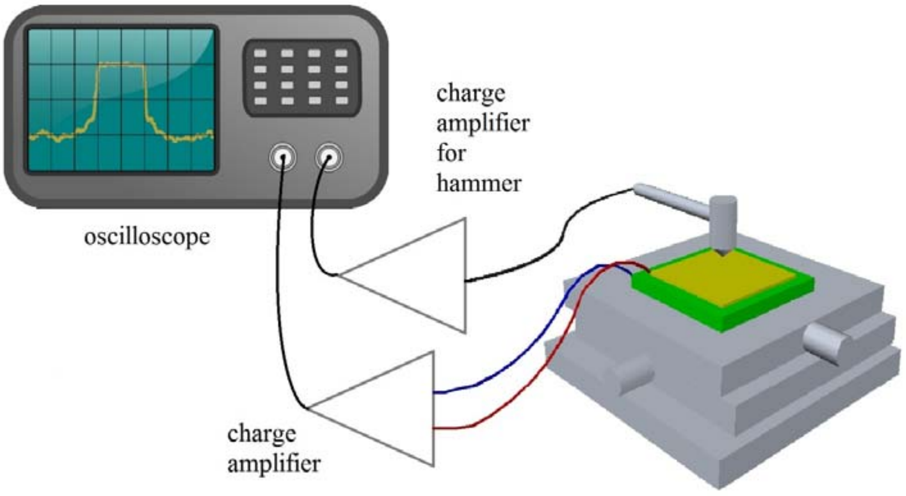

Fig. 25. The experiment setup of the impulse response measurement

One of the measurement results is shown in Fig. 26. Given the sensitivity of the hammer sensor and the capacitance of the device, a rough evaluation of the piezoelectric constant, d_{33}, can be made by simple calculations. For an accurate measurement of d_{33} from impulse response, calibrations need to be made due to different substrate effects. Detailed information is discussed in [**Error! Reference source not found.**].

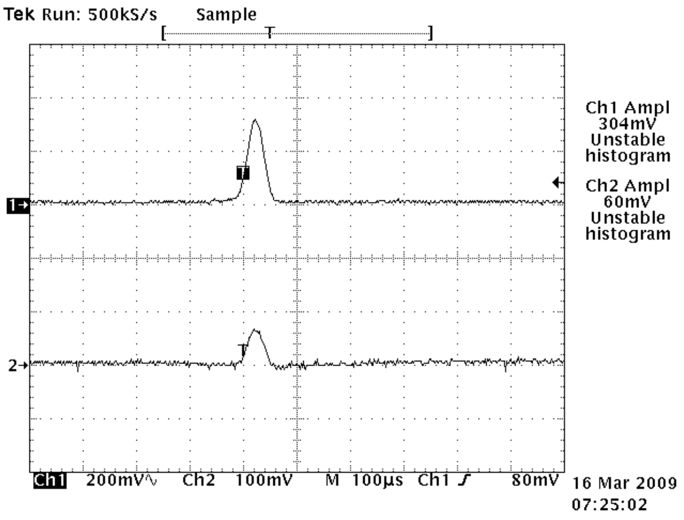

Fig. 26. Impulse response measurement result

Chapter 4 FEA model

4.1 FEA model

A one-eighth FEA model of the actuator is shown in Fig. 27. This model consists of six components: a silicon substrate, a passive silicon membrane, a silicon residue, a PZT thin film, and a pair of top and bottom electrodes. The silicon substrate has the dimensions of 3000 μm × 3000 μm, with a thickness of 400 μm. At the center of the substrate, a silicon block of 800 μm × 800 μm is removed to form the passive membrane, with a thickness of 0.4 μm.

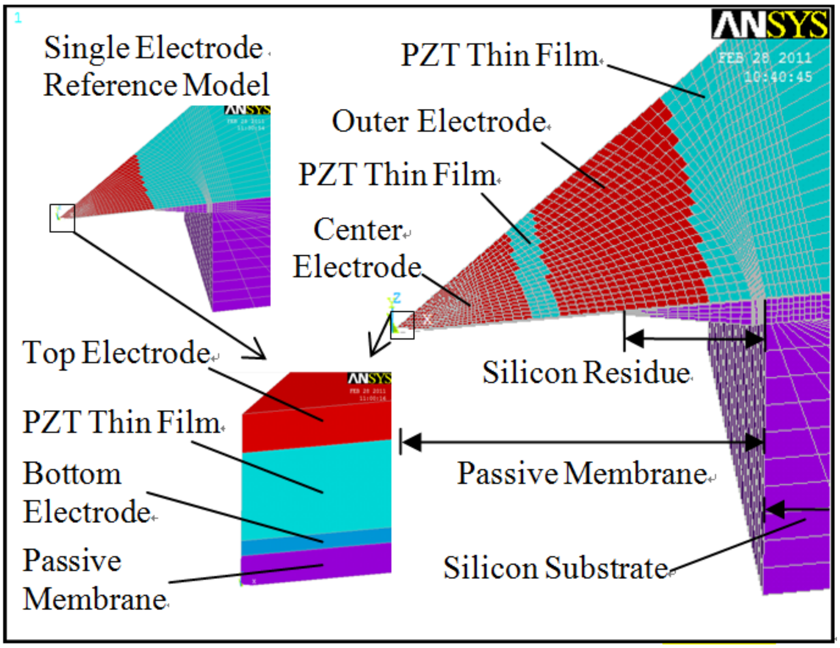

Fig. 27 A diagram of the finite element model and its components

The silicon residue is located below the passive silicon membrane. The silicon residue has a circular inner circumference and a square outer circumference. The inner diameter of the silicon residue varies from 500 μm to 700 μm depending on fabrication conditions. Moreover, the cross section of the silicon residue is trapezoidal with a constant slope measured from the SEM photo, as is shown in Fig. 28. As a result, the shape and volume of the silicon residue can be completely defined through the inner diameter. The nodes of the silicon residue are merged with the bottom surface of the passive silicon membrane and the inner circumference of the silicon substrate.

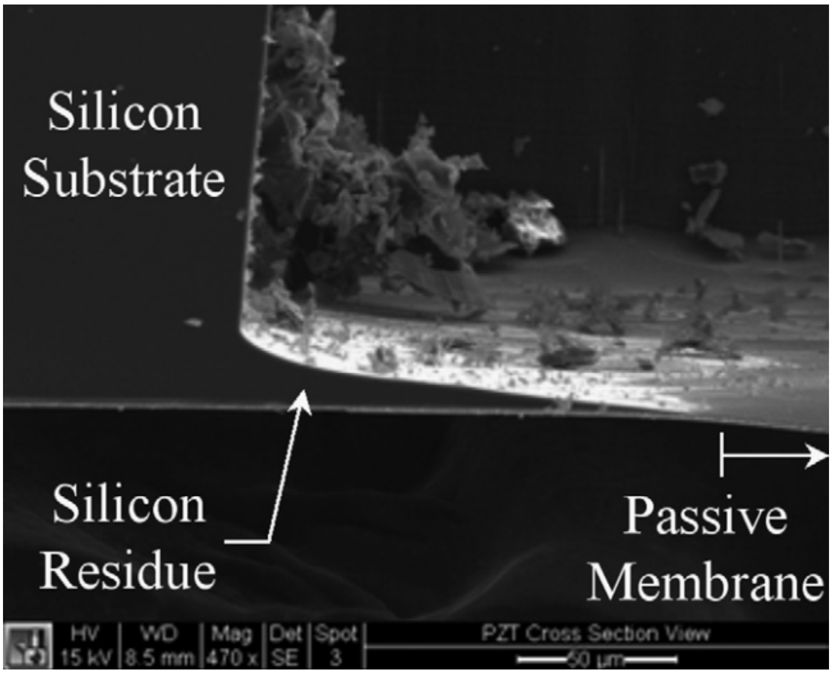

Fig. 28 SEM photo of the silicon residue

The silicon substrate, passive silicon membrane, and silicon residue are all meshed with 3-D linearly elastic solid elements. The bottom surface of the silicon substrate is subjected to geometrically fixed boundary conditions.

On top of the passive silicon membrane, there is a PZT thin film sandwiched between a bottom electrode and a top electrode. In addition, the bottom surface of the bottom electrode is fixed to the top surface of the passive membrane, as shown in Fig. 27. The PZT thin film, top electrode, and bottom electrode have a thickness of 1 µm, 0.5 µm and 0.5 µm, respectively. The PZT thin film and the bottom electrode span the entire top surface of the actuator, whereas the top electrode occupies an area of 400 µm × 400 µm at the center of the passive membrane (on the top surface of the PZT thin film).

The PZT thin film is meshed with 3-D coupled field solid elements that couple electric, piezoelectric, and structural fields. The electrical potential of the nodes interfacing the top electrode are coupled together. A constant voltage is applied to serve as an electrical boundary condition. An identical setup is made for the nodes interfacing the bottom electrode. Material properties of the bulk PZT (PZT-4) are assumed, because exact material properties of the PZT thin films remain unknown and could depend significantly on the fabrication process and quality of the films.

The top and bottom electrode are meshed with 3-D linear elastic solid elements (i.e., same as the silicon substrate and passive membrane). The nodes at the interfaces of the PZT thin film and electrodes are merged together, and so are the nodes at the interface between the bottom electrode and the passive membrane. It is not necessary to consider electrodynamics within the electrodes, because the electrodes will reach an electric equilibrium much faster than the actuator reaches a mechanical equilibrium. Therefore, only the mechanical properties of the two electrodes are needed in the model.

A linear static analysis is then conducted to predict the deflection of the passive membrane. Since the lowest natural frequency of this finite element model is above 50 kHz, harmonic response of the actuator substantially below the first natural frequency (e.g., audio frequency range) can be predicted via static analysis to reduce computational efforts.

Using the same model, the device working as a sensor can also be analyzed. The difference is that the mechanical boundary condition needs to be given before the model is solved. Normally, a constant pressure can be applied as the boundary condition to evaluate the sensitivity of the sensor.

4.2 Piezoelectric coefficient

As mentioned in Chapter 1, the Piezoelectric effect is a coupled relationship between the mechanical and electric status. Each status has two sets of parameters, as is listed here: T is the mechanical stress (6×1 vector); S is the mechanical strain (6×1 vector); D is the electric displacement (3×1 vector); and E is the electric field (3×1 vector). The constitutive relationship is usually expressed as below:

$$\{\mathrm{S}\} = [\mathrm{s}^{\mathrm{E}}]\{\mathrm{T}\} + [\mathrm{d}]\{\mathrm{E}\}$$

$$\{\mathrm{D}\} = [\mathrm{d}]^{\mathrm{t}}\{\mathrm{T}\} + [\varepsilon^{\mathrm{T}}]\{\mathrm{E}\}$$

In the above equations, $[s^E]$ is the compliance (6×6) matrix evaluated at a constant electric field; [d] is the piezoelectric (6×3) matrix relating the strain/electric field; $[d]^t$ is the transposed [d] matrix and $[\varepsilon^T]$ is the dielectric (3×3) matrix evaluated at constant stress.

However, there exists another way to express the constitutive relationship:

$$\{T\} = [c^E]\{S\} - [e]\{E\}$$

$$\{D\} = [e]^t\{S\} - [\varepsilon^S]\{E\}$$

In the second set of constitutive equations, $[c^E]$ is the stiffness (6×6) matrix evaluated at the constant electric filed; [e] is the piezoelectric (6×3) matrix relating the stress/electric field; $[e]^t$ is the transposed [e] matrix; and $[\varepsilon^S]$ is the dielectric (3×3) matrix evaluated at constant stress.

In order to make finite element analysis valid, the material parameter input to Ansys should be consistent and correct. The conversion equations for the piezoelectric properties can be reached by simple manipulation of the above equations. The result is as follows:

$$[c^E] = [s^E]^{-1}$$

$$[\varepsilon^S] = [\varepsilon^T] - [d]^t[s^E]^{-1}[d]$$

$$[e] = [s^E]^{-1}[d] = [d]^t[s^E]^{-1}$$

Chapter 5 Dual top-electrode design

The purpose of this chapter is to develop a dual top-electrode design to enhance the actuator displacement. In this design, the top electrode consists of two disconnected (thus independent) electrode areas, while a continuous bottom electrode serves as the ground. The two top electrodes are located in two regions with opposite curvature when the diaphragm deflects. When the two top electrodes are driven in an out-of-phase manner, the actuator displacement is enhanced. Both finite element analyses and experimental measurements confirm the feasibility of this design. When manufacturing defects are present, experimental results indicate that the actuator displacement can be optimized by adjusting the phase difference between the dual top electrodes.

5.1 Introduction

For almost all PZT thin-film actuators, it is important to maximize the actuator constant, which is defined as the displacement generated per unit of voltage applied. For example, microactuators that generate acoustic pressure waves in intracochlear applications have a specification of 200 nm in displacement. If the actuator constant is large, only a small voltage is needed to drive the actuator to achieve the desired displacement.

In fabricating the PZT thin-film microactuators, there are many factors that could significantly reduce the actuator constant from its designed value. For example, residual stresses are unavoidable during the fabrication because the high sintering temperature of the PZT thin films together with a tiny mismatch of coefficient of thermal expansion can result in huge residual stresses in the actuator [**Error! Reference source not found.-Error! Reference source not found.**]. The presence of the residual stresses will significantly stiffen the diaphragm and reduce the actuator constant. As another example, the diaphragm is often fabricated by etching away part of the bulk silicon substrate from the bottom. The etching is seldom uniform, resulting in residual silicon at the junction of the diaphragm and the silicon substrate [**Error! Reference source not found.**]. The residual silicon increases the diaphragm thickness and stiffens the actuator, thus reducing the actuator constant.

To increase the actuator constant, the current practice is to optimize the relative size of the top electrode to the residual silicon [**Error! Reference source not found.**]. Both the simulation and experimental results indicate that the actuator constant reaches its maximum when the size of the top electrode is roughly 60% of the size of the residual silicon. This design, however, has several drawbacks. First, this design has only one top electrode spanning partially over the diaphragm structure. Therefore, the real estate of the actuator is not fully utilized to increase the actuator constant. Second, the top electrode is optimized with respect to the residual silicon, which may vary from batch to batch depending on fabrication conditions. Therefore, the design is somewhat “passive” and lacks flexibility in adapting to various fabrication results.

Fig. 29 shows the normal strain in the *x* direction of the passive silicon membrane from a finite element analysis for a single-electrode design (cf. Fig. 10). The strain distribution consists of two regions. The first region is the central region covered by the top electrode. In this region, the silicon experiences positive strain, indicating that the diaphragm is extended. Since the deformation under the top electrode comes from the piezoelectric effect, this part of the diaphragm can be termed as the “active diaphragm.” The second region is outside the top electrode, and it experiences a uniform negative strain and hence contraction. For a single electrode design, the PZT thin film in this outside region not only fails to contribute any actuation, but also increases stiffness of the diaphragm reducing the actuator displacement. In a sense, the second region is a “passive diaphragm” for a single-electrode design.

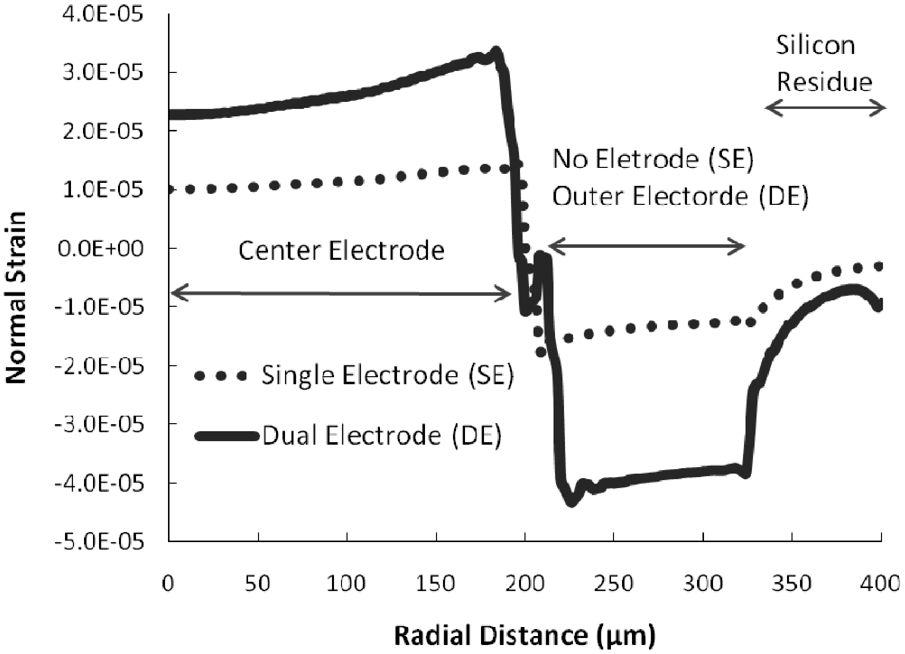

Fig. 29 Comparison of normal strain in the radial direction at the top surface of the passive silicon

Motivated by this observation, the purpose of this chapter is to develop a dual top-electrode design to significantly increase the actuator constant. In this design, the top electrode consists of two disconnected (thus independent) electrode areas, while a continuous bottom electrode serves as the ground. The basic idea is the following. As indicated in Fig. 29, the diaphragm deforms into two concentric areas whose curvatures are opposite. (For example, one is concave upward and the other is concave downward.) Therefore, a second electrode in the passive region will turn it into an active diaphragm as well. When it is driven in an out-of-phase manner to the center electrode, it will significantly enhance the actuator displacement.

This design has two advantages over the single top-electrode design. First, it fully utilizes the real estate of the actuator diaphragm to increase the actuator constant. Second, it can adapt to manufacturing defects (e.g., misalignment between the top electrode and the diaphragm) by adjusting the phase angle between the driving voltages of the two electrodes.

For the rest of this chapter, the enhancement of the actuator constant via a finite element analysis will first be demonstrated. Then, experiments will be conducted to show the feasibility of the dual top-electrode design. Two additional cases are presented to demonstrate the versatility of this design. One is misalignment between the top electrode and the silicon diaphragm. The other is the effect of the warping of the actuator diaphragm.

5.2 Finite element analysis

5.2.1 Model development

To study the displacement enhancement produced by the dual electrodes design, two finite element models are created using ANSYS. One is a reference model with a single top electrode, while the other has dual top electrodes for comparison.

The reference model is introduced in Chapter 4. The dual top-electrode model consisting of a center electrode and an outer electrode is shown in Fig. 27. The center electrode is identical to that of the reference model. The outer electrode has a width of

195 μm surrounding the center electrode like a rectangular frame. Between the two electrodes, there is a gap of 20 μm. The two electrodes can be driven independently by prescribing different voltages as electrical boundary conditions. The two top electrodes, however, share the same bottom electrode. Therefore, three electrical potential values will be assigned in the dual-electrode model.

Other features of the dual-electrode model are identical to that of the reference model. For example, the dual-electrode model has the same properties, element types, meshing, and linear static analysis.

5.2.2 Simulation results

Fig. 30 compares the displacements of actuators with single and dual top-electrode designs as a function of radial position, where the diameter of the silicon residue is 650 μm. For the single top-electrode design, the voltage of the top electrode is 1 V and the bottom electrode is grounded. For the dual top-electrode design, the voltage of the center and outer electrodes is 1 V and -1 V, respectively, while the bottom electrode is grounded. The maximal displacement of the single and dual top-electrode design occurring at the center is 0.41 μm and 0.54 μm, respectively. The presence of the second electrode increases the maximal actuator displacement by 32%.

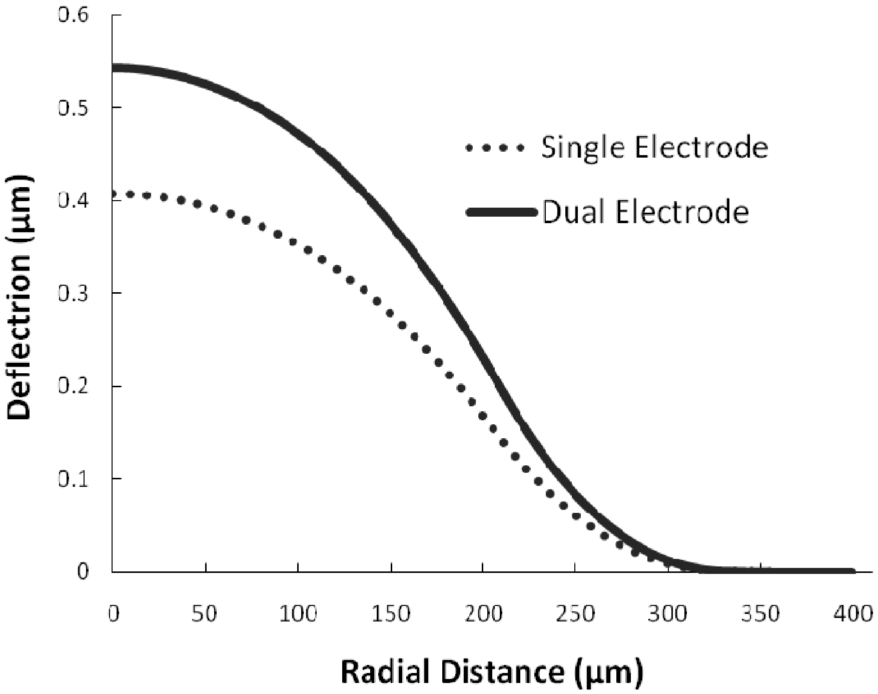

Fig. 30 Comparison of the displacement of the single and dual top-electrode design

Fig. 29 compares the normal strain σ_x from the dual- and single- electrode designs. The presence of the second top electrode significantly enhances the strain in the regions under both electrodes. As a result, actuator displacement is increased. Fig. 31 shows the normal strain distribution along the thickness (*z*-direction) of the diaphragm at the center of the actuator. The presence of the second electrode increases the strain throughout the entire thickness.

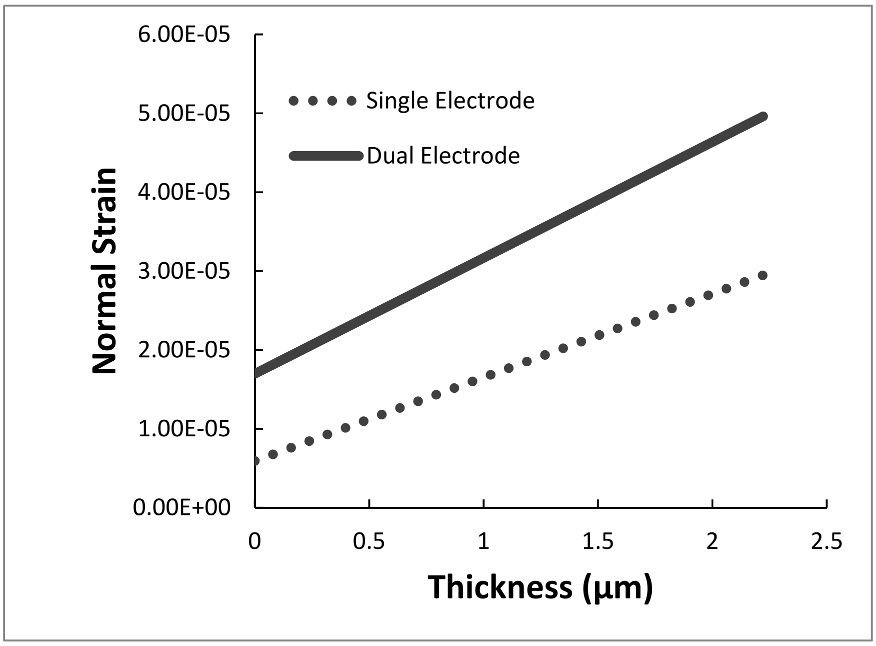

Fig. 31 Comparison of the normal strain along the thickness of the diaphragm

5.2.3 Optimization study

With the help of the finite element model, we can conduct simple parametric studies to optimize the geometry of the dual-electrode design to maximize the actuator constant. Fig. 32 shows how actuator displacement (at the center) varies with respect to the size ratio between the center electrode and backside cavity (the outer electrode has a fixed outer dimension of 800 μm and maintains a 20-μm gap with the center electrode). The maximal actuator displacement occurs around 50% (320 μm), whereas the residual silicon has a diameter of 650 μm. In other words, the best actuator performance occurs when the size of the center electrode is about half of that of the residual silicon.

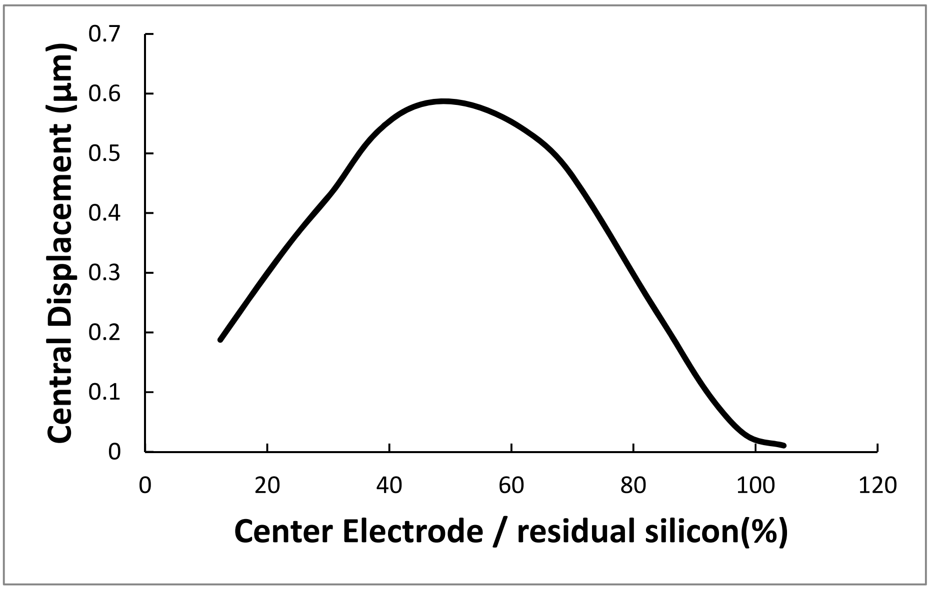

Fig. 32 Actuator displacement with respect to the seize of center electrode

Let us consider the case that the center electrode is optimized at 320 µm and the size of the residual silicon is 650 µm. Under these conditions, effects of the size of the outer electrode are studied via the finite element model. Fig. 33 shows how the displacement at the actuator center varies with respect to the size of the outer electrode. The variation consists of three portions. When the outer electrode exceeds the residual silicon (650 µm), the displacement saturates around 0.58 µm. As the outer electrode decreases in size, the displacement drops steadily and stabilizes at 0.4 µm. Results from Fig. 33 imply that the outer electrode must overlap with the residual silicon to deliver the maximal actuator displacement.

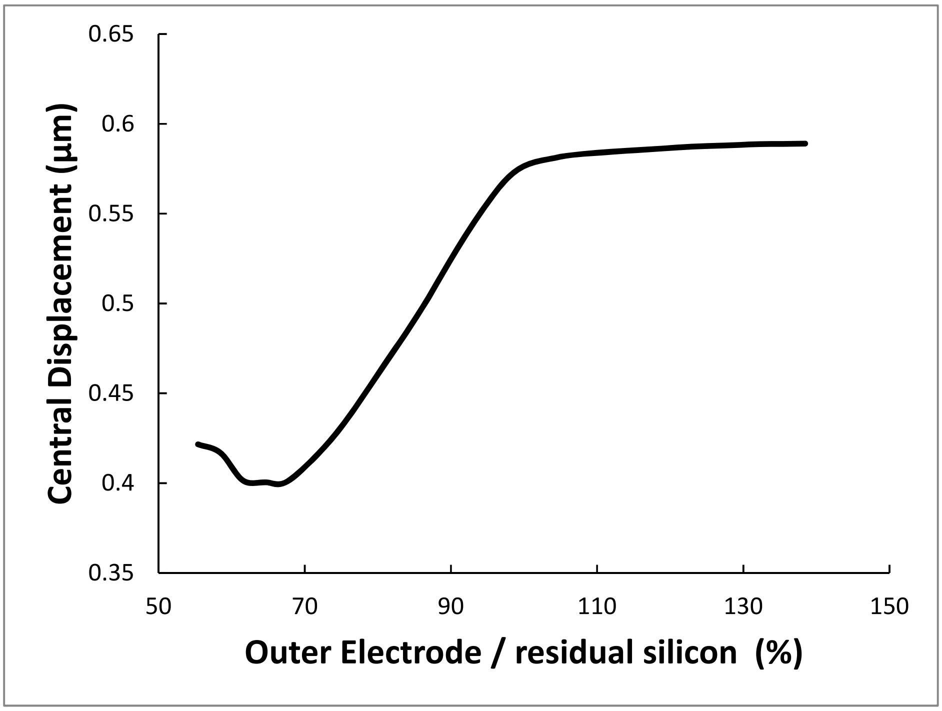

Fig. 33 Actuator displacement with respect to the size of the outer electrode

5.3 Experiment verification

Calibrated experiments are conducted to verify the simulation results. Specimen preparation, experimental setup, and measurement results are described in detail in the following sections.

5.3.1 Specimen preparation

Fig. 34 shows the top view of the fabricated actuator with dual top electrodes under an optical microscope. As one can see, the outer electrode does not completely enclose the center electrode because space is needed for a connecting wire to reach the center electrode from outside. For the actuator shown in Fig. 34, the center electrode is 390 μm×1390 μm, and the width of the connecting wire is 100 μm. In addition, the outer electrode is 800 μm×1800 μm; therefore, it is the same size as the diaphragm. The dashed circle refers to the boundary of the residual silicon, which is about 650 μm.

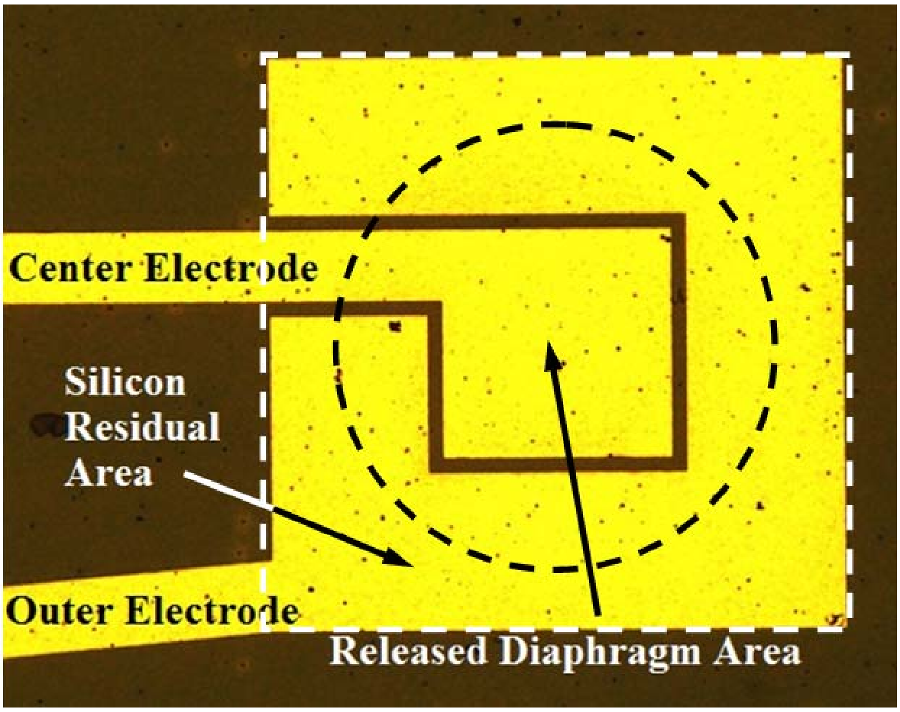

Fig. 34 Microscope picture of the actuator

5.3.2 Experimental Setup and Results

The experimental setup consists of two function generators, a laser Doppler vibrometer (LDV), an oscilloscope, and an actuator specimen to be tested, as shown in Fig. 35. The function generators drive the center and outer electrode, respectively. The excitations are sinusoidal with a frequency of 3 kHz. Moreover, the phase difference between the two driving voltages is adjustable. The LDV measures out-of-plane velocity of the actuator specimen. An oscilloscope monitors the two input driving signals and the output LDV velocity measurement. In particular, channels 1 and 2 of the oscilloscope represent the driving signal for the center electrode and the outer electrode, respectively. Channel 3 records the LDV velocity measurement.

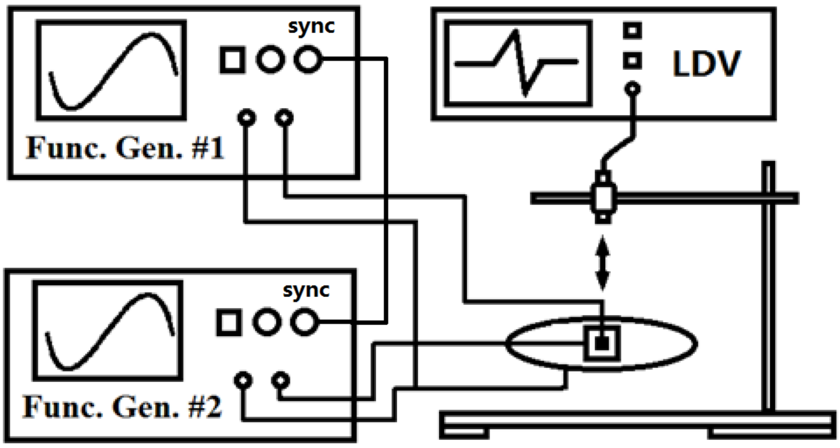

Fig. 35 Schematics of the experiment setup

The measurements of the actuator displacements under dual excitations with different phase differences are shown in Fig. 36 as a polar plot. The radial scale shows the measured actuator constant in nm/V, while the circumferential direction indicates the phase difference of the dual excitations in degrees. The actuator displacement reaches its maximum of 17 nm/V when the phase difference is 180°. When the two electrodes are driven in the same phase, the actuator has a minimal displacement of 5 nm/V. A phase difference of 90° generates a median displacement of about 12 nm/V. These results are consistent with those predicted from the finite element analysis.

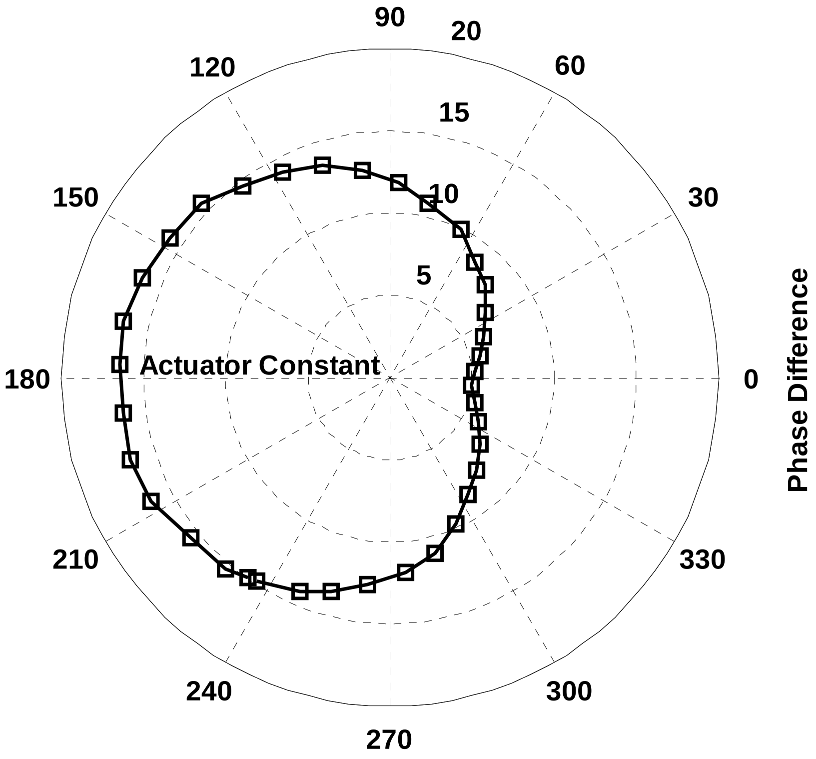

Fig. 36 Displacements under excitation with different phase differences

5.3.3 Applications to Misaligned Microactuators

As mentioned above, fabrication defects could significantly decrease performance of the actuator in terms of actuator displacement. One type of defect is the misalignment of the top electrode and the diaphragm (and therefore, the cavity released via DRIE underneath the diaphragm), as shown in Fig. 37. Such a misalignment could decrease the performance of the actuator for two reasons. First, the effective area of the electrode is smaller because part of the top electrode may not be on the released diaphragm. Second, the position of the top electrode is away from the optimized position (i.e., center of the diaphragm).

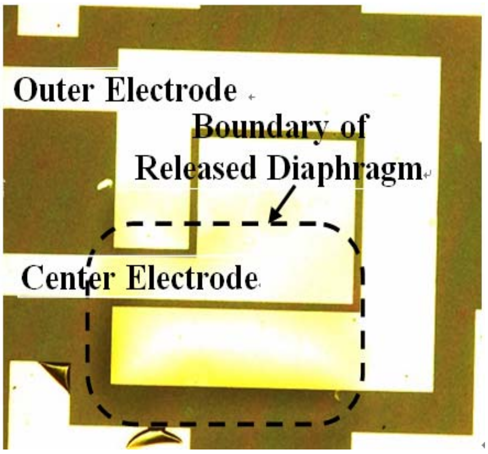

Fig. 37 Microscope picture of the misaligned actuator

The same experimental setup was applied to the misaligned actuator, shown in Fig. 37. The driving signals to the center and outer electrodes have the same magnitude, but the phase difference is adjustable. Fig. 38 shows the measured out-of-plane velocity of the actuator in the form of a polar plot. The radial readings are the actuator constant (i.e., displacement per volt in nm/V) and the circumferential readings refer to the phase difference (in degrees). When the phase difference is 14.8°, the actuator has the smallest displacement of 16 nm/V. In contrast, when the phase difference is -172.2°, the actuator has the largest displacement of 29 nm/V.

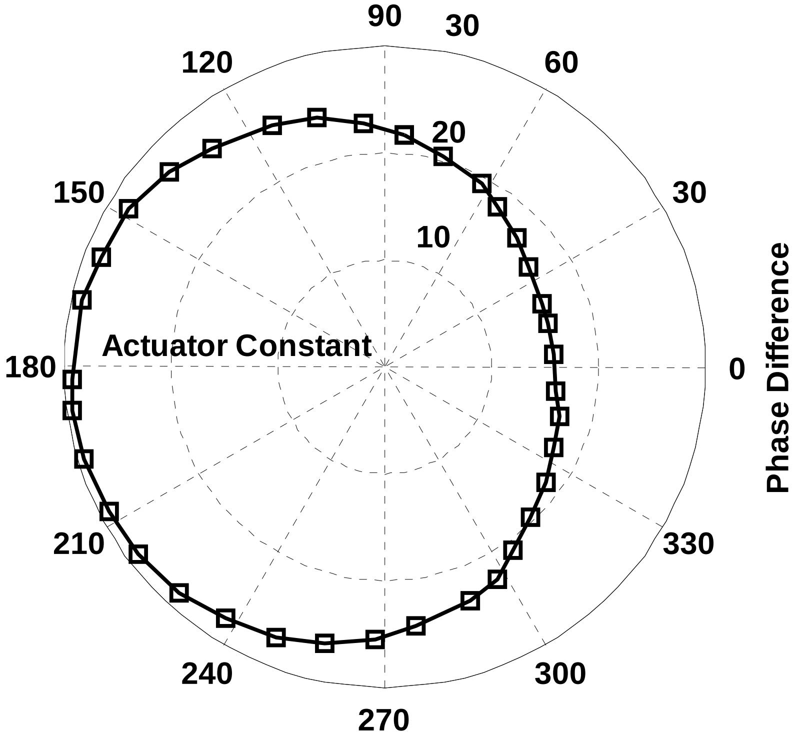

Fig. 38 Displacements under excitation with different phase difference (misaligned actuator)

There are two things worth noting. First, the outer electrode now occupies as large an area of the released diaphragm as the center electrode due to misalignment. Therefore, activation of the outer electrode can now significantly improve the performance of the actuator. Second, the dual-electrode setup allows flexible adjustment of the phase angle to maximize the actuator displacement. As a result of the misalignment, the maximal displacement does not occur at 180° anymore. Since manufacturing defects are unavoidable, the use of dual top electrodes can serve as an effective way to enhance the yield of the manufactured actuators.

5.3.4 Effects of Warping

The finite element analyses above assume that the actuator always has a flat diaphragm. In reality, the diaphragm may warp due to residual stresses resulting from the sintering process of the PZT thin film at elevated temperatures. For example, Fig. 39 shows the surface profile measured through an optical profiler NT3300 indicating a bulge of 3.89 μm with the released diaphragm. Naturally, the finite element predictions above may break down when the warping becomes significant.

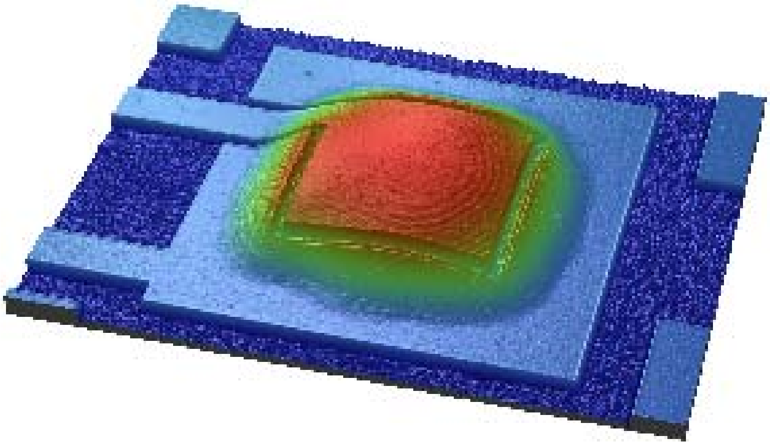

Fig. 39 3D Profile picture of the warped actuator

We have also conducted experiments on warped actuators. The maximum displacement, however, occurs when the center and the outer electrodes are driven in the same phase. As shown in Fig. 40, the two driving voltages (channels 1 and 2) are almost in phase and the resulting actuator velocity measurement (in channel 3) is about 18 mV peak-to-peak. In Fig. 41, the two driving voltages (channels 1 and 2) are almost out of phase and the resulting velocity measurement is about 8 mV peak-to-peak. This is about a

55% reduction from the response under in-phase excitation. The measurement results over 360º shift are shown as a polar plot in Fig. 42.

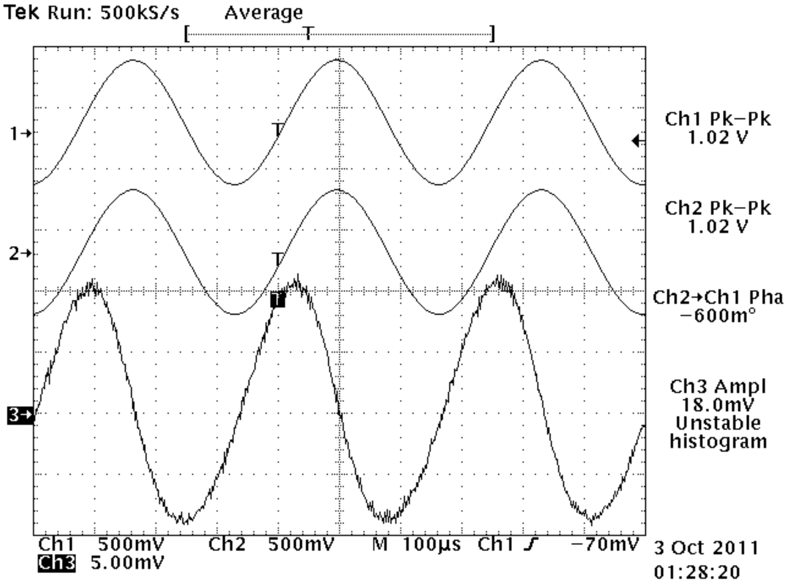

Fig. 40 Actuator excited by both electrodes (in phase)

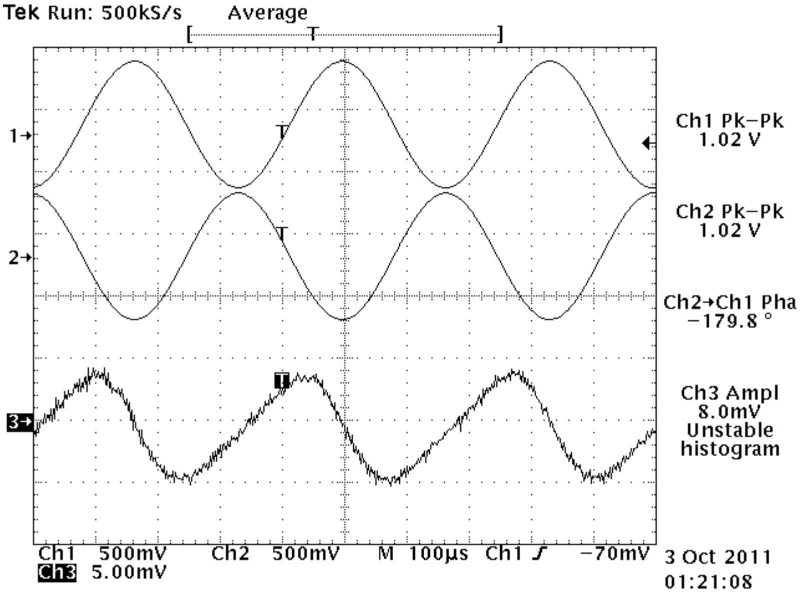

Fig. 41 Actuator excited by both electrodes (out of phase)

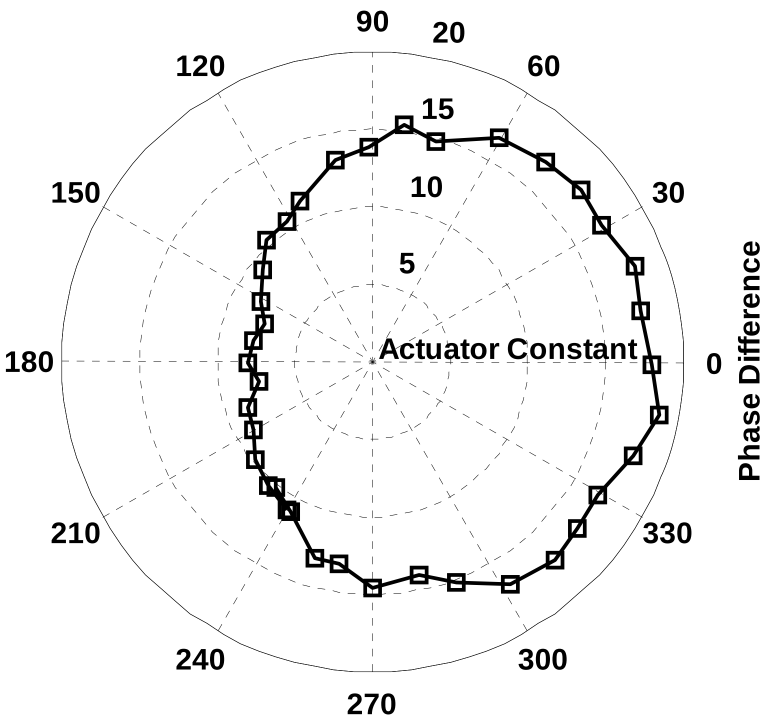

Fig. 42 Displacements under excitation with different phase difference (warped actuator)

These experimental results, at first glance, may seem to contradict the finite element predictions. However, one needs to realize that there are two components contributing to the out-of-plane displacement of the actuator diaphragm. The first component results from the bending of the diaphragm. When the PZT thin film extends or contracts, it generates a bending moment flexing the diaphragm resulting in an out-of-plane displacement. This effect is always present whether or not the actuator diaphragm is warped. Also, the center and outer electrodes must be out of phase in order to maximize this out-of-phase component.

In contrast, the second component results from in-plane deformation of the diaphragm. When in-plane deformation occurs, the corresponding in-plane motion takes place along the mid-surface of the diaphragm. When the actuator diaphragm is perfectly flat, the mid-surface is flat. Since the boundary conditions are fixed at four edges, the in-plane motion along the mid-surface cannot change the length of the diaphragm. As a result, the in-plane motion is confined to the flat actuator plane leading to no out-of-plane motion.

When the actuator diaphragm is warped, the mid-surface is no longer flat. The in-plane motion along the mid-surface can change the length of the diaphragm and the curvature of the mid-surface (e.g., via bulging or flattening). When this happens, an out-of-plane displacement component occurs simultaneously in order to maintain the fixed boundary conditions at the edges. To maximize this out-of-plane component, the center and outer electrodes should be in the same phase, so that they extend or contract together to increase the change of the diaphragm length.

The competition of these two out-of-plane components will depend on many factors, such as degree of warping, severity of residual stresses, physical dimensions of the remaining silicon, and the thickness of the layers in the actuator diaphragm.

5.4 Summary

In this chapter, we have demonstrated an effective design to enhance displacement of a PZT thin-film actuator by employing dual top electrodes. The dual-electrode design consists of a center electrode and an outer electrode driven independently. By adjusting the phase angle between the two driving electrodes, one can maximize the actuator displacement. Furthermore, the dual-electrode design can effectively accommodate imperfections from manufacturing, such as misalignment and warping, to meet specifications in displacement, and thus, increase the yield.

Chapter 6 Design and fabrication of probe device

Up until this point, most PZT thin film micro-actuators and microphones have been fabricated and tested in wafers. In order to demonstrate the function of the intra-cochlear piezoelectric acoustic actuators and microphones in acute animal tests, we need to make an actuator-microphone probe device that is able to be surgically implanted into the cochlea of guinea pigs. The design of this probe device is introduced in this chapter.

6.1 Introduction

A conceptual probe device is shown in Fig. 6. The PZT thin-film with dual top electrodes is at the tip of the probe. One top electrode serves as an acoustic actuator and the other serves as a microphone. When voltage is applied, the piezoelectric diaphragm deforms to generate acoustic stimuli serving as an actuator. When sound pressure waves are present, the piezoelectric diaphragm deforms to generate electric charge serving as a microphone. The width of the tip is about 1 mm in order to fit the size of a guinea pigs' cochlea. One side of the PZT thin film is anchored on solid silicon, while the other three sides are anchored on thin wall structures with a thickness of about 100 micron.

6.2 Dicing method and layout design

The fabrication process of the PZT thin film sensor and actuators is introduced in Chapter 2. For probe devices, most fabrication processes will be the same for the sake of avoiding the risk of changing the recipe. However, the sensors and actuators need to be separated into single probes after being fabricated on a wafer. The dicing strategy and the layout design is discussed in the following sections.

6.2.1 Dicing method

There are two options that are able to accomplish the dicing mission. The dicing saw is introduced in Section 2.5. A prerequisite of this method is the ability to leave marks on the top electrode layer for the cutting alignment. Therefore, the lithography mask for the patterning of the top electrodes must be redesigned.

Another option for accomplishing this mission is to separate the probes from each other by using the last step of the DRIE process. While the backside cavities are etched, the slots between the probes are etched simultaneously. The remaining connections between the probes are in the thickness of microns and are easy to be break by hand. However, the broken edges are not as clean as one cut by the dicing saw. A necessity for this operation is to redesign the lithography mask for DRIE patterning.

The most attractive advantage of the dicing saw is that cutting edges will be clean. There will not be any residual material remaining around the probe. Another advantage is that the modification of the mask is relative easy. The only modification is adding cutting marks around the diaphragm structures with the desired distance. However, there are also many drawbacks of this operation. First, the blade needs to be aligned with cutting marks for every cut. This will not only tremendously increase the processing time, but also cause a variation of the thickness of the walls around the PZT diaphragm. Second, the yield of fabrication will become lower given an increasing risk of breaking the PZT diaphragm. Because the PZT diaphragm structures will have been released before the cutting operation, the intensive mechanical vibration caused by the sawing process may damage the diaphragm. The third disadvantage is the dirty environment full of tiny silicon powders generated from the sawing process. Although a layer of photoresist can protect the probes from contamination, the coating and cleaning process of the protection layer will increase both the risk of breaking PZT diaphragm and the processing time.

On the other hand, separating probes by DRIE has several advantages over the dicing saw. DRIE processes do not have the disadvantages mentioned in the above paragraph. It can be combined with the last etching process. All separating slots between probes are formed simultaneously together with backside cavities, so no more extra backend processes are required; the etching process will not involve mechanical vibration or physical contamination; the thickness of the walls around the diaphragm is precisely defined by the patterning mask. The disadvantage of DRIE is rough edges of the probes caused by handwork breaking. Sometimes, there will be PZT layers remaining outside the walls around the diaphragm.

6.2.2 Layout design

There are two types of layout design: square array and radial array, as shown in Fig. 43 and Fig. 44. Both layout designs can only have one row around the PZT thin film area, so that each device can have an area of exposed bottom electrode. In the square array layout, probes will be rectangular; the width of the probe is constrained to about 1 mm due to the size of the cochlea. While in the radial array layout, probes will be trapezoid in shape. As the tip width is 1 mm, the width of the probe tail will have some degree of flexibility for adjustments.

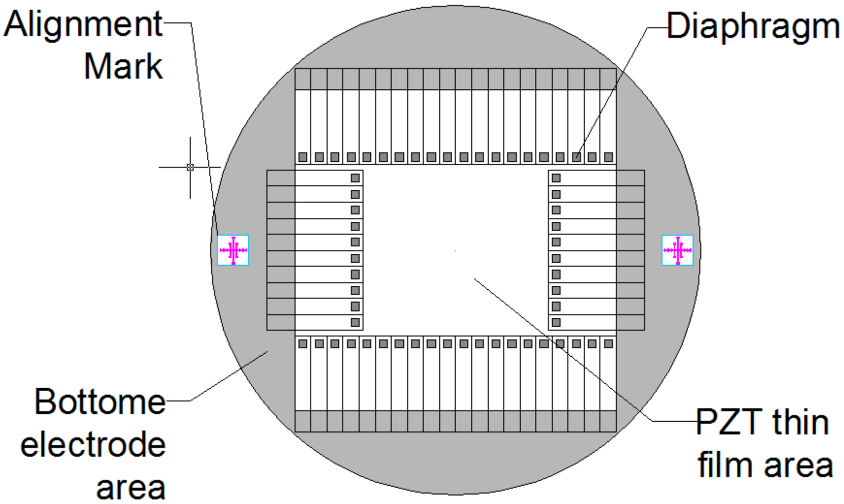

Fig. 43 A schematic of square array layout design

For rectangular probes, it is easier for simulation modeling or theoretical calculations. Another preference is higher efficiency in separating probes. By using the auto index function of the dicing saw, a lot of cutting alignment work could be saved.

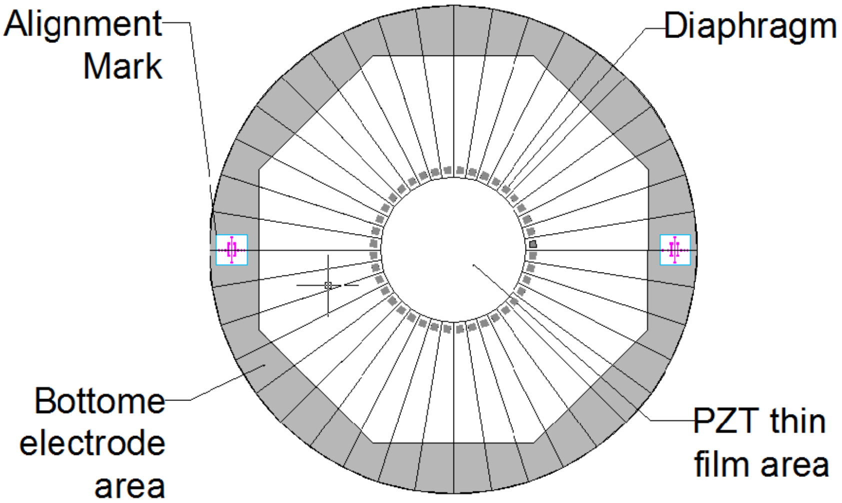

Fig. 44 A schematic of radial array layout design

For the radial array layout, the diaphragms are located on a circle. The distances from the center of the wafer are about the same. This will provide a better thickness uniformity of PZT thin film because the PZT is spin coated with the sol-gel method. In addition, a wider probe tail will offer some advantages over rectangular probes from a practical operation aspect. First, the soldering pads for the two top electrodes can be further from each other. This will prevent them from shorting during the soldering process. Second, larger soldering pads and wider probe tail will make the wire connection and the whole probe more robust to sustain all kinds of mechanical load during experiments.

Because fabrication yields and the sustainability of each probe are the two most important concerns, DRIE was chosen as the dicing method, and the radial array layout was chosen as well.

6.3 Mask design

After the dicing method and layout are determined, the mask design for the probe devices is introduced in this part. The backside mask defines the pattern of the etching process; therefore, it defines the geometry of the cavities under diaphragm structures and also the outline of the probes. The top-side mask defines the center and outer electrodes, soldering pads, and connection wires between them.

6.3.1 Top-side mask design

As shown in Fig. 45, the top electrodes mask is composed of three parts: effective electrodes, connection wires, and soldering pads. The effective electrodes include center electrode and outer electrode. Based on the FEA optimization study introduced in Chapter 5, the outer electrode is designed to be 800 μm×1800 μm, covering the whole span of the diaphragm structure, while the center electrode is 320 μm×1320 μm, about half of the opening size of silicon residue, in order to have the maximum central displacement. In addition, there is an opening in the outer electrode to accommodate the connecting wire from the outside to center electrode. The gap between outer and center electrodes has a width of 20 µm.

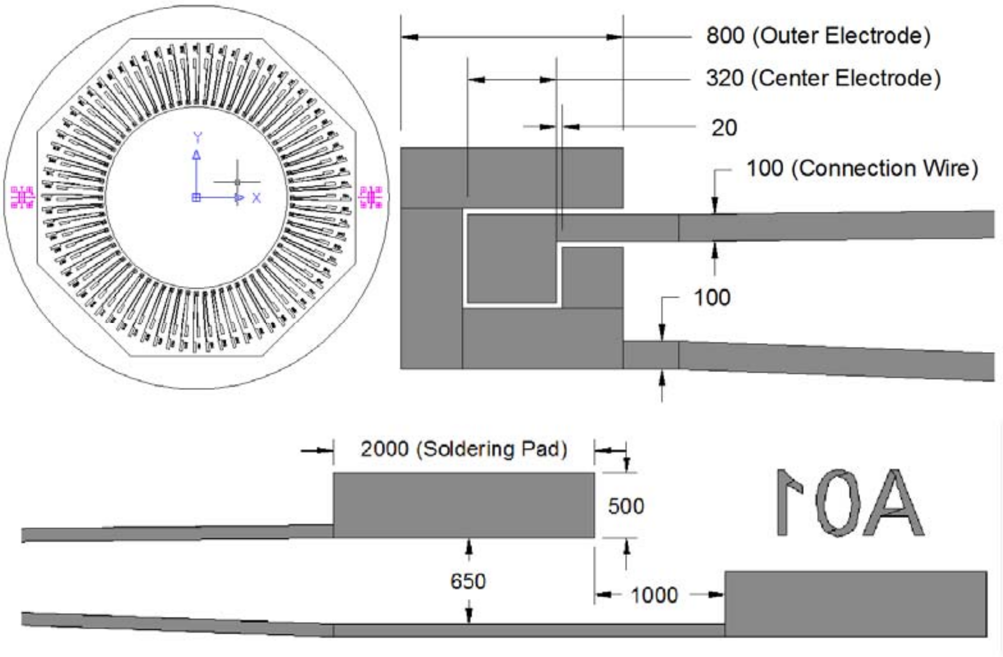

Fig. 45 Top-side mask design

6.3.2 Back-side mask design

As shown in Fig. 46, the backside mask consists of two alignment marks on each side of the wafer, a circle and many radial lines to define the probe outlines, and a circular array of squares to define the backside cavities of each diaphragm. Within one mask, there are three types of probes with different wall thicknesses, at 100 µm, 150 µm, and 200 µm.

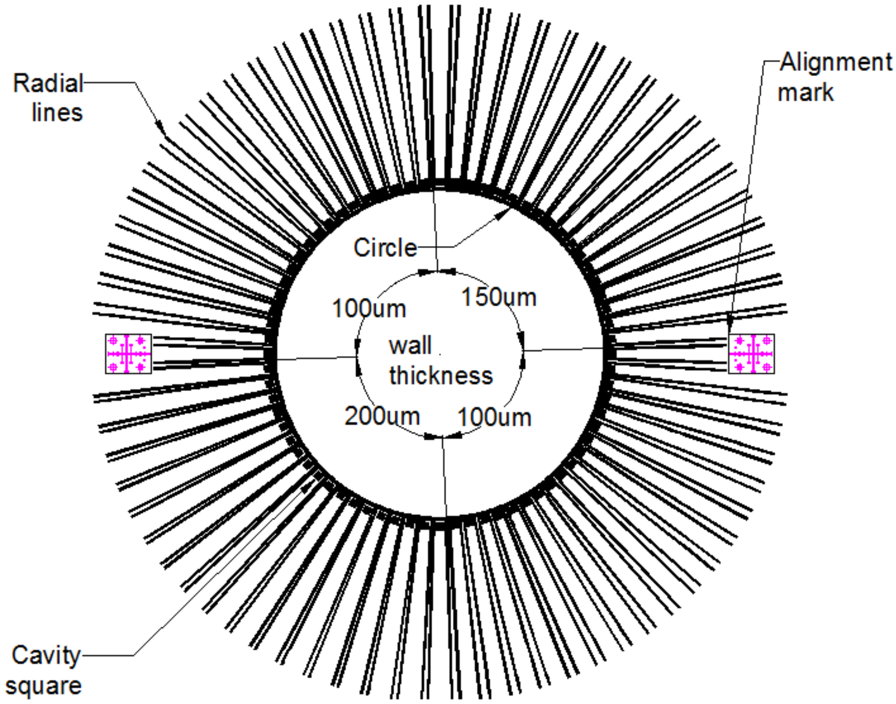

Fig. 46 Backside DRIE mask

The outline of a probe with 100 μm wall thickness is shown in Fig. 47. It is defined in the following steps. The angle taken by each probe is 5 degrees. The radius of the circle is 18.5 mm. The edges of the probe tips are tangential to the circle with a width of two times the wall thickness plus the cavity size. The distance between the square cavity (800 μm×1800 μm) and the edge of the probe tip is the desired wall thickness. The two radial lines beside each probe are defined by extending the two lines connecting the wafer center and the two corners of the probe head.

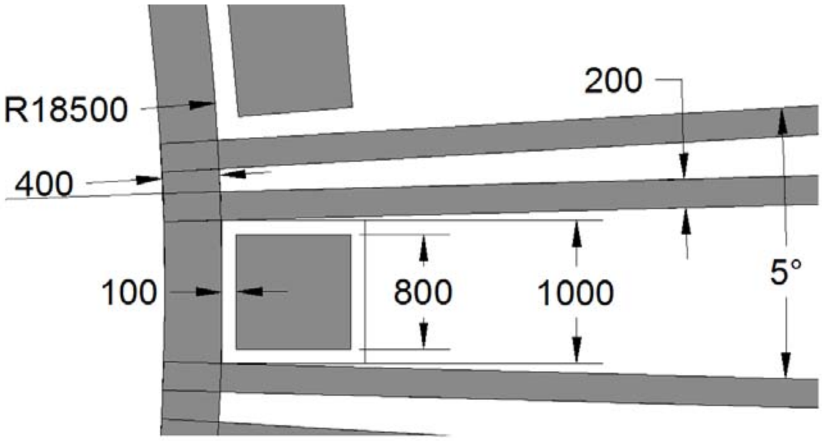

Fig. 47 Backside DRIE mask zoom in (μm)

The width of each etching line depends on a trade-off between two factors. When the line is thinner, the stress concentration when breaking probes will be larger, which is desired for neat breaking edges. When the line is wider, the remaining structure will be thinner. This is desired for less breaking force.

In the first trial, the radial lines and circle are set to 10 μm and 200 μm in width. Because the radial lines are too thin when compared to the size of the cavities, as shown in Fig. 48, the etching rate of the radial lines are not enough to remove all silicon materials when the insulating SiO_2 layer is exposed in the square cavities. Therefore, when breaking the probes, the wafer is broken horizontally or vertically along the direction of the silicon crystalline, rather than the designed radial lines.

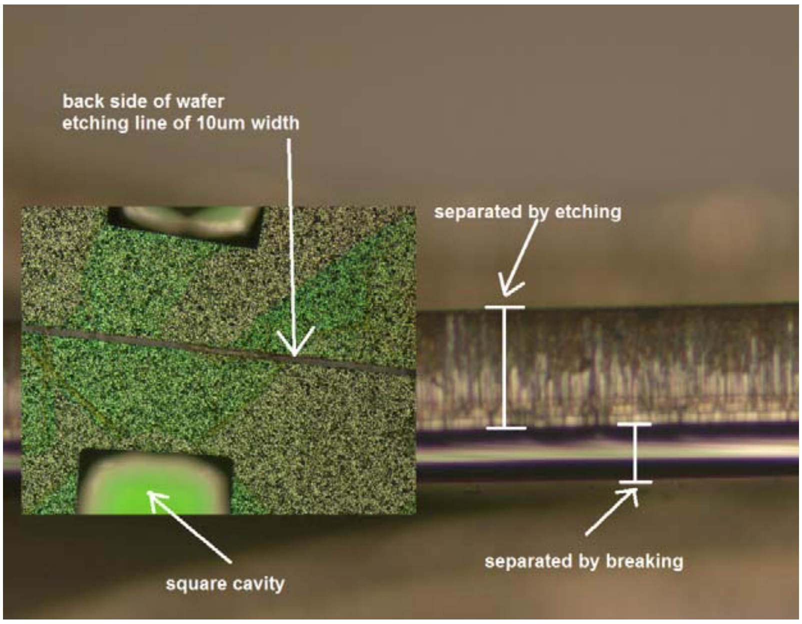

Fig. 48 Separating effect of the etching lines of 10 μm in width

For the second trial, the radial lines and circle are set to 200 μm and 400 μm. The probes are easily separated from each other by hand, as shown in Fig. 49.

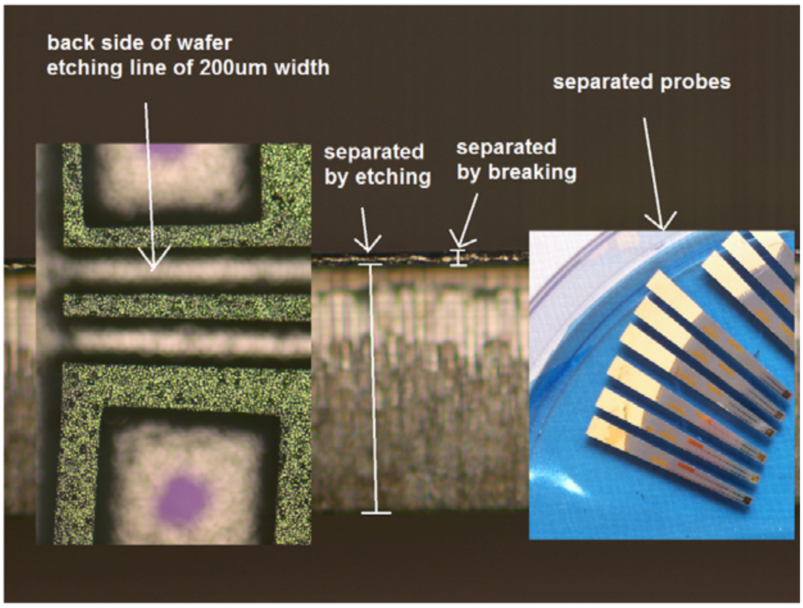

Fig. 49 Separating effect of the etching lines of 200 μm in width

Chapter 7 Boundary conditions for probes

After fabrication, different boundary conditions need to be explored to figure out a consistent setup for further experiments on probes. The effect of the different boundary conditions on the measurement of the actuator performance is shown in Section 3.2.1.

Before the probe device is fabricated, most PZT thin-film devices are tested in the wafer. Because the wafer is much stiffer than the PZT diaphragm, the displacement of the surrounding silicon is negligible and the diaphragm is clamped at four sides. The FEA result of displacement in the z direction, as shown in Fig. 50, also agrees with this conclusion. A typical frequency response (displacement to excitation) measured under the clamped boundary condition is shown in Fig. 51 as a reference for the measurement of the probe device. Normally, there is a resonance peak around 100 kHz while the lower frequency range is a flat zone.

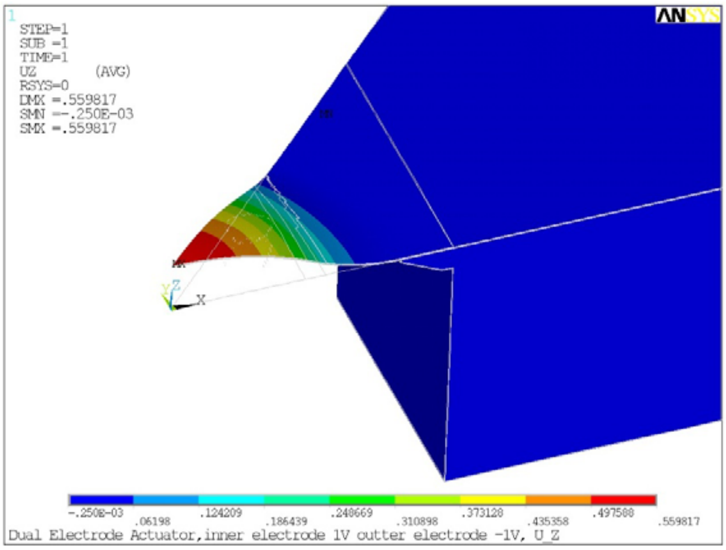

Fig. 50 FEA result of the probe strain

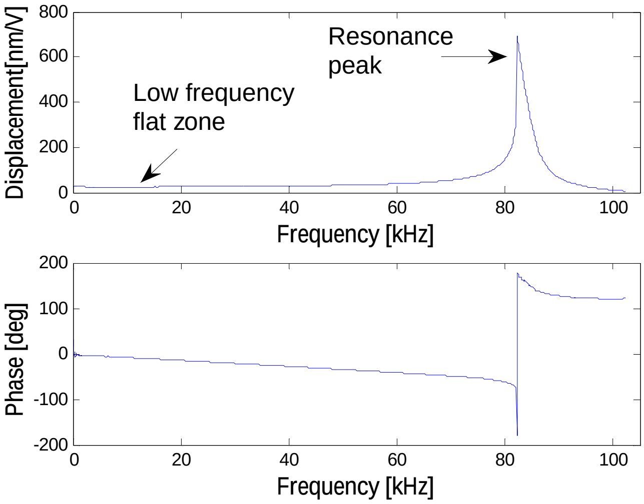

Fig. 51 Typical frequency response under the clamped boundary condition

7.1 Simply supported boundary condition

A probe device is first tested under the simple supported boundary condition, as shown in Fig. 52. The probe is supported by a layer of non-residual blue tape on an aluminum block.

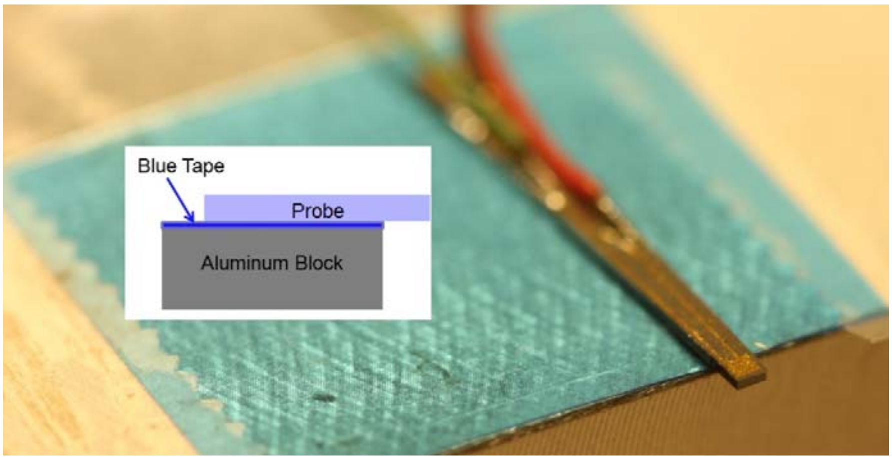

Fig. 52 Simple supported boundary condition with blue tape

The measurement result is shown in Fig. 53. When comparing this result to the one from the clamped boundary condition, there are two major differences. First, the big diaphragm resonance peak is higher than 100 kHz. This may be caused by many random reasons. For example, larger thermal stress was induced during the PZT sintering process, the opening of the silicon residue is smaller, or the diaphragm structure is thicker. All of these reasons will lead to a stiffer diaphragm with a higher resonant frequency. Different resonance frequencies were also seen from different devices within the same wafer. Since we care more about the effect of the boundary conditions on the displacement in lower frequency ranges of around 3 kHz, this difference is ignored. Another important difference is that there are four resonance peaks, at 7.2 kHz, 20.9 kHz, 44.2 kHz, and 70.5 kHz, respectively.

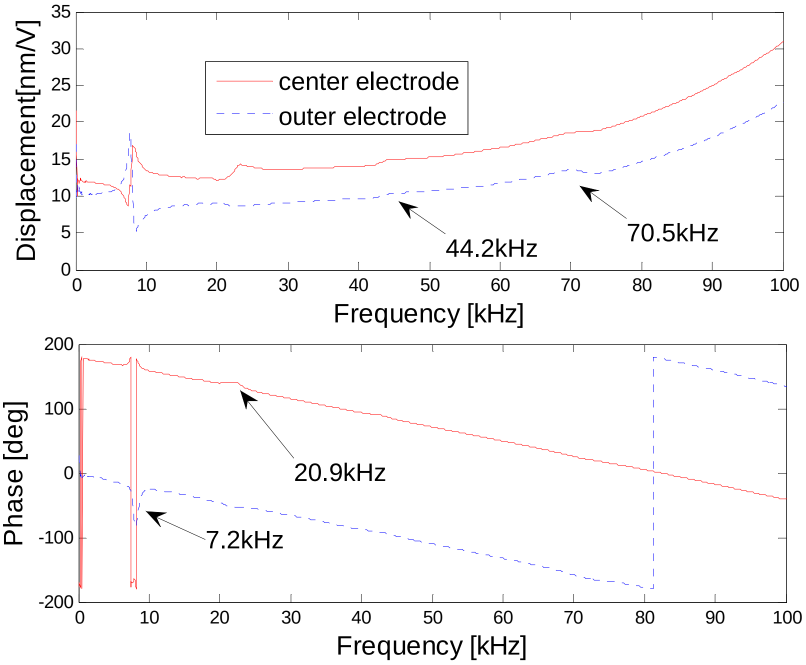

Fig. 53 Measurement results of the simple supported boundary condition

7.2 Experiment under clamped-free boundary conditions

In order to have a flat zone in the low frequency range of around 3 kHz, the resonance peaks need to be recognized and eliminated. Since these peaks did not show up in the results of the clamped boundary condition, the reason for these peaks should be related to the probe shape or the three thin wall structures. Because the amplitude of the 4 peaks are decreasing while the frequency difference between each two are increasing gradually, a simple guess for the unknown vibration is that the probe vibrates in the form of a cantilever beam.

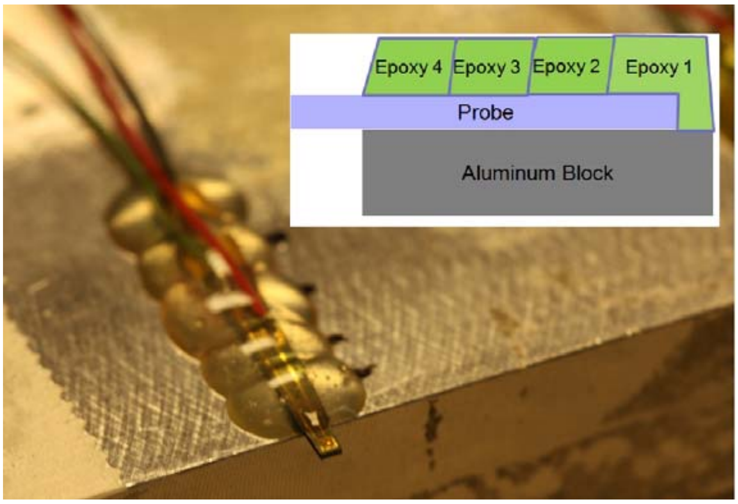

Fig. 54 Clamped-free boundary conditions of different fixed lengths with epoxy

A series of experiments are completed to verify this supposition. The boundary conditions of the experiments are shown in Fig. 54. The probe is fixed on top of an aluminum block with epoxy. The frequency response of the same probe is sequentially measured with 4 different unfixed probe lengths. According to previous assumptions, as the unfixed part becomes shorter, the resonance frequency should get higher. The experiment results agree with this trend, as shown in Fig. 55.

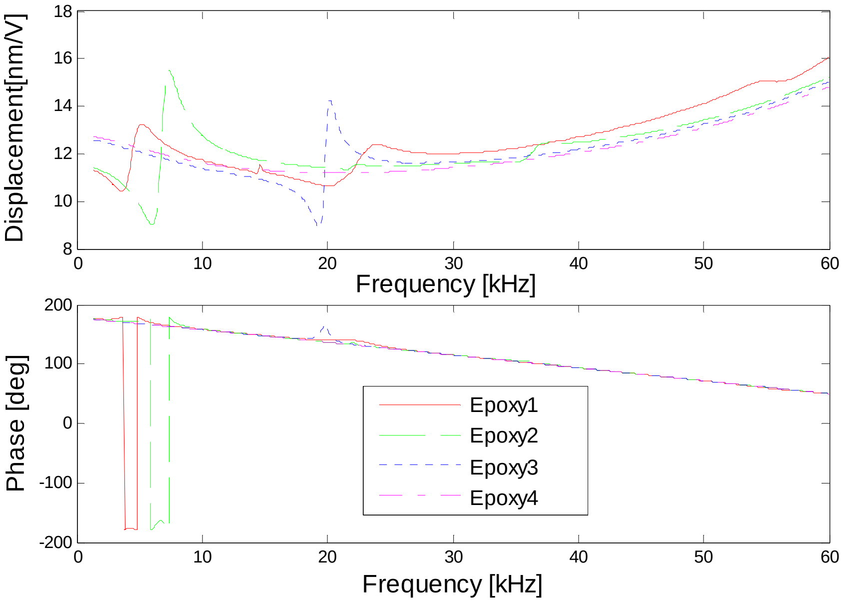

Fig. 55 Experiment results of the clamped-free boundary conditions

7.3 Calculation of the clamped-free boundary condition

Further calculations are made to be compared with the experiment results. The natural frequency of the rectangular single beam can be calculated with the following formula:

$$f_i = \frac{{\lambda_i}^2}{2\pi L^2}\left(\frac{EI}{m}\right)^{\frac{1}{2}}; i = 1,2,3 \ldots$$

$$I = \frac{bh^3}{12}$$

Where λ_i is a dimensionless parameter which is a function of the boundary conditions applied to the beam, L is the length of the beam, E is the young's modulus of the material, I is the moment of inertia of the beam, b is the width of the beam, h is the thickness of the beam, and m is the mass per unit length.

For our trapezoid probe, several upper and lower limits of these parameters, shown in Fig. 56, are used to calculate a range of resonance frequencies. The limits of the length are the probe length with and without the cavity part. The limits of the moment of inertia are calculated from the width of the probe tip and tail. The limits of the mass per unit length are the mass in gray color distributed in the limits of the length. The young's modulus of the silicon is used since the whole diaphragm structure is two magnitude of order thinner than the wafer.

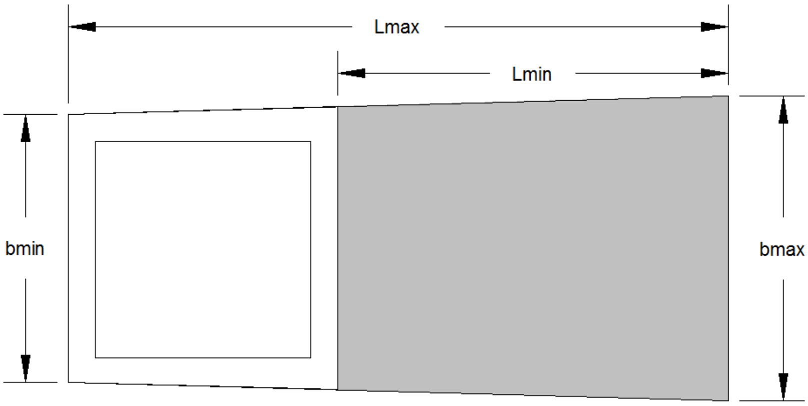

Fig. 56 Schematics of geometry limits

7.4 Summary

The results from the calculations and experiment are compared in Table 2. All of the measured resonance frequencies are located between the upper and lower limits from the calculations. This demonstrates the resonance peaks are different modes of the probe vibration as a cantilever beam. Based on the lower limit calculation, the exposed length should be less than 3 mm to have the first resonance frequency higher than 60 kHz.

Table 2 Calculation and experiment results of the resonance frequencies

probe length	f_{1max}	f_{1min}	Exp.	f_{2max}	f_{2min}	Exp.	f_{3max}	f_{3min}	Exp.
12.2 mm	5.56	3.11	4.30	34.81	19.51	22.00	97.48	54.62	55.60
10.5 mm	7.60	4.32	6.70	47.62	27.06	36.50	133.34	75.76	NA
5.9 mm	26.25	14.58	19.80	164.48	91.36	NA	460.55	255.81	NA
2.0 mm	520	140.14	NA	3260	878	NA	9129	2459	NA

Because the probe is brittle and small, and the diaphragm and soldering connection will be at the tip and tail, the handling of the probe in the following experiments is not convenient, even with tweezers. A holder is designed and fabricated. After the soldering connection is done, the probe can be fixed in the holder with silicone. The exposed length is about 3 mm and the soldering connection will be protected. The design file is included in the Appendix C.

Chapter 8 Parylene coated probe working in fluid environment

As introduced in Chapter 1, the ultimate goal for the probe devices is to make a hybrid cochlea implantable hearing aid. In addition to the geometry requirement of the application, which is discussed and satisfied in Chapter 6, an important issue is the fluid environment in the cochlea. One crucial challenge that the fluid environment presents is the possibility of shorted electrodes of the device due to contact with this fluid. In this chapter, a parylene coating is discussed as the solution to this problem.

8.1 Coating process of parylene

8.1.1 Parylene introduction

Parylene is the generic name for p-xylylene polymers. Due to the combination of their excellent moisture and dielectric barrier properties, good chemical and thermal stability, and clarity for visible lights, parylene is widely used as the protective coating for all kinds of devices, such as electronics for space travel or military use, metallic parts working in highly corrosive environments, and optical lenses or mirrors that need protection from abrasion. Especially, because of their bio-compatibility, parylene are also used in defibrillators, pacemakers, and many other permanently implanted medical devices. Despite these numerous benefits, most parylene materials have relatively low

UV stability. Therefore, parylene is not recommended to be used outdoors directly. Even though all of our experiments are completed in lab, the coated probes are protected from direct sunlight and UV sources.

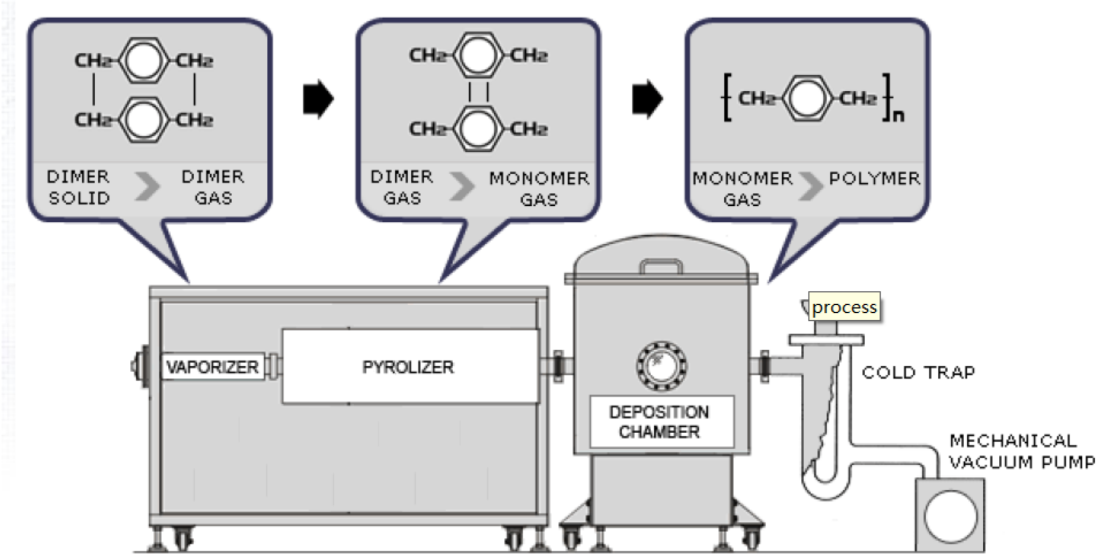

Fig. 57 Parylene coating process [**Error! Reference source not found.**]

The parylene coating is a green process because no initiator or termination group is needed, and no solvent or catalyst is required. As shown in Fig. 57, it starts from paracyclophane (dimer), which is first vaporized into gas. Because of the reduced pressure at the other end, the gas molecules will move into the pyrolysis zone, in which the gas is pyrolized into para-xlylyene, the reactive monomer under high temperature. The monomer molecules then enter the deposition chamber, where they are physisorbed and polymerized on all exposed surfaces to form the coating thin film at room temperature.

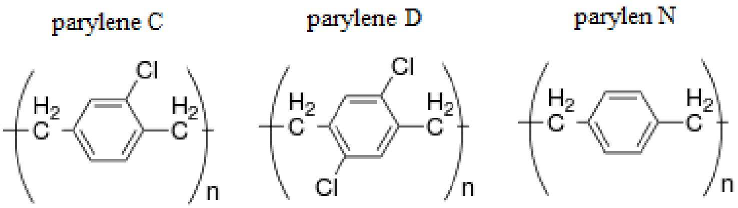

Fig. 58 Repeating units of three types of parylene

Among all parylene materials, Parylene C, Parylene D, and Parylen N are the most popular forms. They are chemically different in repeating units, as shown in Fig. 58. The chlorine atom on the benzene ring in Parylene C results in lower permeability to moisture, chemicals, and other corrosive gases than parylene D and N. Parylene D, with two chlorine atoms, is better at maintaining its physical strength and electrical properties at higher temperatures. Parylene N is a non-substituted molecule having the highest dielectric strength among the three versions. In addition, less molecule mass result in a higher level of molecular activity during deposition, which makes the coating layer more conformal than the other two types.

In our fabrication, parylene N is selected. Except for the benefits just mentioned, its lower young's modulus will diminish the actuator constant less by causing smaller increases in diaphragm stiffness. Some important properties are listed in Table 3.

Table 3 Properties of parylene materials

Parylene type	Density g/cm^3	Young's modulus GPa	Poisson Ratio	Yield strength MPa	Melting Point ^{o}C	Dielectric constant 1kHz	Dielectric Strength V/mil

C	1.31	3.2	0.4	65.6	290	2.83	6900
N	1.11	2.4	0.4	50	420	2.65	7000

8.1.2 Effect of parylene coating thickness on displacement

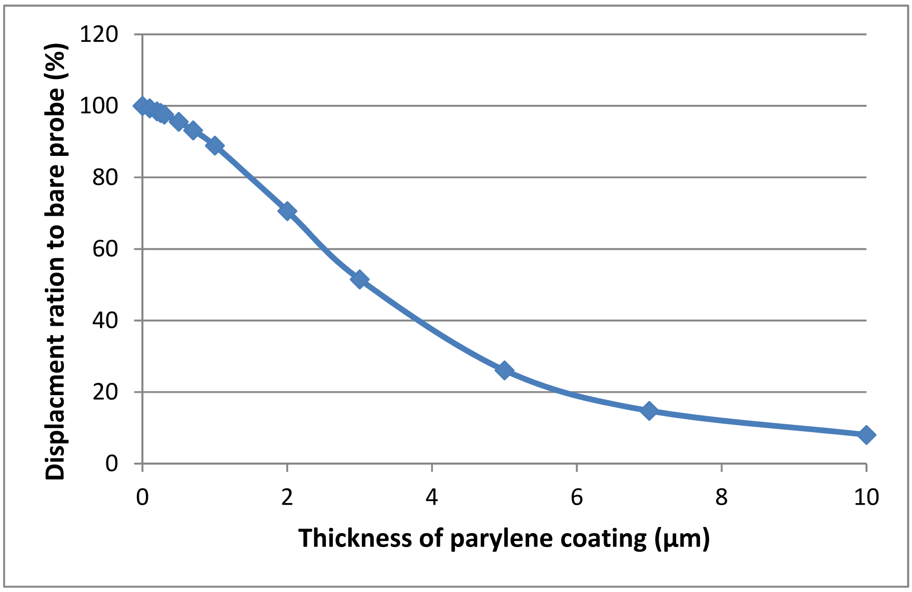

Fig. 59 Displacement ratio in respect to the coating thickness

To make a decision for the appropriate coating thickness, two finite element models are developed in Ansys to analyze the effect of the parylene coating on the performance of the actuators. The thickness of the coating layer of one model is adjusted to be compared with the other model without the coating layer. Other modeling parameters of these two models are the same. The analysis results from these two models are shown in Fig. 59. When the coating is thicker, the diaphragm is stiffer and the placement is smaller. The coating thickness is designed to be 1 μm. The displacement will decrease to about 90% according to the simulation results.

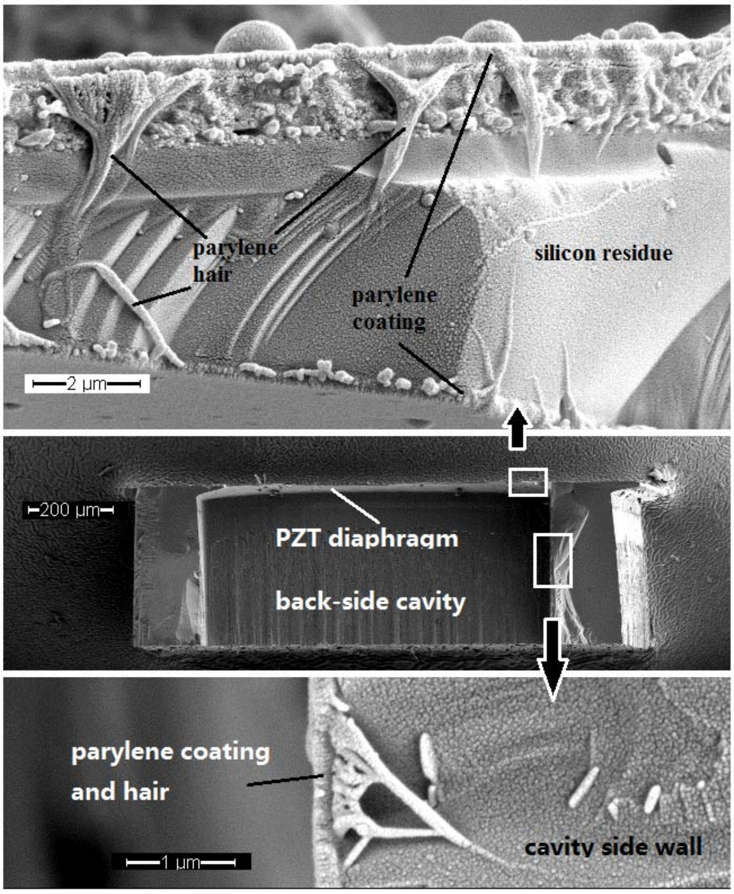

Fig. 60 Parylene coating on different surfaces

After the probes are coated, some cross sectional SEM pictures of the probe tip are taken, as shown in Fig. 60. The parylene coating is conformal on all exposed surfaces, including the top surface, bottom surface, and side wall surface. The parylene hairs should be generated when the probe was broken due to its high elongation capabilities. The thickness of the parylene coating is about 250 to 260 nm, as shown in Fig. 61.

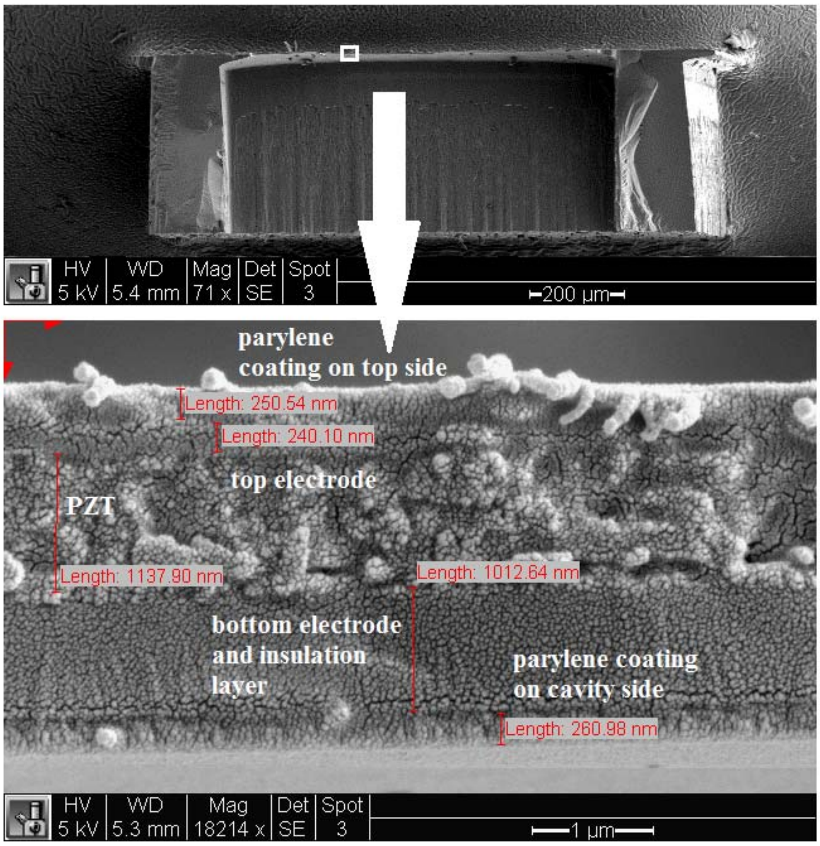

Fig. 61 Parylene coating thickness measurement

The frequency responses of 4 probes are measured before and after the coating process; the results are compared in Table 4. The decrease of the displacement is about 1.5% in average, which is close to the FEA estimation shown in Fig. 59. Because the parylene coating is only 260 nm, the increase of the mass dominates the variation trend of the resonance frequency to, in average, about 97%, which will not affect the flat zone of around 3 kHz.

Table 4 FRF comparison before and after parylene coating

Sample	Before Coating (nm/V)	After Coating (nm/V)	Displacement variation	Before Freq. (kHz)	After Freq. (kHz)	Natural Freq. variation
B14	10.18	9.95	97.74%	59.79	58.19	97.34%
B17	11.38	11.32	99.47%	58.82	57.75	98.18%
C13	12.65	12.50	98.81%	56.91	54.87	96.42%
C16	14.73	14.45	98.10%	58.38	56.42	96.64%

8.1.3 Insulation effect of the Parylene coating

The insulation effect of the parylene coating is first examined by a multimeter. The dc resistance between the bottom and center electrodes is measured for one bare probe and one coated probe. Once the bare probe is soaked in DI water, the resistance immediately starts drifting in the Mohm range. For the coated probe, the multimeter still shows open circuit even two hours after it was put into the DI water.

A more sophisticated examination of the insulation effect of the parylene coating is done by an Aginlent4294A, precision impedance analyzer. The impedance spectrum of one bare probe and a coated probe are measured in the same way to be compared with each other. Because the capacitance varies in respect to the frequency, the comparison of the phase angle will make more sense on checking the insulation effect. For ideal capacitance, the phase angle of its impedance will be -90 degrees. It means the electrical energy is conservative during the charging and discharging process under sinusoidal excitation. The impedance and phase angle values (at 3 kHz) of the two probes is shown in Fig. 62 and Fig. 63. The phase angle of the bare probe drops to -77 degrees from -89 degrees within one hour. The energy efficiency of the probe becomes very poor. In contrast, after soaking into water, the phase angle of the coated probe only decreases from -89 to -88 degrees within 5 hours.

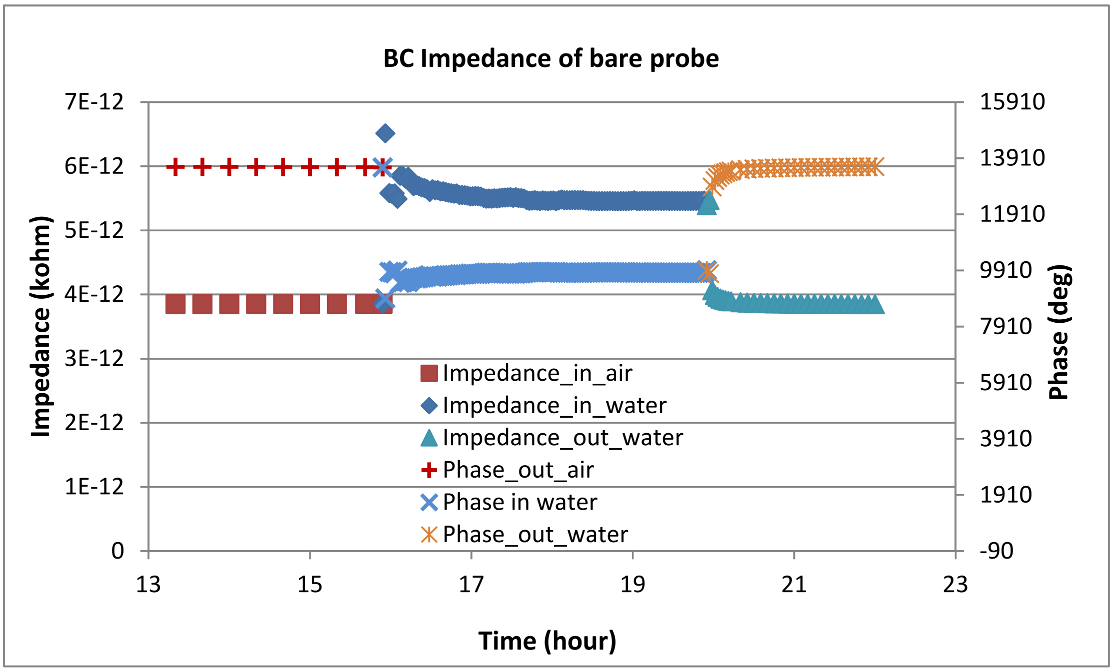

Fig. 62 The impedance variation in DI water over time for the bare probe

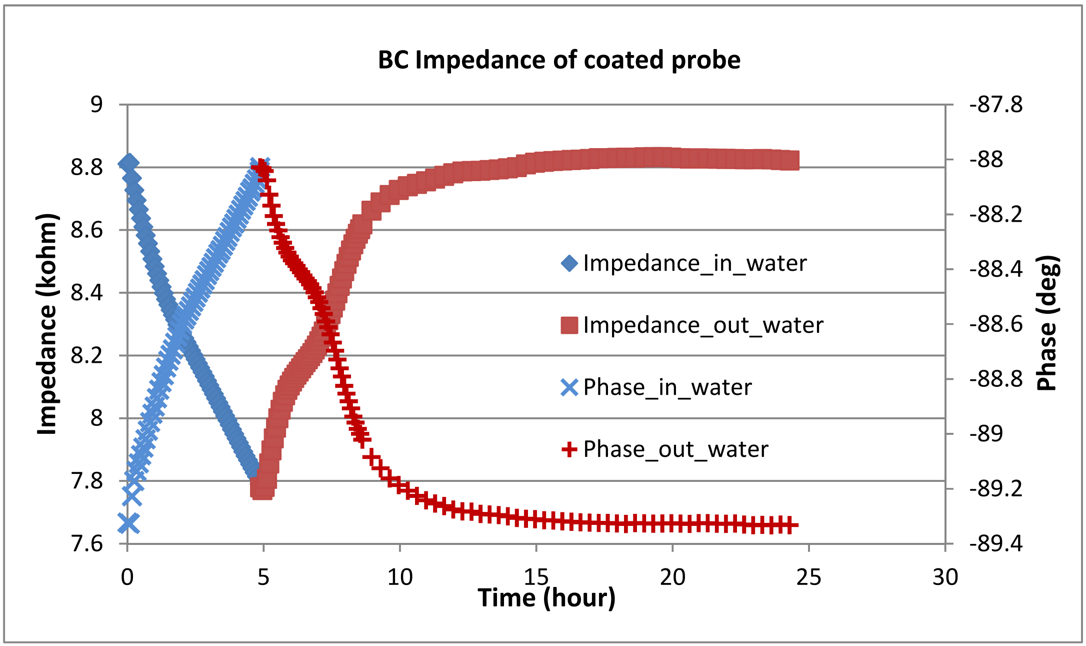

Fig. 63 The impedance variation in DI water over time for the parylene coated probe

The results from the multimeter and impedance analyzer illustrate that the insulation effect of the parylene coating is good in both the dc and ac manner, and the coated probe will be able to work in water without getting shorted.

8.2 Probe working in water over time

8.2.1 Displacement measurement in water

Since DI water is clear to red laser beams, the displacement in the water can also be measured by the LDV as introduced in Chapter 2. However, a correction factor needs to be applied when the measurement is done in water. The LDV measures displacement by comparing the phase difference between the reflected laser beam and another reference beam inside the equipment. Therefore, the measurement results depend on the variation of the wave number between the laser source and the reflection surface. Because the wave number is proportional to the refraction index of the medium, if the reflection surface is in the water, the measurement results need to be corrected by multiplying the reciprocal of the refraction index of the water, which is 1/1.33=0.75.

During the two days impedance test by the multimeter, the displacement of the diaphragm is also measured at 4 different times. After the correction of the refraction of water, the measurement results are listed in Table 5. The displacement increases about 30% from 15.22 nm to 21.5 nm(in average) after being soaked in water for 28 hours. This is different from intuition, because the water should not decrease the stiffness of the diaphragm.

Table 5 Displacement at 3 kHz in water over time (1st time)

Time in water(hour)	In air	0	28	31	54
Raw data of Displacement(nm/V)	15.22	20.3	29.9	28.3	28.1
Corrected Displacement (nm/V)	15.22	15.225	22.425	21.225	21.075

8.2.2 FRF test in water over time

Actually, the measurement of displacement in water over time is difficult to keep consistent due to many unavoidable possible sources of measurement error. For example, as time increases, the water in the petri dish evaporates gradually; the reflection of the laser beam needs to be readjusted; the shining position of the laser beam moves. In order to make sure the increase of the displacement is not coming from measurement error, the same experiment is repeated two more times with different time ranges and time intervals between data points. To eliminate the possibility of drift from the LDV, one set of data is also measured in the air as a reference. All experiment results, as shown in Fig. 64, demonstrate that the displacement increases gradually after soaking in water and gets saturated at about two hours.

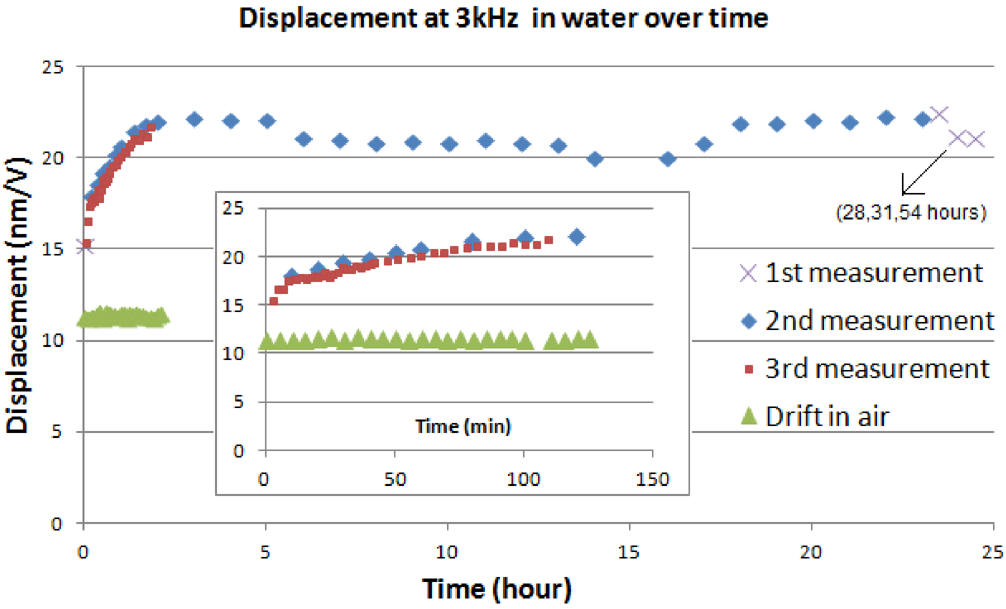

Fig. 64 Displacement (3 kHz) variation in DI water over time

In contrast to the increase of displacement, the resonance frequency almost remains constant, as shown in Fig. 65. This demonstrates that the stiffness of the diaphragm did not decrease in the water ambience. Otherwise, the mass of the diaphragm would have to vary in the same proportion to keep the resonance frequency constant, which is almost impossible.

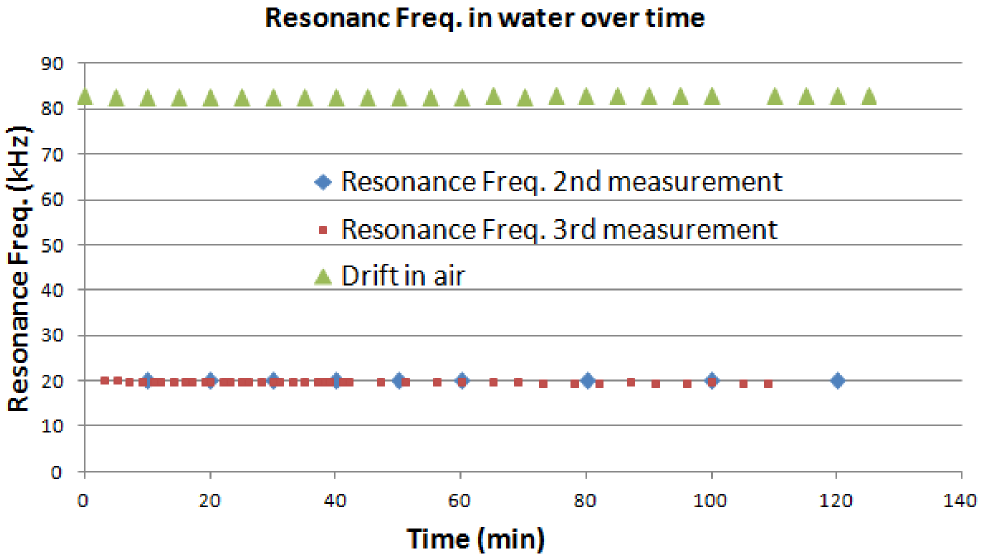

Fig. 65 Resonance frequency in water over time

8.2.3 Impedance test result

Logically, at a certain frequency, the displacement of the PZT diaphragm should only increase for two reasons. One is to decrease the diaphragm stiffness; the other one is to increase the electrical excitation.

Because the first reason is rare, the impedance measurement shown in Fig. 63 was observed more thoroughly to verify the second reason. After being placed into DI water for 5 hours, the impedance value decreased from 8.8 kohm to 7.8 kohm. This trend of impedance values agrees with the second reason of increasing electrical excitation because lower impedance will result in higher current, which will generate higher electrical excitation on the PZT diaphragm. One possible reason for decreasing impedance is that some water goes into the PZT thin film between the bottom and top electrodes, because this will result in larger capacitance, which equals smaller impedance. However, this contradicts the insulation effect of the parylene coating.

8.2.4 Discussion

As mentioned above, water getting into the PZT thin film is one of the possible explanations for the increase in displacement. Although it seems to contradict the parylene coating effect from the macro scale, it makes more sense in the nano scale for several reasons.

First, PZT has a porous structure in the nano scale. The thin film is fabricated by the sol-gel method. One of the crucial steps is the sintering process at 650 ^{o}C to form the desired perovskite structure. As the temperature rises from room temperature to 650 ^{o}C, the PZT sol-gel is actually going through a pyrolysis process. The organic component in the sol gel is evaporated and burned within a couple seconds. The rapid escaping of gas will leave the nano cavities and channels in the PZT thin film. A SEM picture of the PZT surface is shown in Fig. 66.

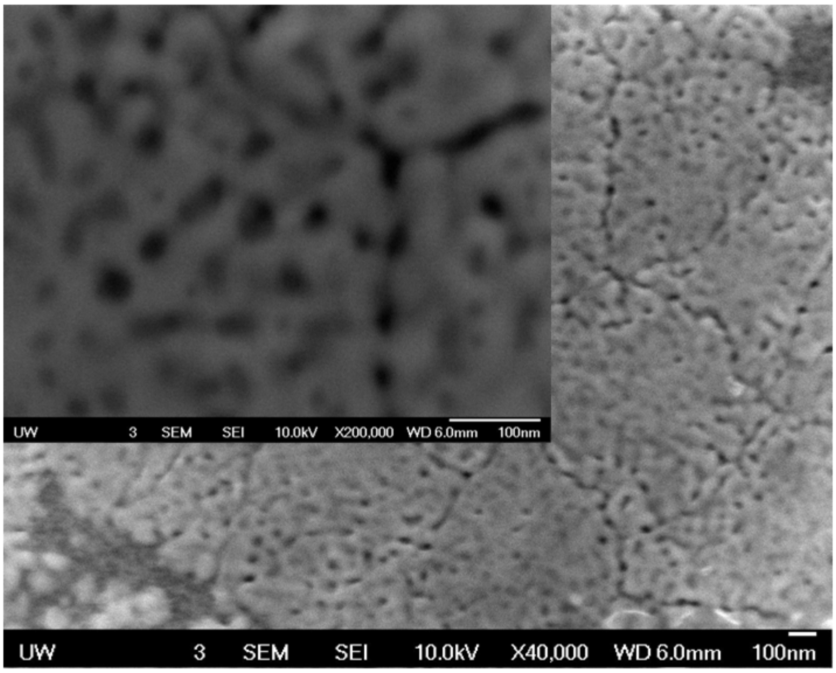

Fig. 66 SEM picture of the porous structure of the PZT surface

Second, the deposition of the top electrode will not be shorted by these nano cavities. Because these nano cavities connected in the 3D structure are distributed through the whole thickness of the PZT thin film and the Ebeam evaporation process is not a conformal coating process, the gold molecules will not be able to reach the bottom electrode or cover all of the cavities. A SEM picture of the top electrode surface is shown in Fig. 67.

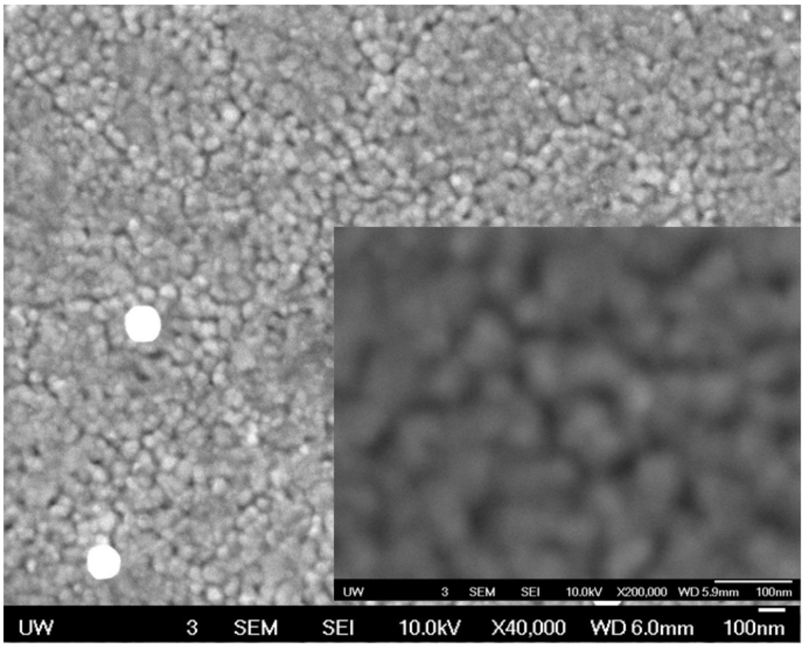

Fig. 67 SEM picture of the porous structure of the top electrode surface

Third, the nano cavities will be partially covered by the conformal coating process of the parylene material. Especially, the top electrode will be well protected because the gold molecules only reach the superficial surface of the PZT thin film.

Because of these three reasons, the water molecules are able to get into the PZT thin film without shorting the top and bottom electrodes. As the dielectric constant of water is much higher than that of the air, the electric field in the water will be much lower than in the same space when taken by the air. When the excitation voltage is fixed, the electric field in the PZT material will become stronger.

More evidence that the water actually goes into the PZT material is shown in Fig. 68. The impedance measurement started at the same time when the probe was taken out of the water after being soaked for 4 days and 10 hours. The measurement result is clearly divided into two stages. In the first stage, the impedance increases linearly with time. In the second stage, the impedance suddenly increases much faster and gets saturated to the final stable value. These two stages correspond to two different evaporation stages, respectively. In the first stage, the nano cavities are full of water. The evaporation rate is proportional to the superficial area of the nano cavities, which is a constant, so the impedance increases linearly. In the second stage, as more water is evaporated, air starts to get back to the nano cavities. Because of the capillary force, the surface area and evaporation rate of the water increases exponentially. This causes the impedance to get saturated exponentially.

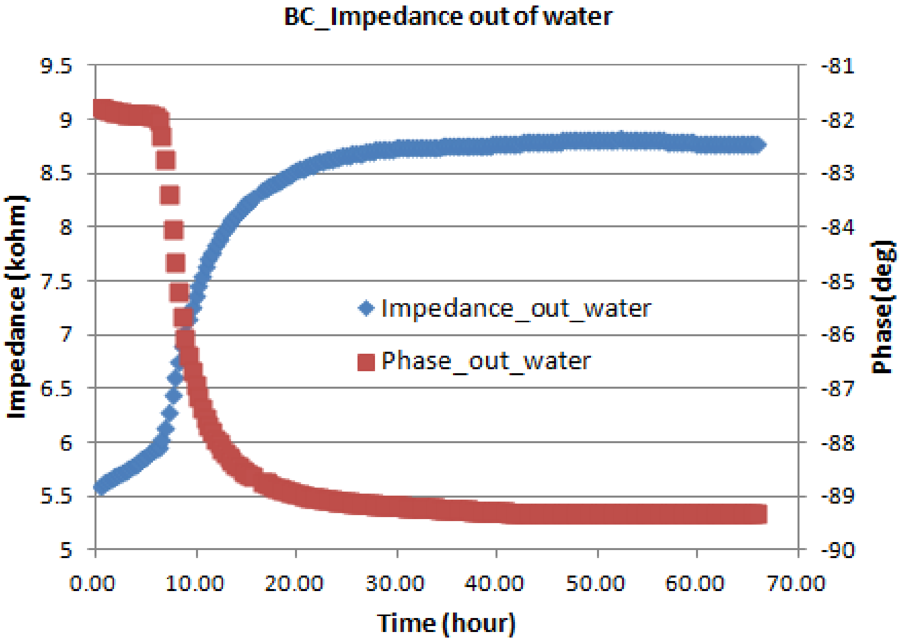

Fig. 68 Impedance after the probe is out of the water

The saturation of the displacement increase that occurs at about two hours into the experiment can also be explained by the water absorption process. The same as evaporation, the water absorption by the nano cavities take time. Only water that gets between the center and bottom electrodes will increase the displacement. After being placed in water for two hours, the nano cavities under the center electrode are saturated with water. While the probe tail is coated with silicone with different thicknesses, the other part of the PZT thin film is still absorbing water; the impedance will keep decreasing and the displacement gets saturated, as is shown in Fig. 63 and Fig. 64.

8.3 Summary

The conformal parylene coating is proved to be able to protect the probe from being shorted by a water environment. The thickness of parylene coating should be less than 1 μm to reduce the displacement less than 10%. A 30% increase of displacement is found after the probe is soaked in DI water for two hours. One of the possible reasons for this is that the DI water gets into the nano cavities and channels in the PZT thin-film layer.

Chapter 9 Conclusions and future work

9.1 Conclusions

This dissertation has illustrated the need to research and develop PZT thin-film microprobe devices for animal testing to demonstrate the feasibility for using a novel HCI hearing aid in hearing rehabilitation. In line with this research objective, a dual top electrodes design has been created to enhance the actuator's displacement by 30%, and a promising procedure has been developed to dice the PZT thin-film actuators into the shape of a probe from a wafer. Furthermore, it has been found that the parylene coating is an effective insulation solution for the aqueous environment in the cochlea.

The dual top electrodes design is studied via finite element analysis and verified by experimental results. The optimal size of the center electrode and the outer electrode has been found to be about half of the opening size of the silicon residue. When the two electrodes are driven out of phase, the displacement increases by about 30% when compared to previously designed actuators with single top electrode. Moreover, the enhancement of the displacement is independent from possible fabrication defects, although the phase difference between the two top electrodes for maximum displacement might change.

The probe shaped actuator has been fabricated. It has been demonstrated that an etching width of 200 μm is enough to accomplish the dicing work through DRIE process, which is compatible with existing fabrication recipes. It has also been found that the exposed length of the probe should be less than 3 mm to maintain consistent performance when the excitation frequency is lower than 10 kHz.

It has been demonstrated that the parylene coating is a valid insulation; the coating prevents the electrodes from being shorted. A finite element analysis shows that a coating thickness of 1 μm or less causes displacement to decrease by less than 10%. The results of the experiment illustrate that a coating thickness of 250 nm reduces the displacement to 98%, which is consistent with the finite element analysis results. It has also been shown that a parylene coating of 250 nm may work as an insulation layer for at least 54 hours, which is long enough for animal testing. In addition, it has been found that the displacement increases by about 30% when the probe is soaked in water for more than 2 hours. One of the possible reasons for this is that the DI water gets into the PZT thin film gradually, without shorting the electrodes under the protection of the parylene coating. This would cause the electric field applied on the PZT material to become larger, which leads to a larger displacement. This explanation is also supported by the results of the impedance measurement during the process of water evaporation.

9.2 Future work

Although the probe device is ready to function as an intracochlear acoustic actuator, there are still some important issues that should be studied before animal testing occurs.

First, the added mass effect of the aqueous environment should be studied. Although the effect of the added mass would not affect the displacement of the actuators, it would significantly reduce the first resonance frequency. The experimental results show that the added mass of the DI water will reduce the first resonance frequency from 80 kHz to 20 kHz. Since the physical properties of the perilymph might be different from the DI water, it is necessary to show that the added mass of the perilymph will not reduce the resonance frequency to lower than 3 kHz.

Second, the squeeze film damping effect of the fluid should be studied. Because the space of the cochlea is small, the distance between the actuator and the basilar membrane would be very small. This will cause a squeeze damping effect when the actuator is vibrating. Determining the effect of this damping is very important to assure the actuator functions properly in the cochlea.

Third, the self testing mode of the actuators with dual top electrodes should be studied. When the actuator is working in the cochlea, the LDV will not be able to measure the displacement. Therefore, one of the top electrodes should be able to work as a sensor, while the other electrode works as an actuator. In this way, the displacement of the actuator could be examined by itself, which is important for animal testing.

Appendix A Fabrication Recipe of probe device

1.0 Silicon Oxidation

1.1 Cleaning Process

1.1.1 Nanostrip 10 min => 3 Cycles Dump Rinse Dry

1.1.2 HF (48%-49%) Dip (or BOE 2 min) => 3 Cycles Dump Rinse

1.1.3 Nanostrip 10 min => 3 Cycles Dump Rinse Dry

1.1.4 SC1 at 70°C 15 min => 3 Cycles Dump Rinse Dry

1.1.5 SC2 at 70°C 15 min => 3 Cycles Dump Rinse Dry

- SC1 1:1:5 = ammonium hydroxide : hydrogen peroxide : DI water
- $NH_4OH : H_2O_2 : H_2O$
- SC2 1:1:5 = hydrochloric acid : hydrogen peroxide : DI water
- $HCL : H_2O_2 : H_2O$
- Use the big rectangular crystal bowl
- Use 400ml, 400ml, 2000ml, so the 4” wafer can be covered
- SC1, SC2 Heating take about 40 min to 70°C

1.2 WTC MRL 812 furnace tube #3

- Target is 5000Å, it takes about 180 min
- Need two bufflalo wafers on each side of the boat
- Need to start the process early in the morning
- Over thickness is better than thinner, the color should be purple or dark pink.

“before oxidation”

		Time	Target	N_2 Sol	N_2 SP	O_2 Sol	O_2 SP	N_2/H_2	N_2 BP
1	Time	1.0	20	Open	60	Open	10.0	Closed	Closed
2	Ramp	10.0	1100	Open	60	Closed	0.0	Closed	Closed
3	Dwell	5.0	Xxx	Open	60	Closed	0.0	Closed	Closed
4	Dwell	30.0	Xxx	Open	30	Open	10.0	Closed	Closed
5	Dwell	5.0	Xxx	Open	60	Closed	0.0	Closed	Closed
6	Ramp	10.0	20	Open	60	Closed	0.0	Closed	Closed
7	End	Xxx	Xxx	Closed	60	Closed	0.0	Closed	open

“oxidation”

		Time	Target	N_2 Sol	N_2 SP	O_2 Sol	O_2 SP	N_2/H_2	N_2 BP
1	Time	1.0	20	Open	60	Open	10.0	Closed	Closed
2	Ramp	10.0	1050	Open	60	Closed	0.0	Closed	Closed
3	Dwell	5.0	Xxx	Open	60	Closed	0.0	Closed	Closed
4	Dwell	180.0	Xxx	Open	30	Open	10.0	Closed	Closed
5	Dwell	5.0	Xxx	Open	60	Closed	0.0	Closed	Closed
6	Ramp	10.0	20	Open	60	Closed	0.0	Closed	Closed
7	End	Xxx	Xxx	Closed	60	Closed	0.0	Closed	open

Appendix A Fabrication Recipe of probe device

1.3 Measurement

5 points measurement

Appendix A Fabrication Recipe of probe device

2.0 Silicon Nitride

2.1 Cleaning Process

2.1.12.1.1 Nanostrip 10 min => 3 Cycles Dump Rinse Dry
2.1.22.1.2 HF (48%-49%) Dip (or BOE 2 min) => 3 Cycles Dump Rinse
2.1.32.1.3 Nanostrip 10 min => 3 Cycles Dump Rinse Dry
2.1.42.1.4 SC1 at 70°C 15 min => 3 Cycles Dump Rinse Dry
2.1.52.1.5 SC2 at 70°C 15 min => 3 Cycles Dump Rinse Dry

SC1 1:1:5 = ammonium hydroxide : hydrogen peroxide : DI water
$NH_4OH : H_2O_2 : H_2O$
SC2 1:1:5 = hydrochloric acid : hydrogen peroxide : DI water
$HCL : H_2O_2 : H_2O$

- Use the big rectangular crystal bowl
- Use 400ml, 400ml, 2000ml, so the 4” wafer can be covered
- SC1, SC2 Heating take about 40 min to 70°C

2.2 WTC LPCVD Tube #3

- LS 5:1 , for 39-40 min (line 65 in the recipe)
- Target: 2000 Å, the color should be shining green
- Need to start at morning before 9am
- Need 18 process wafer, 2 measurement wafer, and buffalo wafers

2.3 Measurement

5 points measurement

Appendix A Fabrication Recipe of probe device

3.0 *Alignment Mark*

- About 70 min for 2 wafers' pattern transfer

3.1 Patterning alignment mark with AZ 1518

3.1.1 Precleaning EKC830 5 min

3.1.2 AZT300T 2 min

3.1.3 3 Cycles Dump Rinse Dry

3.1.4 Primer P-20 0/0/5 - 500/250/5 – 1200/600/15

3.1.5 Photoresist AZ1518 0/0/5 - 500/250/5 – 1200/600/30

3.1.6 Softbake 100°C 3 min

3.1.7 UV exposure 22sec

3.1.8 Develop AZ351 4:1 130 sec

3.1.9 hardbake 110°C 3 min

- This recipe can survive 3 times of 4 min Nitride RIE

3.2 Dry etch by RIE

Nitride recipe for 14 min or shorter

Power set	RF power	Process time	End Pt set	Base press.	SF_6 set
150	100	100	840	150	50

3.3 Clean photoresist layer

Use acetone to remove the photoresist layer or RIE clean recipe for 3~5 min

Power set	RF power	Process time	End Pt set	Base press.	O_2 set
100	150	100	300	150	100

3.4 Cleaning

3.4.1 Precleaning EKC830 10 min

3.4.2 AZT300T 5 min

3.4.3 6 Cycles Dump Rinse Dry

Appendix A Fabrication Recipe of probe device

4.0 Ti/Pt Bottom Electrode

4.1 Pre-cleaning

4.1.1 Nanostrip 10 min => 3 Cycles Dump Rinse Dry

4.1.2 SC1 at 70°C 15 min => 3 Cycles Dump Rinse Dry

4.1.3 SC2 at 70°C 15 min => 3 Cycles Dump Rinse Dry

4.2 Ti/Pt deposition in E-Beam AI:

Material	Target	Rate	Time
Ti	500 A	1 A/s	
Pt	1000 A	5 A/s	

- Beam position adjustment:
- Longitudinal clockwise: moving forward
- Latitudinal clockwise: moving leftward
- Lower deposition rate for Ti result in smaller deposition particle and more adhesive layer

4.3 Cleaning Process

4.3.1 EKC830 10 min

4.3.2 AZT300T 5 min

4.3.3 6 Cycles Dump Rinse Dry

- Never use SC1/SC2 after bottom electrode deposition

4.4 Bottom Electrode Annealing

#Tube4

		Time	Target	N_2 Sol	O_2 Sol	N_2/H_2 Sol	N_2 BP Sol
1	Time to Target	1.0	20	Closed	Closed	Closed	Closed
2	Ramp rate	13.0	800	Closed	Closed	Closed	Closed
3	Dwell	60.0	Xxx	Closed	Closed	Closed	Closed
4	Ramp rate	13	20	Closed	Closed	Closed	Closed
5	End	Xxx	xxx	Closed	Closed	Closed	Open

4.5 Measurement

4.5.1 SEM surface profile(9 points)

Appendix A Fabrication Recipe of probe device

5.0 PZT Sol Recipe

- Takes about 4.5 hours
- Calibrate Finnepipette before using
- Normal mixing rate is 300~500 rpm
- Final volume is approximately 75 ml

5.1 Pb acetate solution

5.1.1 Dissolve 24.48g Pb Acetate in 15.2ml(16g) acetic acid. Use a 400ml beaker.

5.1.2 Stir consistently with a stir bar speed=5

5.1.3 Heat up the solution to 110°C. Use aluminum foil to keep water vapor out.

5.1.4 Dwell at 110°C for 5~15 min. Do not seal parafilm too tight. Let the water vapor out.

5.1.5 Cool down to room temperature.

5.2 Mix other material

5.2.1 Mix14.7ml(15.932g) Zr n-propoxide, and 8.4ml(8.128g) Ti-isopropoxide. wait for 10~30 min at speed=5. Seal well in a 250ml beaker.

5.2.2 Mix Zr and Ti mixture to Pb solution. Wait for 7.5~15 min. Try to be as fast as possible.

5.2.3 Mix 16ml(16g) DI water as slow as possible. Wait for 15 min.

5.2.4 Mix 3.4ml(4g) lactic acid. Wait for 15 min.

5.2.5 Mix 4.8ml(6g) glycerin(glycerol). Wait for 15 min. load glycerin 2 min before hand because it’s sticky.

5.2.6 Mix 3.6ml(4g) ethylene glycol. Wait for 15 min.

5.2.7 Filter

5.3 Diluted PZT sol

5.3.1 PZT sol : acetic acid = 1:1

5.3.2 Ultrasound for 30 min.

- Acetic acid: 15.2ml = 3.8 x 4
- Zr: 14.7ml = 3.8 x 3 + 3.3
- Ti: 8.4ml = 4.2 x 2
- DI: 16ml = 4 x 4
- Lactic acid: 3.4ml
- Glycerin: 4.8ml

Appendix A Fabrication Recipe of probe device

- Ethylene glycol: 3.6ml

Appendix A Fabrication Recipe of probe device

6.0 PZT film fabrication

- It takes about 5 hours to finish the PZT film
- Ultrasound the PZT (diluted) sol for 15 min
- It takes 16 min to tape 2 wafers

6.1 Pre-cleaning

6.1.1 EKC830 10 min

6.1.2 AZT300T 5 min

6.1.3 6 Cycles Dump Rinse Dry

6.2 PZT film deposition

6.2.1 Timing procedure

#	pre	0-15	15-30	30-46	45-60	60-75	75-90	90-105
1	2tape	1spin/peel	1sinter	3pictures		2tape/spin	1peel	cycle to 15-30
2	1tube on	2tape/spin	2peel	1sinter	2pictures		2tape/spin	
3			3tape/spin	2peel	1sinter	1pictures		

6.2.2 Spin PZT film 500/250/5 4500/1500/20 0/0/1

- A good film looks smooth. there should not be any shinning spot or openging

6.2.3 Sinter Tube4 or Tube3

- Put the wafers on the metal shelf right after taking out from the tube for rapid cooling

		Time	Target	N_2 Sol	O_2 Sol	N_2/H_2 Sol	N_2 BP Sol
1	Time to Target	1.0	20	Closed	Closed	Closed	Closed
2	Ramp rate	13.0	650	Closed	Closed	Closed	Closed
3	Dwell	240	Xxx	Closed	Closed	Closed	Closed
4	Ramp rate	13	450	Closed	Closed	Closed	Closed
5	End	xxx	xxx	Closed	Closed	Closed	Open

Appendix A Fabrication Recipe of probe device

7.0 Top Electrode (I)

7.1 Cleaning Process

7.1.1 EKC830 10 min

7.1.2 AZT300T 5 min

7.1.3 6 Cycles Dump Rinse Dry

7.2 Top electrode Cr/Au evaporation

Material	Target	Rate	Time
Cr	250 A	1 A/s	
Au	5000 A	5 A/s	

7.3 Cleaning Process

7.3.1 EKC830 10 min

7.3.2 AZT300T 5 min

7.3.3 6 Cycles Dump Rinse Dry

7.4 Top electrode patterning

- Use CEE #2 for 3 Inch wafers
- For AB-M infrared alignment, use “8” or “0” filter of the camera
- Do not turn on the vacuum of the chunk to prevent PZT film from breaking

step	Process	Tools	Parameters
1	Primer	P-20	0/0/5 500/250/5 1200/600/15
2	PR	AZ1518	0/0/5 500/250/5 2500/1250/15
3	Softbake	100°C hotplate	3 min
4	UV	AB-M	12 sec
5	Develop	H_2O:AZ351 4:1	75~80 sec
6	Rinse & dry	DI water	
7	Hardbake	110°C hotplate	3 min

7.5 Top electrode etch

- Etch rate depends on agitation and temperature.
- Au etchant speed: 40A/s = 240 A/min at 40°C
- Cr etchant speed: 28A/s = 168 A/min at 25°C

Material	Thickness	Etchant	Etchtime
Au	500A		50 sec
Cr	200A		30 sec
Au	5000A		3 min
Cr	250A		40sec

7.6 Photoresist strip

7.6.1 EKC830 10 min

Appendix A Fabrication Recipe of probe device

7.6.2 AZT300T 5 min

7.6.3 6 Cycles Dump Rinse Dry

Appendix A Fabrication Recipe of probe device

8.0 Top Electrode (II)

8.1 Cleaning Process

8.1.1 EKC830 10 min

8.1.2 AZT300T 5 min

8.1.3 6 Cycles Dump Rinse Dry

8.2 Top electrode patterning

step	Process	Tools	Parameters
1	Primer	P-20	0/0/5 500/250/5 1200/600/15
2	PR	NR71-1000PY	0/0/5 500/250/10 3000/1500/40 (950-1050 nm thick)
3	Softbake	150°C hotplate	1 min(2 min for oxide coating)
4	Softbake	165°C hotplate	4min
5	UV	AB-M	30 sec (366nm wavelength 390 mJ/cm² f 1 μm thick film)
6	Hardbake	100°C hotplate	1 min(2 min for oxide coating)
7	Hardbake	110°C hotplate	4min
8	Develop	$H_2O:RD_6$ 1:3	50sec (75~80 sec)

8.3 Top electrode evaporation

Material	Target	Rate	Time
Cr	250 A	1 A/s	
Au	1000 A	5 A/s	

8.4 Strip

8.4.1 Acetone or RR41 overnight

8.4.2 6 Cycles Dump Rinse Dry

Appendix A Fabrication Recipe of probe device

9.0 Back Side cavity

9.1 Cleaning processing

9.1.1 EKC830 10 min

9.1.2 AZT300T 5 min

9.1.3 6 Cycles Dump Rinse Dry

9.2 Back side patterning

- The thickness of the PR is around 13.32um. this recipe can survive 465 loops in DRIE
- If the PR is spun on at 1500/1000/30, the result thickness is about 10.92um, enough for 450 loops in DRIE

step	Process	Tools	Parameters
1	Primer	P-20	0/0/5 500/250/5 3000/1000/15
2	PR	AZ4620	0/0/5 500/250/5 1100/500/20
3	Softbake	60°C hotplate	2 min
4	Softbake	90°C hotplate	6 min
5	UV	AB-M	70 sec
6	Develop	H_2O:AZ400K 4:1	5 min or longer
7	Rinse & dry	DI water	
8	Hardbake	110°C hotplate	3 min

9.3 Initial RIE

- Run nitride recipe for about 12~16 min to get rid of all nitride and oxide on the wafer
- Pure wafer should shine with sliver color
- Do not use oxide recipe because it will etch PR very much
- Etch oxide and nitride away before attaching the wafer to the 4 inch wafer. The heat in RIE will melt the PR and debond the PR adhesive.

Power set	RF power	Process time	End Pt set	Base press.	SF_6 set
150	100	100	720	150	50

9.4 Attach 3” wafer to 4” wafer

step	Process	Tools	Parameters
1	Primer	P-20	0/0/5 500/250/5 3000/1000/15
2	PR	AZ4620	0/0/5 500/250/5 1100/500/20
3	Attach	Soft contact	
4	Hardbake	110°C hotplate	5 hour

9.5 D-RIE

Appendix A Fabrication Recipe of probe device

10.0 Version Log

1.0	Dec. 2008 Main structure
1.1	Feb. 3rd 2009 Write 1~3; update format
1.2	Mar. 4th 2009 Write 4~6; update format of “detail comment”
1.3	Mar. 7th 2009 write 7~9; update format of heading2 and move the title to the header
1.4	Correct the recipe for lift off parameters

Appendix B Basic Program for Automatic Impedance Measurement

```
10 DIM File$[9],Tdate$[20],Timed$[9]
20 INTEGER Interval ! Time_inverval [sec]
30 Interval=1200 ! Time_inverval [sec]
40 CLEAR SCREEN
50 IF SYSTEM$("SYSTEM ID")="HP4294A" THEN
60 ASSIGN @Agt4294 TO 800
70 ELSE
80 ASSIGN @Agt4294 TO 717
90 END IF
100 !
110 Seconds=TIMEDATE+Interval
120 Timed$=TIME$(Seconds-Interval)
130 Tdate$=DATE$(Seconds-Interval)
140 File$=Tdate$[4,4]&Tdate$[1,2]&Timed$[1,2]&Timed$[4,5]
150 OUTPUT @Agt4294;";MEAS CPR"
160 OUTPUT @Agt4294;";SAVDAT ON"
170 OUTPUT @Agt4294;";SAVDTRC ON"
180 OUTPUT @Agt4294;"SAVDASC"&" """&"S"&File$&""""
190 PRINT File$&"IS SAVED"
200 Measure_start: !
210 Timed$=TIME$(Seconds)
220 Tdate$=DATE$(Seconds)
230 File$=Tdate$[4,4]&Tdate$[1,2]&Timed$[1,2]&Timed$[4,5]
240 WAIT 1050 ! Rough waiting time before go into while loop [sec]
250 OUTPUT @Agt4294;";CONT"
260 WHILE TIMEDATE<Seconds
270 END WHILE
280 OUTPUT @Agt4294;";HOLD"
290 OUTPUT @Agt4294;"SAVDASC"&" """&"S"&File$&""""
300 PRINT File$&" IS SAVED"
310 Seconds=Seconds+Interval
320 GOTO Measure_start
330 END
```

Notes:

1.This program measure the parallel capacitance and resistance automatically.

2.This program needs to be manually stopped from the front panel of the equipment!

3.The floppy disk needs to be replaced manually when the space is not enough for one data file (19k)

Appendix C Design of the Holder for Probes

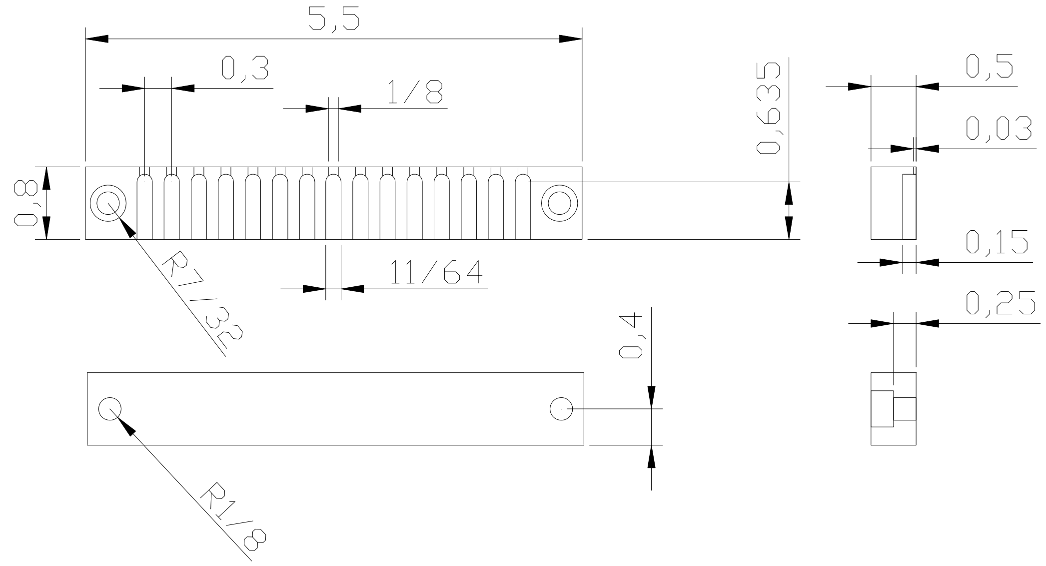

Bibliography

[1] Wardlow, Jesse. "Sudden Hearing Loss" *westsuburbanent.com*. West Suburban Ear, Nose & Throat Center (2012). Web. 6 Apr. 2012

[2] Fitzakerley, Janet. "StereociliaDamage" d.umn.edu. University of Minnesota Medical School Duluth 22 Feb. (2012). Web. 6 Apr. 2012

[3] Gray, Henry/30th American ed. Anatomy of The Human Body. Philadelphia: Lea & Febiger (1985)

[4] Gantz, B.J., Turner, C.W., Gfeller, K.E., & Lowder, M.W. “Preservation of hearing in cochlear implant surgery: Advantages of combined electrical and acoustical speech processing” Laryngoscope, vol.113, 796-802, (2005)

[5] B. J. Gantz and C. W. Turner, "Combining acoustic and electrical hearing," Laryngoscope, vol. 113, 1726-1730, (2003)

[6] B. S. Wilson, D. T. Lawson, J. M. Muller, R. S. Tyler, and J. Kiefer, "Cochlear implants: Some likely next steps," Annual Review of Biomedical Engineering, vol. 5, 207-249, (2003)

[7] M. F. Dorman, A. J. Spahr, P. C. Loizou, C. J. Dana, and J. S. Schmidt, "Acoustic simulations of combined electric and acoustic hearing (EAS)," Ear and Hearing, vol. 26, 371-380, (2005)

[8] J. Kiefer, M. Pok, O. Adunka, E. Sturzebecher, W. Baumgartner, M. Schmidt, J. Tillein, Q. Ye, and W. Gstoettner, "Combined electric and acoustic stimulation of the auditory system: Results of a clinical study," Audiology and Neuro-Otology, vol. 10, 134-144, (2005)

[9] Y. Y. Kong, G. S. Stickney, and F. G. Zeng, "Speech and melody recognition in binaurally combined acoustic and electric hearing," Journal of the Acoustical Society of America, vol. 117, 1351-1361, (2005)

[10] W. N. Yao, C. W. Turner, and B. J. Gantz, "Stability of low-frequency residual hearing in patients who are candidates for combined acoustic plus electric hearing," Journal of Speech Language and Hearing Research, vol. 49, 1085-1090, (2006)

[11] R. H. Gifford, M. F. Dorman, S. McKarns, and A. J. Spahr, "Combined electric and contralateral acoustic hearing: Word and sentence recognition with bimodal hearing," Journal of Speech Language and Hearing Research, vol. 50, 835-843, (2007)

[12] Y. Y. Kong and R. P. Carlyon, "Improved speech recognition in noise in simulated binaurally combined acoustic and electric stimulation," Journal of the Acoustical Society of America, vol. 121, 3717-3727, (2007)

[13] N. Li and P. C. Loizou, "A glimpsing account for the benefit of simulated combined acoustic and electric hearing," Journal of the Acoustical Society of America, vol. 123, 2287-2294, (2008)

[14] C. C. Lee, C. R. Hume, G. Z. Cao, and I. Y. Shen, "Temporary Packaging of PZT Thin-Film Microactuators," Integrated Ferroelectric, vol. 101, 121-131, (2008)

[15] S. N. Merchant, M. E. Ravicz, and J. J. Rosowski, "Acoustic Input Impedance of the Stapes and Cochlea in Human Temporal Bones," Hearing Research, vol. 97, 30-45, (1996)

[16] R. Aibara, J. T. Welsh, S. Puria, and R. L. Goode, “Human middle-ear sound transfer function and cochlear input impedance” Hearing Research, vol. 152, 100-109, (2001)

[17] S. Puria, "Measurements of human middle ear forward and reverse acoustics: Implications for otoacoustic emissions," Journal of Acoustical Society of America, vol. 113, 2773-2789, (2003)

[18] B. Jaffe, W.R. Cook Jr., and H. Jaff, Piezoelectric Ceramics, London, New York: Academic Press, (1971).

[19] “Perovskite structure of PZT” en.wikipedia.org. N.p. 5. Aug. (2010). Web. 6. Apr. 2012

[20] L. E. Cross, Ferroelectric Ceramics-Tutorial Reviews, Theory, Processing and Applications, N. Setter and E. L. Colla,eds, Monte Verit`a, Zurich, (1993)

[21] Polla, Dennis L. Francis, Lorraine F. “Processing and characterization of piezoelectric materials and integration into microelectromechanical systems”, Annual Review of Materials Science 28, 563-597 (1998)

[22] M. T. N. Pham, B. A.Boukamp, G. Rijnders, H. J. M. Bouwmeester, D. H. A. Blank, “Pulsed laser deposition of PZT/Pt composite thin films with high dielectric constants,” Applied Physics A: Materials Science and Processing, vol. 79, 907-10, (2004)

[23] K. Kakimoto, H.Ohsato, H. Kakemoto, Y. Masuda, “Stoichiometry and crystal orientation of YAG-PLD derived ferroelectric PZT thin film,” Journal of the European Ceramic Society, vol. 24, 993-7, (2004)

[24] P. Verardi, M. Dinescu, F. Craciun, “Pulsed laser deposition and characterization of PZT thin films,” Applied Surface Science, vol 154-155, 514-18, (2000)

[25] Y. Chen, L. Zheng, C. Lin, X. Xu, and S. Zou, “Pulsed excimer laser deposition and rapid thermal annealing of ferroelectric Pb(Zr0.52Ti0.48)O3 thin films Si-on-Insulator,” Materials Research Society symposium proceedings, Ferroelectric thin films IV, vol. 361, 563-68, (1994)

[26] Z. Wang, I. Karibe, R. Maeda, and H. Kokawa, “Preparation of Lead Zirconate Titanate thin films derived by hybrid processing: Sol-gel method and laser ablation,” Journal of the American Ceramic Society, vol. 85, no. 12, 3108-10, (2002)

[27] Y. Luo, M. Lu, T. Cui, "A polymer-based bidirectional micropump driven by a PZT bimorph", Microsystem Technologies 17, 403-409 (2011).

[28] J. Akedo, M. Lebedev, “Fabrication of microfluidic-devise (diffuser or mixer) using aerosol deposition method” Nano- and Microtechnology: Materials, Processes, Packaging, and Systems, 234-240 (2002).

[29] T. Kobayashi, R. Maeda, T. Itoh, “Low speed piezoelectric optical microscanner actuated by piezoelectric microcantilevers using LaNiO3 buffered Pb(Zr,Ti)O3 thin film”, Smart Materials and Structures 18, (2009).

[30] E. J. Ruggiero, D. J. Inman, “Modeling and control of a 2-d membrane mirror with a PZT bimorph”, International Mechanical Engineering Congress and Exposition, (2006)

[31] Y. Hishinuma, E. Yang, “Piezoelectric unimorph microactuator arrays for single-crystal silicon continuous-membrane deformable mirror”, Journal of Microelectromechanical Systems 15, 370-379 (2006)

[32] Y. Choe, S. Chen, E. S. Kim, “High fidelity loud microspeaker based on PZT bimorph diaphragm”, NSTI Nanotechnology Conference and Expo 2, 316-319 (2010).

[33] J. Cho, S. Jang, H. Nam, “A Piezoelectrically actuated mems speaker with polyimide membrane and thin film pb(zr,ti)o3(pzt) actuator”, Integrated Ferroelectrics 105, 27-36 (2009) .

[34] P.Y. Yeh, Y. Le, J. Kizhakkedathu, M. Chiao, “An investigation of vibration-induced protein desorption mechanism using a micromachined membrane and PZT plate”, Biomedical Microdevices 10, 701-708 (2008).

[35] C. Lee, C. Hume, G. Cao, I. Shen, “A feasibility study of PZT thin-film microactuators for hybrid cochlear implants”, in: Proceedings of the 2005 27th Annual International Conference of the Engineering in Medicine and Biology Society, IEEE-EMBS, 1929–1932, (2005)

[36] H. Ma, S. Huang, Y. Cheng, C. Yu, C. Hou, A. Su, “Study of proton exchange membrane fuel cells (PZT-PEMFCS) with nozzle and diffuser”, 7th International Conference on Fuel Cell Science, Engineering, and Technology, Compendex 9-15, (2009)

[37] M. Changki, L.J. Radziemski, W.W. Clark, “Analysis of PMN-PT and PZT circular diaphragm energy harvesters for use in implantable medical devices”, Active and Passive Smart Structures and Integrated Systems 6525, 7-16, (2007)

[38] D. Shen, J. Ajitsria, S. Choe, D. Kim, “Evaluation and modeling of power generator with bimorph PZT cantilever”, 2006 MRS Materials Research Society 966, 275-280, (2006).

[39] D. Isarakron, D. Briand, A. Sambri, S. Gariglio, J.M. Triscone, F. Guy, J.W. Reiner, C.H. Ahn, N.F. Derooij, “Finite element analysis and experiments on a silicon membrane actuated by an epitaxial PZT thin film for localized-mass sensing applications”, Sensors and Actuators, B: Chemical 153, 54-63, (2011).

[40] T. Xu, J. Miao, Y. Liu, C.M. Li, “Investigation of the effect of adsorption induced surface stress on the resonant frequency of PZT membrane based biosensors”, 5th IEEE International Conference on Nano/Micro Engineered and Molecular Systems, NEMS, Compendex, 569-572, (2010)

[41] S. Xiong, H. Kawada, H. Yamanaka, T. Matsushima, P. Muralt, “Highly sensitive PZT thin film ultrasonic micro-sensors with grooved diaphragm”, 16th IEEE International Symposium on the Applications of Ferroelectrics, Compendex, 707-710 (2007)

[42] K. Yamashita, K. Tomiyama, K. Yoshikawa, M. Noda, M. Okuyama, “Resonant frequency tuning of piezoelectric ultrasonic microsensors by bias voltage application to extra top-electrodes on PZT diaphragms”, Ferroelectrics 408, 48-54 (2010)

[43] V. Mohammadi, M.H. Sheikhi, S. Torkian, A. Barzegar, E. Masumi, S. Mohammadi, “Design, modeling and optimization of a piezoelectric pressure sensor based on thin-film PZT diaphragm

contain of nanocrystalline powders", 6th International Symposium on Mechatronics and its Applications, Compendex (2009).

[44] Q. Guo, "Development of ThiniFilm Based Microdevices and Process Enhancement for Making the Same", PhD Thesis, University of Washington, Chapter 3 (2012)

[45] C. Lee, Q. Guo, G.Z. Cao, I.Y. Shen, "Effect of electrode size and silicon residue on piezoelectric thin-film membrane actuators", Sensors and Actuators A 147, 279–285 (2008).

[46] L. Lian, N.R. Sottos, "Stress effects in sol ‑ gel derived ferroelectric thin films", Journal of Applied Physics 95 January 629 ‑ 634, (2004).

[47] S. Corkovic, R. Whatmore, Q. Zhang, "Development of residual stress in sol ‑ gel derived Pb(Zr,Ti)O3 films: an experimental study", Journal of Applied Physics 103 April (2008).

[48] S. Sengupta, S. Park, D. Payne, L. Allen, "Origins and evolution of stress development in sol ‑ gel derived thin layers and multideposited coatings of lead titanate", Journal of Applied Physics 83 February 2291 ‑ 2296, (1998).

[49] E. Hong, R. Smith, S. Krishnaswamy, C. Freidhoff, S. Trolier-McKinstry, "Residual stress development in Pb(Zr,Ti)O3/ZrO2/SiO2 stacks for piezoelectric microactuators", Thin Solid Films 510 January 213 ‑ 221, (2006).

[50] "Parylene Deposition Prcess" Paryleneengineering.com, N.p. (2010) Web. 15. Aug. 2012